Parametric design and optimization model

For offshore wind turbine monopile foundations with GFRP tower

L.E. van der Linden

Aerospace Engineering
Master of Science Thesis

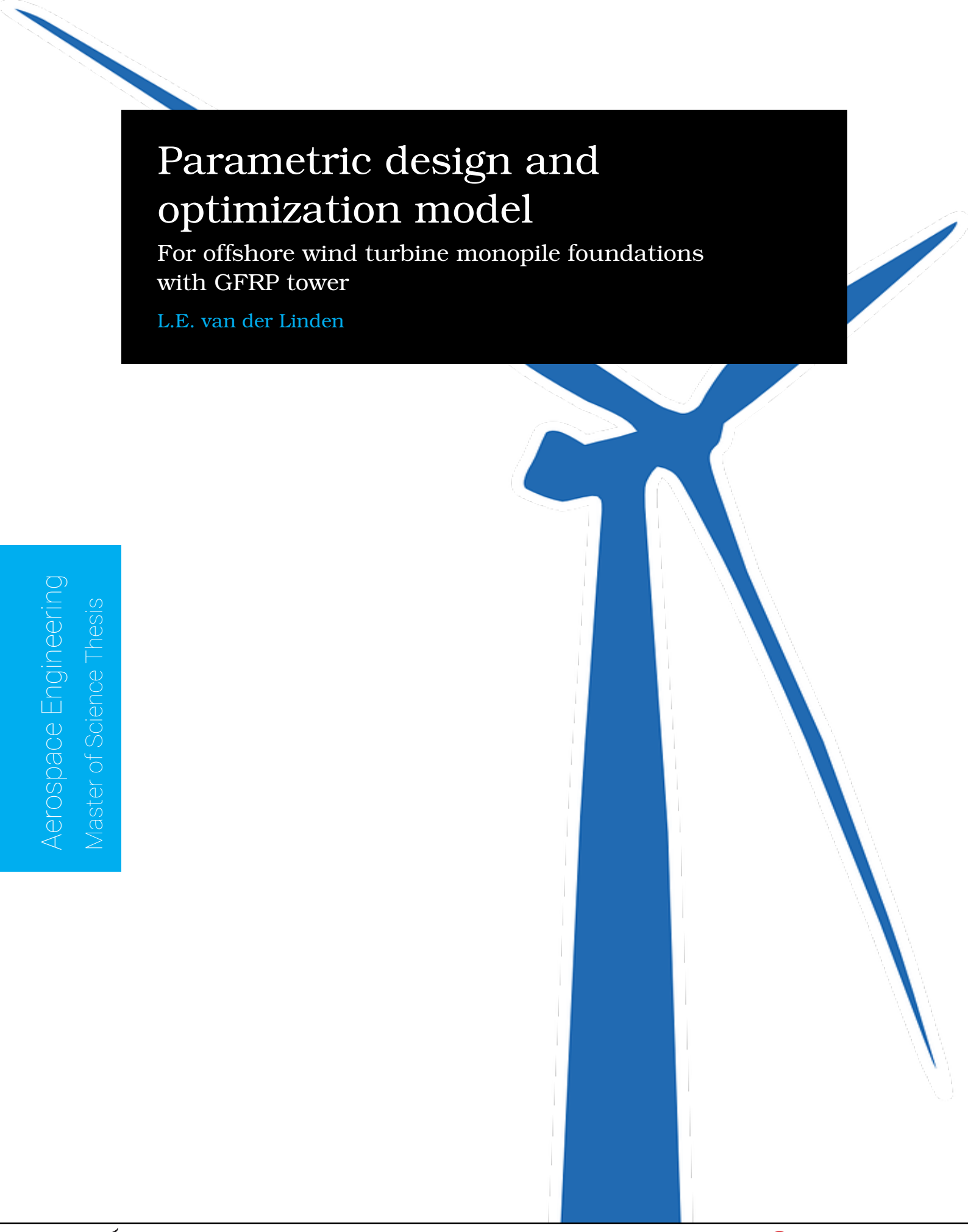

TU Delft Delft University of Technology

JULES DOCK

Parametric design and optimization model

For offshore wind turbine monopile foundations with GFRP tower

by

L.E. van der Linden

in partial fulfillment of the requirements for the degree of

Master of Science
in Aerospace Engineering

at the Delft University of Technology,
to be defended publicly on Monday October 7, 2019 at 09:00 AM.

Student number: 4217934

Thesis committee:	Prof. dr. S.J. Watson	Delft University of Technology, Chairman
	Dr. ir. W.A.A.M. Bierbooms	Delft University of Technology, Thesis Supervisor
	Dr. ir. O.K. Bergsma	Delft University of Technology, Supervisor
	Ir. Kerssemakers	Jules Dock, Supervisor

This thesis is confidential and cannot be made public until November 1, 2024.

TU Delft Delft University of Technology

JULES DOCK

Cover image: `https://pixabay.com/nl/users/Clker-Free-Vector-Images-3736`

Summary

The offshore wind energy market is highly dynamic and one of the major challenges is to become more cost competitive against other sources of energy. The support structure of an offshore wind turbine shows a high potential for further cost reduction. Jules Dock is investigating in the replacement of a steel tower on a monopile foundation by a Glass Fiber Reinforced Plastic (GFRP) tower, which has a higher specific strength and better corrosion resistance compared to steel. This would enable lower transportation and installation costs and a potentially longer lifetime. Currently Jules Dock assesses the feasibility of a GFRP tower versus a steel tower using an aero-elastic simulation tool. However, such a tool is computationally demanding and requires detailed turbine data, which are often not available in a preliminary design phase. For this reason, a research project has been set-up to develop a parametric design model which can effectively be used without detailed turbine data and aero-elastic simulations, to identify the design driving constraints for preliminary designs and mass optimization purposes.

The parametric design model analyses the natural frequency constraint and Ultimate Limit State (ULS). The natural frequency of the support structure is intended to be in the soft-soft region, which will result in the lowest mass possible as has been found in previous research. The natural frequency of the support structure is analyzed with a finite beam element model, in which the Rotor Nacelle Assembly (RNA) is modelled as a point mass. The interaction with soil is also included using a three spring model. For the ULS, the yield and buckling capacity of the support structure are analyzed. For the steel monopile and transition piece, dedicated design standards have been used. For the composite tower, however, these design standards are not existing and therefore analytical solutions from composite tube applications have been used and verified for this purpose. FEM analysis showed that the yield capacity can be determined exactly. The buckling capacity approximation in the parametric design model showed conservative results compared to a dedicated buckling analysis tool.

In the parametric design model the maximum loading for the ULS constraints has been analyzed using a quasi-static load analysis method which includes turbulence and dynamic wave loading effects. This method has been compared with the time-domain simulation tool Phatas, which is integrated in Focus6. This comparison showed that also the tower top bending moment should have been included. If this is taken into account, the integrated load analysis method appears to approach the maximum loading for a very stiff tower quite accurately compared with the time-domain simulations. For flexible towers, however, the loads are less accurately approached, since dynamic interactions between wind and wave loading have appeared to be relevant, especially for load cases with a wave excitation frequency close to the natural frequency of the support structure. In the quasi-static load analysis method these dynamic effects are only taken into account for the submerged part of the support structure, but the time-domain simulations have shown that these effects will increase the maximum loading on the support structure above water level as well.

For mass optimization and identification of the design driving constraints of this support structure, a genetic algorithm has been developed. Several optimization runs have been made, resulting in multiple feasible solutions with only small differences in support structure mass. While the buckling constraint drives the design of the monopile, transition piece and top of the tower, the lower part of the tower is design driven by the yield constraint.

It has been concluded that the loading analysis method in the developed parametric design model should include the tower top bending moment, since this leads to a mass increase of up to 20% of the support structure mass. Next to that, it has been observed that the optimization algorithm tends to converge to solutions with a natural frequency to be as low as possible, such that the dynamic amplification of the wave loading is minimized. For these solutions, the loading analysis method in the parametric design model may have underestimated the maximum loading on the flexible support structure. This needs to be further investigated.

Acknowledgements

This thesis project brought me a lot of new insights in the challenging engineering field of offshore wind energy, but could not have been finished with success without the support of a number of people.

First of all, I would like to Ties Kerssemakers, who provided me a lot of guidance during the execution of this thesis project as a daily supervisor at Jules Dock. Next to that, I would like to thank Dr. ir. Bierbooms and Dr. ir. Bergsma of the TU Delft, for providing me a lot of input on the topics related to offshore wind and composite engineering. Also I would like to thank T. van der Zee and G. de Winkel of LM Wind Power for answering all my questions related to Focus6. Finally, I would like to thank my friends and parents for their continuous support during my entire studies in Delft.

Contents

List of Symbols

A	Cross sectional area	[m^2]
A_R	Rotor swept area	[m^2]
C	Reduced buckling coefficient	[-]
C_D	Drag coefficient	[-]
C_{DS}	Relative roughness parameter	[-]
C_m	Inertia coefficient	[-]
C_T	Aerodynamic thrust coefficient	[-]
c_u	Undrained shear strength	[Nm^2]
D_p	Pile diameter	[m]
d	Mean water depth	[m]
E	Youngs Modulus	[Pa]
F_{M_s}	Fitness value	[kg]
F_T	Aerodynamic rotor thrust	[N]
F_t	Fluctuating wind loading	[N]
F_q	Mean wind loading	[N]
F_w	Wave loading	[Nm^1]
F_{wind}	Total wind loading	[N]
f	Coupling stiffness term as defined in Focus6	[m]
f_n	Natural frequency	[Hz]
H_m	Maximum wave height	[m]
h	Height above sea level	[m]
I	Area moment of inertia	[m^4]
I_{ref}	Turbulence intensity at wind speed of 15 m/s	[-]
I_v	Turbulence intensity	[-]
K_L	Lateral soil stiffness	[Nm^{-1}]
K_{LR}	Cross-coupling soil stiffness	[N]
K_R	Rotational soil stiffness	[Nm rad^{-1}]
[$\mathbf{K_s}$]	Stiffness matrix	
K_u	Lateral soil stiffness as defined in Focus6	[Nm^{-1}]
K_ϕ	Rotational soil stiffness as defined in Focus6	[Nm rad^{-1}]
k	Wave number	[m^{-1}]
k_h	Modulus of subgrade reaction	[Nm^{-3}]
k_p	Turbulence peak factor	[-]
k_r	Surface roughness	[m]
L	Support structure length	[m]
L_k	Integral length scale parameter	[m]
L_p	Embedded pile length	[m]
l	Element length	[m]
l_p	Monopile/transition piece length	[m]
M_{RNA}	Rotor nacelle assembly mass	[kg]
[$\mathbf{M_s}$]	Mass matrix	
M_y	Bending load	[Nm]
m	Mass distribution	[kgm^{-1}]
N	Axial load	[N]
n_h	Coefficient of subgrade reaction	[Nm^{-3}]
p	Penalty value	[-]
q	Distributed wind loading	[Nm^{-1}]
R_e	Reynolds number	[-]
r	Radius	[m]

r_m	Radius till midplane	[m]
S	Wave steepness	[m]
$[\mathbf{S}^{(i)}]$	Compliance matrix of individual layer	
$[\mathbf{S_h}]$	Homogenized compliance matrix in cylindrical coordinate system	
$[\mathbf{S_L^{(i)}}]$	Compliance matrix of individual layer in cylindrical coordinate system	
T_p	Wave period	[s]
t	Thickness	[m]
t_r	Thickness ratio	[-]
U_r	Ursell parameter	[-]
u	Wave velocity	[ms^{-1}]
$\dot{u}$	Wave acceleration	[ms^{-2}]
u_{max}	Maximum wave velocity at still water level	[ms^{-2}]
V	Wind speed	[ms^{-1}]
$\bar{V}$	Mean wind speed	[ms^{-1}]
V_{avg}	Long term average wind speed	[ms^{-1}]
V_r	Rated wind speed	[ms^{-1}]
V_{ref}	Reference wind speed	[ms^{-1}]
v	Turbulent wind speed	[ms^{-1}]
X^c	Compressive strength in fiber direction	[MPa]
X^t	Tensile strength in fiber direction	[MPa]
Y^c	Compressive strength in matrix direction	[MPa]
Y^t	Tensile strength in matrix direction	[MPa]
Z_l	Curvature parameter [-]	
z	Water depth coordinate	[m]
α	Wind shear coefficient	[-]
β	Slenderness parameter	[-]
γ_{FF}	Fiber failure material factor	
γ_{IFF}	Inter fiber failure material factor	
γ_M	Material factor	[-]
γ_{sand}	Sand specific weight	[Nm^{-3}]
ϵ	Wave perturbation coefficient	[-]
ζ	Damping ratio	[-]
η	Water elevation	[m]
λ	Wave length	[m]
$\bar{\lambda_s}$	Reduced slenderness	[-]
μ_w	Shallow water parameter	[-]
ν	Poisson ratio	[-]
ρ	Density	[kgm^{-3}]
σ_a	Axial stress	[Pa]
σ_{cr}	Critical buckling stress	[Pa]
σ_{Ea}	Axial characteristic buckling strength	[Pa]
σ_{Em}	Bending characteristic buckling strength	[Pa]
σ_m	Bending stress	[Pa]
σ_{max}	Maximum stress	[Pa]
σ_v	Wind speed standard deviation	[m/s]
σ_{yield}	Yield stress	[Pa]
ϕ	Velocity potential	[m^{2}s^{-1}]
Ψ	Wake amplification factor	[-]
ω	Wave angular frequency	[rads^{-1}]

List of Abbreviations

DAF	Dynamic Amplification Factor
DLC	Design Load Case
ETM	Extreme Turbulence Model
EWM	Extreme Wind Model
FLS	Fatigue Limit State
GA	Genetic Algorithm
GFRP	Glass Fiber Reinforced Plastic
KC	Keulegan-Carpenter number
NTM	Normal Turbulence Model
RNA	Rotor Nacelle Assembly
RPM	Revolutions Per Minute
SLS	Serviceability Limit State
ULS	Ultimate Limit State

1 Introduction

1.1. Composite tower for offshore wind support structures

The wind energy market is continuously expanding; whereas the installed capacity was 432 GW in 2015, it is estimated that this will grow to 2000 GW in the year 2030 [1]. One of the challenges for the offshore wind industry is to become cost competitive with other energy sources [2]. The foundation and substructure costs of an offshore wind turbine are estimated to be 19% to 25% of the capital costs [3, 4] and there is still a high potential for cost reduction [5]. Jules Dock is aiming at reducing costs by the integration of a Glass Fiber Reinforced Plastic (GFRP) tower with a monopile foundation. A composite tower has a high specific strength compared to a steel tower, by which the mass of the tower can be reduced compared to a steel tower. This potential decrease in mass might lead to a reduction in transportation and installation costs [6]. Next to that, the high corrosion resistance of composite materials is especially interesting for offshore applications [7]. Currently, in collaboration with LM Wind Power (prior known as Knowlegde Centre WMC), Jules Dock investigates the feasibility of the integration of a composite wind turbine tower on a steel transition piece and monopile using an aero-elastic simulation tool. This aero-elastic tool requires all the detailed turbine data to perform its simulations and is computationally demanding and time-consuming [5, 8] . Besides, these turbine data are often not available for tender designs and parametric studies, due to confidentiality reasons with turbine manufacturers [9, 10]. For this reason, a research project is setup to develop a parametric design model which can be used without the need of detailed turbine data for tender designs, parametric studies and optimization purposes.

The standard in the wind turbine industry is that the turbine manufacturer designs the tower and the foundation manufacturer designs the foundation for technical and commercial reasons [11, 12]. However, for an optimal design in terms of mass, it was found by a number of studies [4, 11, 13] that the mass of the support structure can be reduced more efficiently. Tower or monopile mass and cost optimization has been the subject of a number of past research [8, 14–16]. These studies focused on the optimization of the foundation or tower separately. However, it was found by a number of studies [4, 11, 13] that the mass of the support structure can be reduced more efficiently if the monopile and tower are optimized simultaneously. In these studies, mass reduction of 12% up to 20% were obtained compared to a baseline design. The optimization algorithms used in these studies were able to identify the design driving constraints of the support structure as well. For a steel tower with monopile, the natural frequency and fatigue were identified as design driving constraints. A parametric design model to show the potential benefits of a composite wind turbine tower with steel monopile foundation does not yet exist and will be the subject of this research. To identify the design driving constraints for this type of support structure, an optimization algorithm has to be implemented as well. Most beneficial would be an integrated design approach for the complete wind farm design [17]. Several studies were performed optimizing in a multidisciplinary approach, in which rotor and/or control parameters [12, 18, 19] or wind farm layout [20], is optimized simultaneously with the support structure. However, this will not be taken into account in this research project.

1.2. Research Questions

To find the design driving constraints for a monopile foundation with GFRP wind turbine tower, the research question is formulated as:

What are the design constraints for a GFRP wind turbine tower with monopile foundation for large offshore wind turbines and how do these design constraints influence the mass optimization of the integrated support structure in a preliminary design?

Related subquestions are:

- To what extend can a quasi-static load estimation model without detailed turbine data be used in a preliminary design phase?
- To what extend can analytical solutions for composite tubes be used for the structural analysis of the composite tower in this parametric model?
- What are the design constraints for the monopile, transition piece and GFRP tower separately?

1.3. Research objectives

From this research question, the following research objective can be formulated:

Identify the design constraints for a GFRP tower with monopile foundation offshore wind turbine support structure by designing a parametric model with optimization tool for a GFRP wind turbine tower with monopile foundation.

The tasks that will be conducted during the research are:

- Develop a parametric design model for a monopile with GFRP tower
- Implement the design constraints for an offshore wind turbine support structure
- Develop an optimization module for the parametric model to identify the design driving constraints
- Perform a sensitivity study on the load estimation model to identify the influence on the design driving constraints

1.4. Methodology

To answer the research question, a parametric model with optimization routines has to be developed. This will be implemented in Python. As will be outlined in chapter 2, the design constraints consists of the maximum stress constraint, global and local buckling constraint, monopile and tower deflection constraint and fatigue constraint. For this parametric design model, used for preliminary designs, the fatigue and deflection constraints will be considered outside the scope of the project. The stress and buckling constraints for the steel monopile and transition piece will be analyzed using the described methods by the DNV standards, whereas for the composite tower analytical solutions for specific loading conditions will be used. These have to be verified with a 3D finite element model. The loads will be determined using quasi-static load analysis methods, such that the model can be used without computationally expensive time-domain simulations and required turbine data. This model will be verified with the time-domain simulation tool Phatas integrated in Focus6, using the aero-elastic model of the AVATAR 10 MW research turbine.

1.5. Results and Relevance

The optimization module will be used to identify the design driving constraint for this type of support structure using a case study. The Borssele III location in the North Sea near the Dutch coast will be used, since the data for this location is publicly available [21]. Next to this case study, the optimization module will be used to identify the sensitivity on the design on the quasi-static load analysis model.

A GFRP tower with monopile support structure is a new concept and still in the development phase. This parametric model can help to identify the design driving constraints for different locations. Next to that, it

can be used to identify the advantages and disadvantages compared to conventional steel tower designs. It is expected that this model can be used by Jules Dock for future preliminary and tender designs and that it will support their business case without the need of detailed turbine data which are often difficult to obtain from industry.

1.6. Project outline

In chapter 2 background information on past research on composite applications for wind turbine structures and parametric design modelling is given. In chapter 3, the way the support structure is modelled to analyze the natural frequency is explained, and verified using Focus6. In chapter 4, the parametric load estimation model is discussed, and is verified in a number of steps. First, constant wind and hydrodynamic loading is compared separately, after which effects of turbulence and dynamic amplification are added. In chapter 5, the implementation of the structural analysis of the monopile, transition piece and tower is outlined. The structural analysis model of the composite tower is verified using WMC FEM and Finstrip. In chapter 6, the optimization routine is discussed in detail, after which the case study and sensitivity analyses are given. The report ends with the conclusions and recommendations in chapter 7.

2

Background Information

In this chapter relevant research on the topic of composite wind turbine towers is discussed. Firstly, in section 2.1 past research projects on the applicability and feasibility of GFRP material for wind turbine towers is discussed. In section 2.2 the design constraints a wind turbine tower must fulfill are outlined, in section 2.3 load estimation tools are analyzed and optimization strategies are discussed in section 2.4.

2.1. Past research on composite wind turbine towers

A number of research projects have been conducted in the past to identify the applicability of composite materials for wind turbine towers. In section 2.1.1 application studies of composite materials in wind turbine towers is discussed, and in section 2.1.2 the feasibility for offshore applications.

2.1.1. Composite material applications in wind turbine towers

A number of studies have been performed on the use of composite materials for wind turbine tower applications. Polyzois et al [6] and Hasan [22] investigated the design of a multi-cell GFRP wind turbine tower. This multi-cell tower consists of multiple segments (the cells), to reduce the costs of transportation and installation of wind turbine towers in remote areas. The cross-section of an eight-cell tower configuration is shown in figure 2.1. Design criteria analyzed were maximum failure loading, buckling capacity and natural frequencies. Prototypes of the cell segments and a 4.8 m high tower has been build and tested to validate the finite element models developed. Local buckling was identified as first failure mode in these tests. The eight-cell tower design achieved a 14% mass reduction compared to a conventional steel tower design.

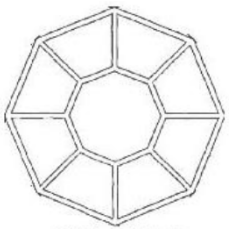

Figure 2.1: Eigth cell FRP tower design [22]

In the Megawind project [23] two composite tower concepts were developed. The motivation for this study was the expectation of lower maintenance costs, better damping characteristics, longer fatigue life and reduced costs for installation in comparison with a steel tower. The original concept consisted of lightweight composite formwork segments. These segments would be assembled on site, where they would be filled with a concrete core. The second concept consisted of jointed solid composite shell segments. These two concepts were build on a 1:3 scale of the 50 meter prototype and tested on natural frequency and structural capacity. The solid tower met all the structural requirements, while the concrete filled tower showed bad performance in shear transfer between the glass fiber skins and concrete core.

Lim et al [24] investigated the design procedure for a 100 meter long tower for a 2 MW class wind turbine system, using glass/polyester face sheets and sand/polyester core material. Different lay-up sequences were analyzed, taking into account the effects of the proposed filament winding production process. Only a storm load case was considered in which the parked blades and the tower wind loading produce a shear force and bending moment along the tower. Stresses, top deflection and buckling modes of the composite tower have been analyzed using finite element models. A final design of 100 meter was presented with a mass of 270 tonnes.

2.1.2. Offshore applications

Next to these studies on the use of composite materials for wind turbine towers, research has been done on the specific use of composite towers for offshore applications. The DeepCwind Consortium [25, 26] designed, manufactured and tested a 1:8 scaled prototype of the offshore floating 6 MW VolturnUS wind turbine. This scaled prototype is shown in figure 2.2. In this concept, the tower is made of GFRP material. The benefits of GFRP material for floating wind turbines is especially the reduction in weight, which brings the mass of the floating substructure down. In this study and test, the design load cases were obtained from the ABS Guide for Building and Classing Floating Offshore Wind Turbine Installations. Data was collected to verify the aeroelastic code FAST, which was initially used to calculate the loads on the design.

Figure 2.2: VolturnUS 1:8 scale prototype [7]

Young et al. [7] used this VolturnUS concept as case study for their proposal of an optimization strategy for the composite tower. Three different designs (steel, sandwich composite and solid composite) were analyzed and compared. The tower loading was obtained using FAST in which four design load cases were analyzed. The optimization algorithm used was a Genetic Algorithm (GA). The constraints used in the optimization phase included natural frequency, maximum stress and buckling load, while fatigue was neglected and only checked for the optimized design. Including fatigue in the optimization would have increased the computational time while fatigue was not expected to be a design driver. The optimization parameters used for the three different cases are the thicknesses of the steel and composite materials at predefined stations of the tower. For the steel tower, the bottom thickness, the thickness halfway and the top thickness were optimized. For the two composite towers, the thickness of the inner composite layer, foam core material and top layer were optimized at the bottom section and top section. In between these stations, the values of the thickness are determined using linear interpolation to increase the optimization time. Only unidirectional material was used in the optimization. While the natural frequency constraint was design driving for the steel tower design, the design driving constraints for both composite design were both the buckling and frequency constraint. Since the optimal mass of the sandwich tower design was almost equal to the solid composite tower design, the latter one is suggested because of its production simplicity. For this design, a mass reduction of 55% was achieved compared to the optimized steel tower design.

The feasibility of a soft-soft GFRP tower with monopile support structure was shown by van der Zee et al. [27] for a 10 MW offshore wind turbine. The DTU 10 MW wind turbine on a location in the North Sea was used as a case study. Load analysis was performed using time-domain simulations with the aeroelastic simulation tool Phatas implemented in Focus6. Design constraints considered in the design were maximum stress, blade clearance, tower top deflection, buckling and fatigue. To reduce computational effort, only a limited number of load cases was used in the optimization phase, and the fatigue analysis was only performed after the optimization. Monopile dimensions of the baseline support structure were not changed for the composite tower design. The diameter of the composite tower was fixed as well, while its thickness and laminate lay-up has been used as optimization variables. It was concluded that a optimal solution would be found moving the natural frequency of the support structure below the 1P area, instead of a soft-stiff design with its first natural frequency between the 1P and 3P area. The optimized composite tower design showed a mass reduction of 34% compared to the baseline steel tower design.

2.2. Parametric model design constraints

In this section the design constraints which have to be fulfilled by a wind turbine support structure will be discussed.

2.2.1. Natural frequency constraint

The natural frequency of the support structure should not coincide with the operational frequency of the rotor system (1P frequency range) and blade passing frequencies (3P frequency range) to avoid resonances. Another frequency constraint is the wave spectrum, which causes dynamic amplification in case of natural frequency coincidence as well [18]. In figure 2.3 a typical turbine and wave spectra is shown. Three frequency regions are possible for the natural frequency of the support structure, whereas a soft-stiff design is most often used in industry [28]. However, as discussed in section 2.1.2, the optimal composite tower design in the study of [27] with minimal mass was obtained with a first natural frequency in the soft-soft region below the 1P area, and will therefore be used as constraint in this parametric design model. The determination of the natural frequency of the support structure is described in chapter 3.

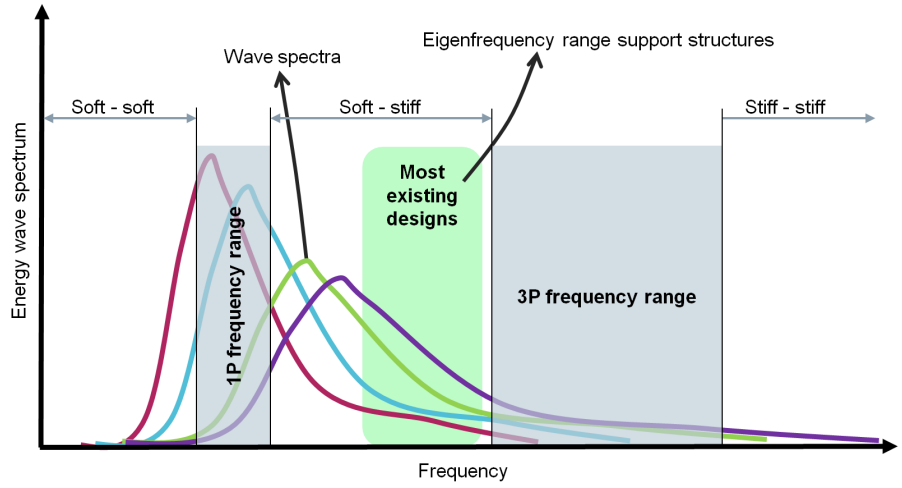

Figure 2.3: Energy spectrum [13]

2.2.2. Ultimate Limit State and Serviceability Limit State

From all the load cases a wind turbine support structure encounters during its lifetime, the maximum load has to be determined on different sections along the support structure. The dominant loading on the support structure are the bending moment, lateral shear force and axial compressive load [10]. For this maximum loading, the Ultimate Limit State (ULS) and Serviceability Limit State (SLS) should be assessed. For the ULS constraint, the ultimate load, global buckling and local buckling capacity should be analyzed, which is explained in detail in chapter 5.

The Serviceability Limit State (SLS) requirement states the limit of rotation of the monopile at the sea bed, which is ± 0.5° according to DNV-OS-J101 [29]. The requirement for maximum rotation at the tower top can be set at ± 5° [29]. For large diameter monopiles, the critical pile length criterion to assess the rotation requirement is suggested by [30]. This criterion says that the pile should be long enough such that a further increase in monopile length will have no effect on the deflection and rotation at sea bed level. The rotation at sea bed is primarily determined by the embedded length of the pile. However, the parametric model will focus on the support structure above the sea bed and therefore this criterion will not be evaluated.

For the ULS, the maximum loading along the support structure have to be determined. In literature, several load cases were used for the determination of maximum loading. Design Load Case (DLC) 6.1 of the IEC standard was used to determine maximum loading by [4, 19, 31]. This load case corresponds to a parked or idling turbine, encountering a 50-year return extreme wind speed based on the Extreme Wind Model (EWM) with a 50-year return wave height. In the worst case scenario, wind and waves are aligned. In the study of [11] DLC 6.2 was found as most severe. This load case is the same as DLC 6.1, except that a grid connection failure is present as well, such that the yaw angle can not be corrected to the wind direction. According to [10] a production load case (DLC 1.6) at rated wind speed should be taken into account since the highest aerodynamic thrust by the rotor is expected at this wind speed. Young [7] analyzed DLC 1.6 between cut-in and cut-out wind speed, DLC 6.1 and DLC 6.3 as ultimate load cases, of which DLC 1.6 at rated wind speed was found to be most severe. From the discrepancies between multiple studies it is concluded that not a single load case can be assigned to be most severe on forehand. DLC 1.6 and DLC 6.1 both will be considered for the determination of the maximum loading on the structure. According to the DNV-OS-J101 standard [32], the varying loads have to be multiplied by a load factor of 1.35, and the permanent loads (the gravitational load) by a factor of 1.1.

2.2.3. Fatigue Limit State

Wind turbine structures are designed for a lifetime of 20 to 25 years. A wind turbine is loaded dynamically and since the turbine is dynamically loaded, it is prone for fatigue damage [5], which is analysed in the Fatigue Limit State (FLS) requirement. The stress ranges due to the dynamic loading will cause cracks in the material which will lead to failure [33]. The fatigue damage in the steel monopile and transition piece can be determined using Miner's rule, given in equation 2.1 [34]. Here is n_i the number of cycles of a certain stress range bin and N_i the cycles to failure. The number of cycles for a certain stress range are given in so called S-N curves [32], of which an example is given in figure 2.4. For composite materials, these S-N curves are not as straightforward as for steel materials, whereas the S-N curve for composite materials depends on the mean stress loading as well [35].

$$D = \Sigma \frac{n_i}{N_i} \tag{2.1}$$

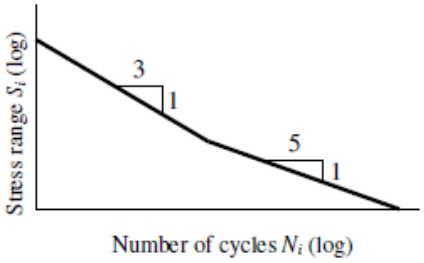

Figure 2.4: Typical S-N curve, with slope 5 and 3 on log scale [33]

The fatigue damage on the support structure is determined by all loading conditions over the lifetime on the support structure. However, the number of load cases to be analyzed can be reduced. a representative load case is the DLC 2.1 from the IEC standard [4], which is the entire operational range of the wind turbine. DLC 2.1 is responsible for 80% of the total fatigue loads [36]. A Normal Turbulence Model (NTM), Normal Sea State (NSS) and zero current are applicable. The safety factor in these load cases corresponds to 1.0. In a number of

design studies ([1, 4]), DLC 2.1 is represented by a single load case. The Damage Equivalent Load approach is used to derive one single fatigue load. This A more detailed fatigue analysis has been performed by [19] and [33], where multiple load cases for DLC 2.1 were analyzed. A limited number of sea states is used to represent the complete lifetime of the turbine. Each lumped sea state is described by the significant wave height, zero cross period, wind speed and probability of occurrence.

2.3. Load estimation

A wind turbine is a dynamic system, and since the natural frequency of the support structure has its natural frequency close to the operational frequency the dynamics will have a influence on the loads [37]. The stochastic nature of the environmental loads makes it hard to predict the ultimate load and fatigue load on the support structure over the complete lifetime of the turbine. These dynamic and stochastic loads can be calculated using time-domain, frequency-domain simulations or using static load analysis. Time-domain simulations, where thousands of load cases are analyzed, is the most accurate way, and therefore used for certification analysis [5]. This technique is used in a number of parametric and optimization studies [7, 11, 27]. However, detailed turbine data is required for time-domain aeroelastic simulations [2]. Next to that, geometry optimization requires a lot of iterations, which would be time consuming when time-domain simulation load analysis is used. Therefore, static load analysis is recommended for optimization purposes [5].

Static load analysis techniques without making time-domain simulations to determine the ultimate load is used in parametric and optimization studies for wind turbine support structures as well [4, 10, 31]. However, the loading on the turbine has a dynamic nature. Turbulence, wave loading, mass and aerodynamic imbalances of the rotor and tower shadow effects can be considered as dynamic loads [10]. For the latter two, detailed turbine data will be required and will therefore be disregarded in the parametric load estimation model. The differences between the determination of maximum loading using aeroelastic simulations and quasi-static load analyses techniques are dealt with in chapter 4.

For the fatigue analysis, a bin of stress ranges and number of cycles of this stress range have to be determined to apply Miner's rule given in equation 2.1. In time-domain simulations, fatigue loading is most commonly calculated by rain flow counting [33, 35]. To reduce computational costs, a frequency-domain analysis was proposed by [33]. This method determines the bending moment spectrum in frequency-domain, but requires initial time-domain simulations for the determination of transfer functions. A frequency-domain analysis method for the determination of the bending moment spectrum which does not require time-domain simulations was proposed by [37]. This bending moment could then be used as input for cycle counting methods such as Rayleigh, Rice and Dirlik, of which the latter one was found to be most accurate compared to rain flow counting used in time-domain [33]. However, as mentioned in section 2.2.3, for the application of SN-curves for composite materials, the mean stress should be known as well. No feasible method was found for the determination of mean stress using quasi-static load analyses techniques and will be considered outside the scope of the project. Therefore the FLS requirement is left out in the parametric design model.

2.4. Integrated optimization

The standard in industry is that the turbine manufacturer designs the tower and the foundation manufacturer designs the foundation [11], for technical and commercial reasons [12]. Tower or monopile mass and cost optimization has been the subject of a number of past research [8, 14–16]. The structure was optimized by varying diameter and thickness. These studies focused on the optimization of the foundation or tower separately. However, it was found by a number of studies [4, 11, 13] that the mass of the support structure can be reduced more efficiently if the monopile and tower are optimized simultaneously. In these studies, mass reduction of 12% up to 20% were obtained compared to a baseline design. These optimization tools were able to identify the design driving constraints of the support structure as well. For a steel tower with monopile, the natural frequency and fatigue were identified as design driving constraints in these studies, by which the minimal support structure mass was set. Most beneficial would be an integrated design approach for the complete wind farm design [17]. Several studies were performed optimizing in a multidisciplinary approach, in which rotor and/or control parameters [12, 18, 19] or wind farm layout [20], is optimized simultaneously with the support structure. However, the integration of all these aspects will not be feasible within this research project.

2.4.1. Optimization algorithms

The goal of the optimization is to minimize the mass of the complete support structure. As mentioned in section 2.4, the minimal mass will be found if monopile, transition piece and tower are optimized simultaneously. According to [4], two types of optimization algorithms for the optimization of a support structure exist; calculus-based and meta-heuristic algorithms. In calculus-based algorithms, the sensitivity of each design variable is analyzed. By changing the design variable, the gradient of the objective function (the mass of the support structure) is determined. The optimization of a support structure is a non-linear problem [11], and applying a calculus-based algorithm to a non-linear problem can result in a local optima, and therefore meta-heuristic algorithms are preferred [4].The meta-heuristic algorithms are based on iterative procedures, in which the design variables are assigned with values randomly within the design space. This way the whole design space is evaluated and the chance of finding a (near-)global optimum is more likely. One of these meta-heuristic algorithms is the Genetic Algorithm (GA), which was used for the composite tower optimization study by [7]. GA is widely used for optimization of composite blades as well, due to its ability to handle a large number of variables [38]. Therefore a GA algorithm will be used for the mass optimization of the support structure. The implementation of the GA is described in chapter 6.

2.4.2. Optimization variables

The mass of the support structure can be minimized by altering the geometry of the support structure. For the steel part, the diameter and wall thickness can be used as optimization variables. Next to these geometric variables, the anisotropic properties of the GFRP material provide extra freedom in optimization. Stacking sequence, thickness of each ply and the fiber orientation can be used for optimization as well [39]. These variables can be changed on different sections along the structure. To reduce the computational time, the number of sections needs to be limited, by calculating the diameter and thickness in between sections using linear interpolation. For example, Gentils et al [4] specified the diameter of the monopile and tower only at the bottom and the top. The thickness of the monopile is only specified at the bottom and the top, whereas the thickness of the tower is specified at three sections.

3

Support Structure Natural Frequency

In this chapter, the method of support structure modelling for the determination of the natural frequency is described. Firstly in section 3.1, the finite element model is explained. In section 3.2, the inclusion of soil stiffness to the finite element model is explained. Finally, the verification of the finite element model is discussed in section 3.3.

3.1. Support structure model

Several methods do exist in literature for the determination of the natural frequency. A simple method to estimate the natural frequency of the support structure is modelling the support structure as a simple cantilever beam [10]. In this model, the mass, stiffness and thickness distribution are assumed to be constant. To capture the difference in stiffness between monopile and tower, a more elaborated analytical expression was proposed by [40].

However, differences in diameter and thickness along the height are not included in these models. This effect can be included in a finite element model, in which the support structure is divided in small elements. One dimensional beam elements or three dimensional brick or shell elements can be used. The latter one is capable of capturing stress concentrations [4], but requires all the structural details and the construction of the FEM model is time consuming. These structural details are not yet known in a preliminary design phase and therefore a one dimensional beam element model is appropriate in the parametric design tool for the determination of the natural frequency.

Of these beam element models, Euler-Bernoulli and Timoshenko beam models are used most, of which the latter one includes shear deformation [11] and will therefore be used in this model. The Timoshenko beam elements will have two nodes, each having three degrees of freedom; two translational and one rotational. The natural frequency of the system can be obtained by solving the eigenvalue problem given in equation 3.1.

$$\det|\boldsymbol{K_s} - \lambda \boldsymbol{M_s}| = 0 \tag{3.1}$$

In this equation, $\boldsymbol{K_s}$ and $\boldsymbol{M_s}$ are the global stiffness and mass matrix, respectively. These matrices are assembled from the element stiffness and mass matrices, of which the derivation is given in Appendix B. From the finite element model the natural frequency is determined by solving the eigenvalue problem in equation 3.2.

$$f_i = \frac{\sqrt{\lambda_i}}{2\pi} \tag{3.2}$$

The required input for the mass and stiffness matrices for each beam element with length l are the mass (ρAl), tensile stiffness (EA), bending stiffness (EI) and shear modulus (G) at various heights along the structure. These properties are retrieved from the homogenized elastic constants E_z and $G_{\theta z}$, which will be discussed in section 5.2.1. The determination of the bending stiffness is done according the method of Chan [41], as described in Appendix A.

3.2. Soil interaction

The interaction of the soil with the support structure has an influence on the natural frequency and cannot be neglected [4]. Different methods can be used to include this effect, of which the p-y method is used in the DNV standard [32]. However, this method originates from the oil and gas industry and is only valid for small diameter piles and overestimates the soil reaction for large diameter piles at greater depths [29]. The soil modelling approach used here is a three springs approach [42]. The soil is effectively modelled by three springs at the mudline; a lateral, rotational and cross-coupling spring, as shown in figure 3.1. The vertical stiffness of the soil is neglected in a three spring approach, since the structure is very stiff itself in this direction [42].

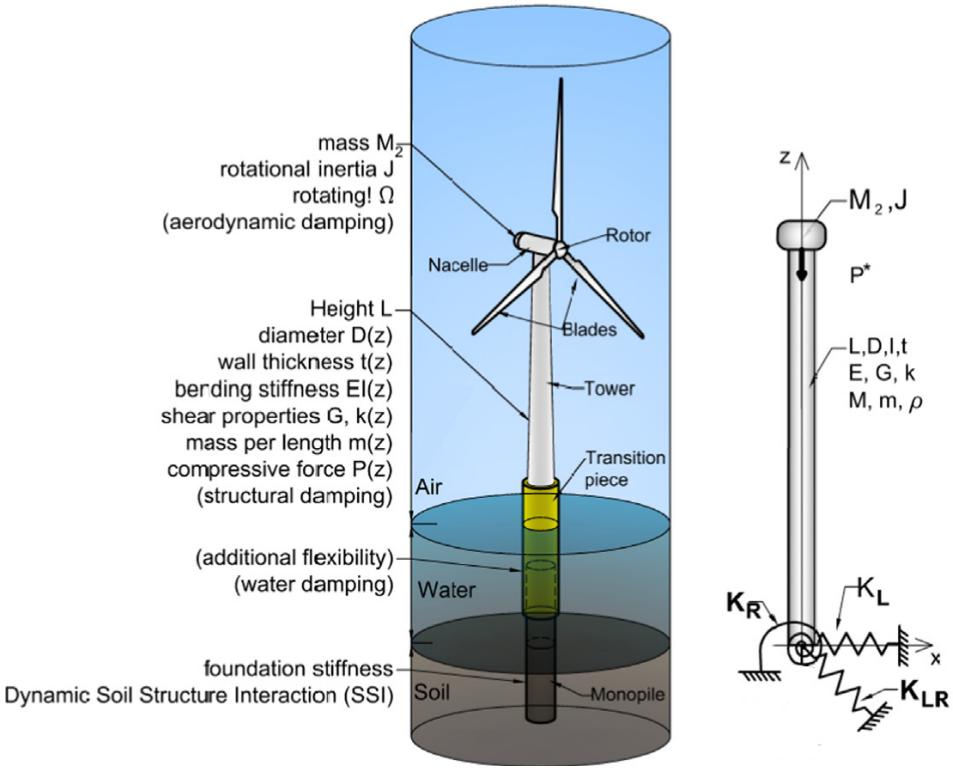

Figure 3.1: Mechanical model of wind turbine with springs attached at mudline [42]

The soil stiffness is modelled by three springs at the first node of the finite element model. These are a lateral spring with stiffness K_L, a rotational spring with stiffness K_R and a cross coupling spring with stiffness K_{LR}. These terms are added to the first node of the global stiffness matrix. This soil stiffness matrix is shown in equation 3.3 [43].

$$\bar{\boldsymbol{K}}_{\boldsymbol{f}} = \begin{bmatrix} 0 & 0 & 0 \\ 0 & K_L & K_{LR} \\ 0 & K_{LR} & K_R \end{bmatrix} \tag{3.3}$$

Several methods for the determination of the foundation stiffness properties exists in literature, of which the method of Poulos & Davis are most accurate when using a three springs approach [10]. These terms are determined differently for different types of soils. Three types of soils are mainly considered for offshore wind turbine structures; homogeneous (clay), inhomogeneous (sand) and bedrock. Homogeneous soils have constant properties over depth, whereas the properties of inhomogeneous soils change over depth [40]. In reality, multiple types of soils will be present at one location, and for a detailed soil stiffness description over depth p-y method seems more feasible, but will be left out for simplicity.

Next to the type of soil, it should be determined if the monopile can be considered rigid (the pile moves as a rigid body) or slender (the pile itself will deform). For homogeneous soils, the pile can be considered slender if $\beta L_p > 2.5$ and rigid if $\beta L_p < 1.5$, in which the slenderness parameter β is given by equation 3.4 [40]. For

inhomogeneous soils, the determination of a rigid or slender pile should be considered is given in equation 3.5 [10]. The equations for the stiffness terms for homogeneous and inhomogeneous soils are listed in Table 3.1.

$$\beta = \sqrt[4]{\frac{k_h D_p}{4 E_p I_p}} \tag{3.4}$$

$$\text{Slender if:} \quad L_p > 4.0\left(\frac{E_p I_p}{n_h}\right)^{\frac{1}{5}} \qquad \text{Rigid if:} \quad L_p < 2.0\left(\frac{E_p I_p}{n_h}\right)^{\frac{1}{5}} \tag{3.5}$$

Table 3.1: Soil stiffness equations [10]

	Slender; homogeneous	Slender; inhomogeneous	Rigid; homogeneous	Rigid; inhomogeneous
K_L	$\frac{k_h D_p}{\beta}$	$1.074 n_h^{\frac{3}{5}} (E_p I_p)^{\frac{2}{5}}$	$k_h D_p L_p$	$\frac{1}{2} L_p^2 n_h$
K_{LR}	$-\frac{k_h D_p}{2\beta^2}$ (1)	$-0.99 n_h^{\frac{2}{5}} (E_p I_p)^{\frac{3}{5}}$	$-\frac{k_h D_p L_p^2}{2}$	$-\frac{1}{3} L_p^3 n_h$
K_R	$\frac{k_h D_p}{2\beta^3}$	$1.48 n_h^{\frac{1}{5}} (E_p I_p)^{\frac{4}{5}}$	$\frac{k_h D_p L_p^3}{3}$	$\frac{1}{4} L_p^4 n_h$

Next to the monopile parameters E_p, I_p and D_p at mudline level, for homogeneous soils the modulus of subgrade reaction k_h is required. Several approximations for the modulus of subgrade reaction are provided in literature [40]. In the parametric model use will be made of the method proposed by Skempton, as given in equation 3.6, since it only requires the undrained shear strength c_u as required soil input parameter. A factor A_c between 80 and 320 has to be added. For inhomogeneous soils, the coefficient of subgrade reaction is required and given in equation 3.7. Soil parameter required is the specific weight γ_{sand}. The factor A_s has a value of 100-300 for loose sand, 300-1000 for medium sand and 1000-2000 for dense sand. To identify the influence of the estimation of these soil factors, a sensitivity study needs to be performed, but will be considered outside the scope of this project.

$$k_h = A_c \cdot \frac{c_u}{D_p} \tag{3.6}$$

$$n_h = \frac{A_s \cdot \gamma_{sand}}{1.35} \tag{3.7}$$

3.3. Beam model verification

The beam element model verification is divided in three steps such that the effect of each extra strep can be analyzed. The first step is a cantilever beam, secondly a cantilever beam with top mass and finally a beam with three springs at the bottom and a top mass. A simple, constant steel tube is used for verification. The properties of this tube are given in Table 3.2.

Table 3.2: Simple steel tube

Inner diameter	4.8 m
Thickness	0.1 m
Length	100 m
E	210 GPa

3.3.1. Cantilever beam

The cantilever beam problem is constant in diameter and thickness, and it is fixed at one end. The analytical solution for this problem is given in Equation 3.8. For the given steel tube, the first natural frequency equals 0.5015 Hz.

$$f_n = \frac{1.875^2}{2\pi} \sqrt{\frac{EI}{mL^4}} \tag{3.8}$$

This analytical solution is compared to the finite element model for various number of elements. In the analytical solution, the effect of gravitational load due to the weight of the structure itself is not taken into account, and therefore this effect will not be considered. The results are given in Table 3.3. From this, it can be concluded that the finite element model is accurate and a small number of elements is sufficient.

Table 3.3: Cantilever beam solution

Number of elements	f_n^{FE} **[Hz]**	**Error [%]**
1	0.5035	0.40
10	0.5012	-0.06
50	0.5012	-0.06
100	0.5012	-0.06

3.3.2. Cantilever beam with rotor nacelle assembly

In the finite element model, the Rotor Nacelle Assembly (RNA) is modelled as a point mass on the top node of the finite element model. In this verification, the mass of the RNA M_{RNA} of the AVATAR 10 MW turbine (702 tonnes) is used. To verify the finite element model, a comparison is made with an approximate equation (equation 3.9) for a wind turbine tower with top mass as proposed by van der Tempel [33] and with the Avatar 10 MW model in Focus6. In the Focus6 software, rotary inertia and mass misalignment of the RNA are included as shown in figure 3.2. Next to this, the effect of the axial compression load due to the self weight of the structure is included, which will have an effect on the natural frequency as well. In the approximate equation of van der Tempel, these effects are not included.

$$f_n \approx \sqrt{\frac{3.04EI}{(M_{RNA}+0.227mL)4\pi^2L^3}} \tag{3.9}$$

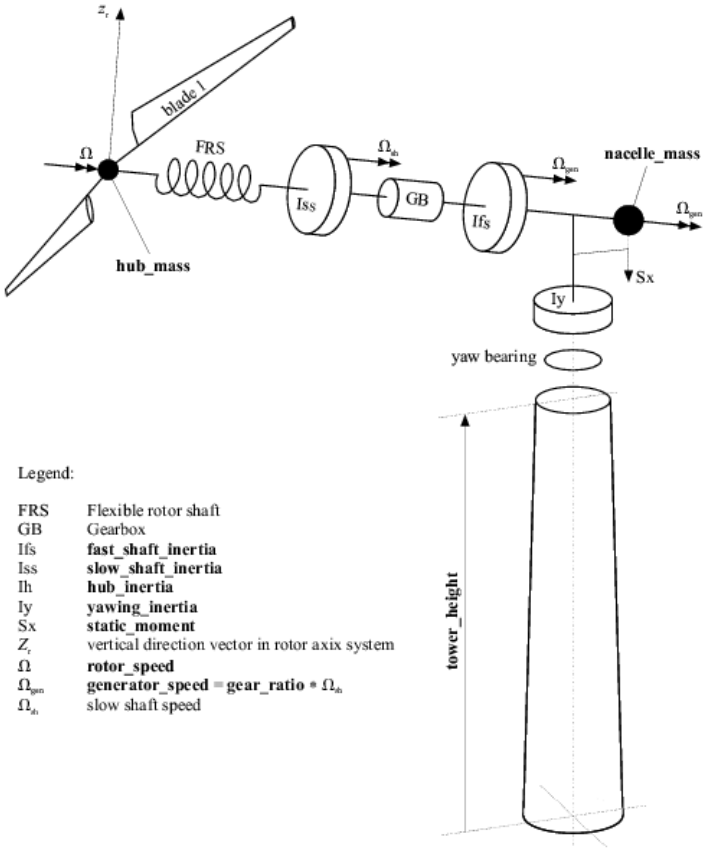

Figure 3.2: Mass properties of the turbine as defined in Focus6 [44]

The effect of the weight of the structure is included in the parametric model, while the effect of rotary inertia and rotor misalignment are not. The same tower configuration as described in the previous section will be used. The results are shown in table 3.4, with the Focus6 result including all effects as baseline result.

Table 3.4: Natural frequency determinations

Model	Frequency	Difference [%]
Focus6	0.2548	-
Focus6 w/o misalignment and inertia	0.2629	3
van der Tempel	0.2767	9
Parametric model w/o axial load	0.2723	7
Parametric model with axial load	0.2664	5

The Focus6 output including all effects results in the lowest natural frequency. In the parametric model, the natural frequency is 5% higher as the Focus6 output. Excluding the effects of misalignment and rotary inertia in Focus6, results in a 3% higher frequency. Without the effect of the self weight of the structure, the frequency is 9% higher using van der Tempel, and 7% higher using the parametric model.

3.3.3. Support structure with soil interaction

The finite element model frequency output including soil flexibility will be again compared to Focus6. In Focus6 the root flexibility is modelled using a lateral spring, rotational spring, torsional spring and a coupling term between bending and lateral displacement. Neglecting the torsional spring, which is not taken into account in a three spring approach as well, the stiffness terms can be defined in matrix form as given in equation 3.10 [44].

$$\begin{bmatrix} u \\ \phi \end{bmatrix} = \begin{bmatrix} \frac{1}{K_u} & \frac{f}{K_\phi} \\ \frac{f}{K_\phi} & \frac{1}{K_u} \end{bmatrix} \begin{bmatrix} F_{fore-aft} \\ M_{bend} \end{bmatrix} \tag{3.10}$$

As described previously, the soil modelling is included in the finite element model by a three spring approach. This can be written in matrix form, as given in equation 3.11 [10].

$$\begin{bmatrix} F_{fore-aft} \\ M_{bend} \end{bmatrix} = \begin{bmatrix} K_L & K_{LR} \\ K_{LR} & K_R \end{bmatrix} \begin{bmatrix} u \\ \phi \end{bmatrix} \tag{3.11}$$

The required inputs for the soil modelling in Focus6 can be obtained by inverting the stiffness matrix of the three spring approach. The result of this inversion gives the relation between K_u, K_ϕ, f and K_L, K_R, K_{LR} and is given in equation 3.12.

$$\begin{aligned} K_u &= \frac{K_L \cdot K_R - K_{LR}^2}{K_R} \\ K_\phi &= \frac{K_L \cdot K_R - K_{LR}^2}{K_L} \\ f &= -\frac{K_{LR}}{K_L} \end{aligned} \tag{3.12}$$

For the verification, each of the three spring terms is added separately such that the sensitivity on the natural frequency and error between the finite element model and Focus6 can be analyzed. As soil, clay with an undrained shear strength of 800 kPa has been used, with an average value for A_c of 200. An embedded pile length of 35 meter is used such that the pile can be assumed to be slender. The stiffness values are calculated with the method described before and are given in Table 3.5.

Table 3.5: Soil Stiffness inputs

FEM model		**Focus6**	
K_L [N/m]	19.97 E+8	K_u [N/m]	9.98 E+8
K_R [Nm/rad]	15.55 E+10	K_ϕ [Nm/rad]	7.78 E+10
K_{LR} [N]	-12.46 E+9	f [m]	6.24

To analyze the influence of the individual lateral and rotational springs on the natural frequency in Focus6, the other stiffness terms are set at a very large number (1E30), and the coupling is set to 0. Note here that the foundation stiffness terms for the FEM model and Focus6 become equal. The last case includes all springs, including the coupling stiffness term. The difference between the finite element model and Focus6 is given in Table 3.6. The rotational stiffness term has the most influence on the natural frequency. The difference remains more or less the same including the soil stiffness terms. The finite element model overestimates the natural frequency for this specific case around 4-5%.

Table 3.6: Foundation stiffness influence

	Fixed foundation	**Lateral stiffness**	**Rotational stiffness**	**All stiffness**
Finite element model	0.2664 Hz	0.2661 Hz	0.2418 Hz	0.2179 Hz
Focus6	0.2548 Hz	0.2546 Hz	0.2321 Hz	0.2099 Hz
Difference [%]	5	5	4	4

As described in section 3.2, the soil stiffness is determined based with empirical equations based on the rigid or slender assumption. The influence of this assumption, the assumed value for undrained shear strength for clay, and the specific weight for sand is shown in figures 3.3 and 3.4, respectively. As can been seen in these figures, a gap is present in the data points. The left part of the graph is the result for the rigid assumption, and the right for the slender assumption. For pile lengths in between the rigid and slender assumption, interpolation can be used. However, in the parametric model the design of the embedded pile will not be considered. It will be assumed that the embedded pile can be considered slender in all cases, since the natural frequency of the support structure will not change for slender piles as can been seen in figures 3.3 and 3.4.

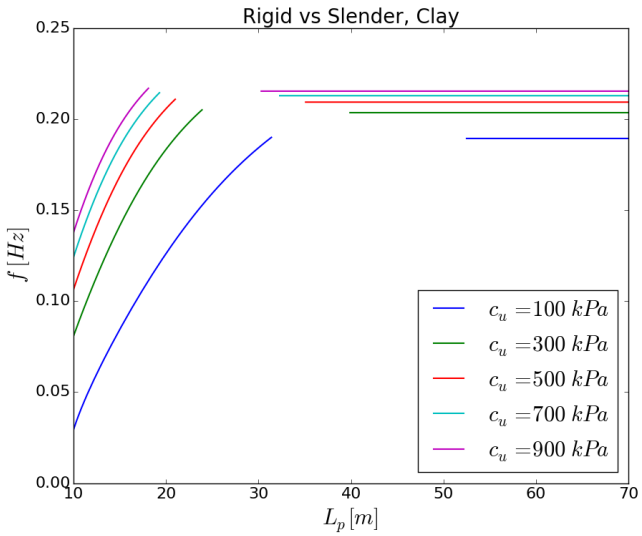

Figure 3.3: Natural frequency for monopile in clay

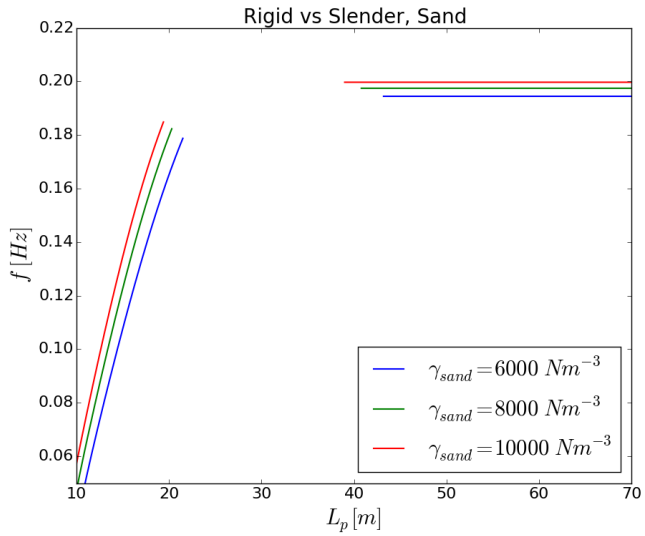

Figure 3.4: Natural frequency for monopile in sand

3.3.4. Conclusion

The finite element model in the parametric design tool overestimates the natural frequency in the order of 4-5% compared to the output of Focus6. The main difference is due to the effect or rotor misalignment and rotary inertia, which decreases the frequency by 3%. However, the parametric design tool should be usable without detailed turbine data and therefore these two effects will not be included in the parametric design tool. The support structure is supposed to be designed such that the natural frequency is below the 1P area and the wave peak frequency. Therefore, an overestimation of the natural frequency in a preliminary design phase will be on the conservative side. This holds true for the assumption of a slender pile for the soil stiffness determination as well.

4

Load Estimation Model

Several sources of loads act on the support structure. In section 4.1 and 4.2 the wind loading and wave loading will be discussed, respectively. In section 4.3 the inclusion of dynamic effects on the loading is explained. In section 4.4 the load estimation will be verified using the aero-elastic simulation tool integrated in Focus6, using the aero-elastic model of the Avatar 10 MW research turbine.

4.1. Wind loading

The rotor of the wind turbine produces thrust in operational condition, which can be determined with equation 4.1 [10]. In this equation, ρ_a is the air density, A_R the rotor swept area, V the wind speed and C_T the aerodynamic thrust coefficient. For an accurate determination of C_T, blade element momentum theory should be used, with the need of detailed blade properties data. As the purpose of this model is to eliminate the use of this detailed information, the method of Frohboese and Schmuck [45] is used. This method can be used between cut-in wind speed and rated wind speed [10, 37], given in equation 4.2. After rated wind speed, the power remains constant and therefore it may be assumed that the thrust coefficient is inversely proportional to the cube of the wind speed [10], as given in equation 4.3.

$$F_T = \frac{1}{2}\rho_a A_R C_T V^2 \tag{4.1}$$

$$C_T(V \leq V_r) = \frac{3.5(2V_r - 3.5)}{V_r^2} \approx \frac{7}{V_r} \tag{4.2}$$

$$C_T(V > V_r) = \frac{3.5V_r(2V_r - 3.5)}{V^3} \tag{4.3}$$

Next to the aerodynamic thrust, the wind acts as a distributed load along the tower and is calculated with equation 4.4. The wind speed profile $V(h)$ is calculated with the power law described in equation 4.5, with a shear coefficient α, which is set at 0.11 for offshore locations [32]. For heights lower than ten meter, a logarithmic profile as described in equation 4.6 is used [44]. In these equations, $C_{D,t}$ is the towers drag coefficient, A_t equals the outer diameter of the tower and V_{ref} is the wind speed at reference height h^*.

$$q(h) = 0.5\rho_a V(h)^2 C_{D,t} A_t \tag{4.4}$$

$$V(h) = V_{ref}\left(\frac{h}{h^*}\right)^{\alpha} \tag{4.5}$$

$$V(h) = V_{ref}\frac{\ln\left(\frac{h}{\alpha}\right)}{\ln\left(\frac{h^*}{\alpha}\right)} \tag{4.6}$$

The nacelle front area will produce drag as well. This drag force is calculated in similar fashion as equation 4.4, where the area and drag coefficient of the tower have to be replaced for the area and drag coefficient of

the nacelle. According to [44], the drag coefficient of the nacelle front area equals 1.2.

For load cases with a wind speed higher then the cut-out wind speeds, the blades are pitched out of the wind but still produce drag. This drag can be calculated with equation 4.7 [22]. The drag coefficient and blade area do vary along the blade span, since chord length and blade profile change over the blade. In this parametric loading tool, no detailed turbine data is available and therefor a drag coefficient $C_{d_{blade}}$ and blade area A_{blade} for the complete rotor blade will be estimated. For the comparison with the Avatar 10MW turbine in Focus6, the blade area is estimated by the average chord length times the blade span. The drag coefficient is estimated to be 0.038.

$$F_{T_{parked}} = 0.5\rho_a V^2 3 C_{d_{blade}} A_{blade} \tag{4.7}$$

4.2. Hydrodynamic loading

In this section, the applied wave kinematics model in the parametric model and the determination of the wave loading using the Morison equation is explained.

4.2.1. Wave kinematics

Several wave theories for the determination of the wave velocity $u(x,z,t)$ and acceleration $a(x,z,t)$ do exist. The validity of a wave theory depends on the environmental conditions and is expressed in three parameters: Wave steepness parameter S, shallow water parameter μ_w and Ursell parameter U_r, defined in equation 4.8, 4.9 and 4.10, respectively [46]. In these equations, g is the gravitational acceleration, T_p the wave period, d the mean water depth and H_m the maximum wave height. The validity of a number of common used wave theories is given in Table 4.1.

$$S = 2\pi \frac{H_m}{g T_p^2} \tag{4.8}$$

$$\mu_w = 2\pi \frac{d}{g T_p^2} \tag{4.9}$$

$$U_r = \frac{1}{4\pi^2} \frac{S}{\mu_w^3} \tag{4.10}$$

Table 4.1: Applicability of wave theories [32]

Wave Theory	**Applicability**
Linear Airy wave	$S < 0.006$; $S/\mu_w < 0.03$
2nd order Stokes wave	$U_r < 0.65$; $S < 0.04$
5th order Stokes wave	$U_r < 0.65$; $S < 0.14$
Cnoidal theory	$U_r > 0.65$; $\mu_w < 0.125$

For the determination of the ULS, the maximum 50 year wave height is one of the sea states that should be analyzed. Table 4.2 shows the data of the Borssele III site for this sea state, resulting in: $S = 0.073$, $\mu_w = 0.156$, $U_r = 0.458$, for which the 5th Order Stokes theory is valid. It should be noted that the applicability of the 5th Order Stokes wave theory is not valid for shallow water conditions where breaking waves may occur [32]. These wave conditions will not be considered in this design model.

Table 4.2: 50yr return wave at Borssele III site [21]

Water depth[m]	35.1
Maximum wave height [m]	16.42
Wave period [s]	11.99

A method for the use of the 5th order Stokes Wave theory was proposed by Fenton [47]. The wave kinematics are described by a velocity potential ϕ, given in equation 4.11 [47, 48]. In this equation, k is the wave number,

z the depth coordinate measured from mean sea level, ϵ a wave perturbation coefficient given by $\frac{kH_m}{2}$, and θ is a description of the position of the wave $(kx-\omega t)$, where ω is the angular frequency of the wave. The coefficients A_{ij} and C_0 are coefficients defined by Fenton, and are elaborated in Appendix C. From the velocity potential, the horizontal wave velocity $u(x,z,t)$ can be obtained as given in equation 4.12.

$$\begin{aligned}\phi(x,z,t) = C_0\sqrt{\frac{g}{k^3}}\big[&(\epsilon^1 A_{11}+\epsilon^3 A_{31}+\epsilon^5 A_{51})\cosh(kz)\sin(\theta)\\ &+(\epsilon^2 A_{22}+\epsilon^4 A_{42})\cosh(2kz)\sin(2\theta)\\ &+(\epsilon^3 A_{33}+\epsilon^5 A_{53})\cosh(3kz)\sin(3\theta)\\ &+(\epsilon^4 A_{44})\cosh(4kz)\sin(4\theta)\\ &+5(\epsilon^5 A_{55})\cosh(5kz)\sin(5\theta)\big]\end{aligned} \tag{4.11}$$

$$\begin{aligned}u(x,z,t) = \frac{\partial\phi}{\partial x} = C_0\sqrt{\frac{g}{k}}\big[&(\epsilon^1 A_{11}+\epsilon^3 A_{31}+\epsilon^5 A_{51})\cosh(kz)\cos(\theta)\\ &+2(\epsilon^2 A_{22}+\epsilon^4 A_{42})\cosh(2kz)\cos(2\theta)\\ &+3(\epsilon^3 A_{33}+\epsilon^5 A_{53})\cosh(3kz)\cos(3\theta)\\ &+4(\epsilon^4 A_{44})\cosh(4kz)\cos(4\theta)\\ &+5(\epsilon^5 A_{55})\cosh(5kz)\cos(5\theta)\big]\end{aligned} \tag{4.12}$$

The total wave acceleration $a(x,z,t)$ is given in equation 4.13 [49]. Here is the vertical wave velocity $v(x,z,t)$ determined from the velocity potential function as well. The derivation of these terms is rather straightforward and added to Appendix C for convenience.

$$a(x,z,t) = \frac{Du}{Dt} = \frac{\partial u}{\partial t} + u\frac{\partial u}{\partial x} + v\frac{\partial u}{\partial z} \tag{4.13}$$

The water elevation $\eta(x,t)$ will change over time and position as well, and is determined with equation 4.14 [48]. The coefficients B_{ij} are described by Fenton and can be found in Appendix C.

$$\begin{aligned}\eta(x,t) = \frac{1}{k}\big[&(\epsilon+\epsilon^3 B_{31}-\epsilon^5(B_{53}+B_{55}))\cos(\theta)\\ &+(\epsilon^2 B_{22}+\epsilon^4 B_{42})\cos(2\theta)\\ &+(-\epsilon^3 B_{31}+\epsilon^5 B_{53})\cos(3\theta)\\ &+(\epsilon^4 B_{44})\cos(4\theta)\\ &+(\epsilon^5 B_{55})\cos(5\theta)\big]\end{aligned} \tag{4.14}$$

A final required input for these equations is the wave number k. The wave number is described with a transcendental equation given in 4.15 [48], in which the dimensionless factors C_n depend on depth and wave number, given in Appendix C.1. This transcendental equation has to be solved iteratively for given wave height, wave period and water depth. The Python module root is used in the parametric load model to solve this equation.

$$C_0+\epsilon^2 C_2+\epsilon^4 C_4 = \frac{2\pi}{T_p\sqrt{gk}} \tag{4.15}$$

The calculation of the wave kinematics in the parametric design tool are verified using a tool developed by Fenton, as described in Appendix C.2. Considering the wave described previously for the Borssele case, on position $x=0$, the wave height, wave velocity and acceleration at water level for two wave periods are shown in figure 4.1.

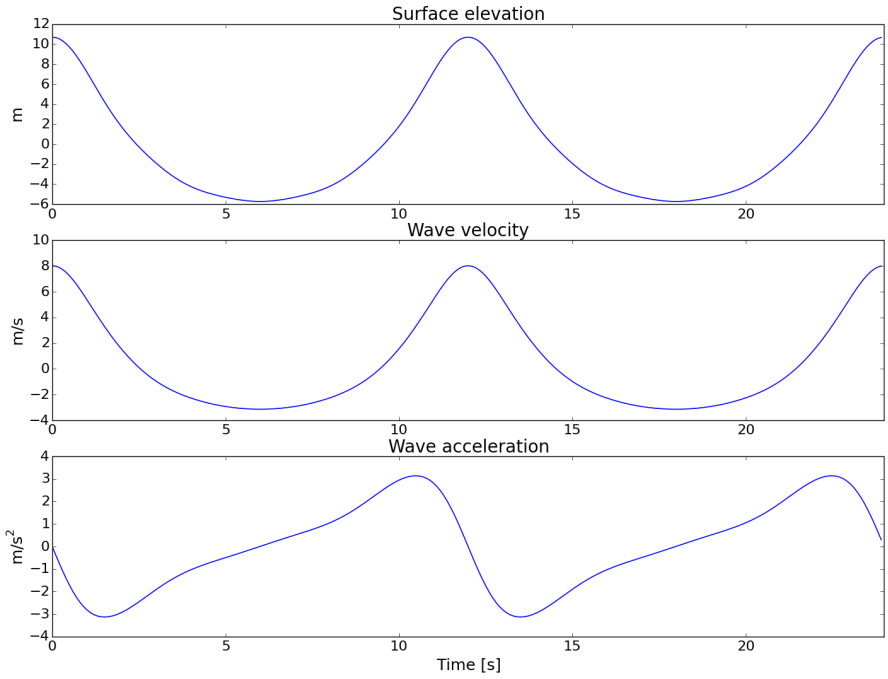

Figure 4.1: Wave height, velocity and acceleration as function of time

4.2.2. Morison's equation

The wave loading on the support structure is determined with Morison's equation as given in 4.16. The wave loading consists of a drag and inertia term, depending on the wave velocity and acceleration, as determined according to the method described before. respectively. Furthermore, the wave loading depends on the water density ρ_w, the diameter of the pile D_p, drag coefficient $C_{D,p}$ and inertia coefficient C_m. The determination of these coefficients is load case dependent and is explained in more detail in Appendix C. However, for simplicity, the drag coefficient and inertia coefficient will be assumed to have a default value of 0.7 and 2.0 in the load estimation model.

$$\delta F_w(z,t) = \frac{1}{2}\rho_w D_p C_{D,p} u(x,z,t)\left|u(x,z,t)\right| + C_m \rho_w \frac{D_p^2}{4} a(x,z,t) \tag{4.16}$$

The resulting hydrodynamic force can be determined by integrating the Morison equation from seabed till wave crest height ($\eta(x,t)$), as given in Equation 4.17. In the parametric model, the wave loading is assumed to be constant over length for each finite element.

$$\int_{-d}^{\eta} \delta F_w(z,t)\,dz \tag{4.17}$$

As can been seen in figure 4.1, the maximum velocity and acceleration do not occur at the same time. Therefore, one cannot just fill in the maximum wave velocity and acceleration in the Morison equation to find the maximum loading on the structure. The Keulegan-Carpenter (KC) number, determined with equation 4.18, can be used to identify the dominating force.

$$KC = \frac{u_{max} T_p}{D_p} \tag{4.18}$$

Considering the 50 year maximum wave height at the Borssele III location and a monopile diameter of five meter, the shear force at mudline over one wave period due to the drag and inertia force is shown in figure 4.2.

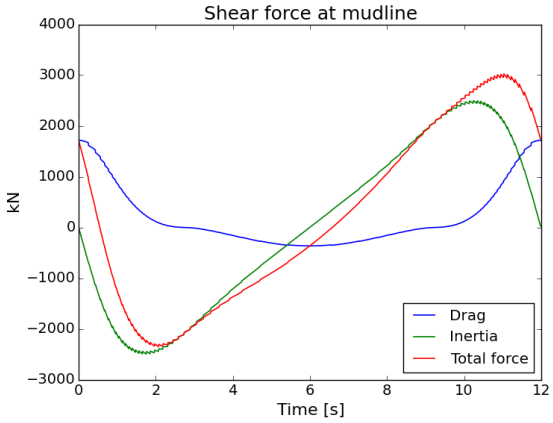

Figure 4.2: Shear force at mudline

As can been seen, the maximum total force is approximately 3000 kN, 20% higher than the maximum inertia force (2500 kN). Therefore, drag can not be neglected in this case. For a KC smaller than 5, the inertia force will be dominating [37] and the drag term can be neglected. Filling in the wave parameters of the 50 year maximum wave height in equation 4.18, the KC number will be below 5 if the monopile diameter exceeds 16 meter. This is not expected for a monopile design and therefore the drag term can not be neglected. As can been seen in figure 4.2, the time instant of maximum loading at the mudline does not coincide with the time instant of maximum inertia loading or drag loading. Therefore, a complete wave period will be analyzed after which the time instant of maximum wave loading at mudline will be used for the determination of maximum loading in the ULS analysis.

4.3. Dynamic loading

The dynamic effects of the wave loading can be taken into account by mean of a Dynamic Amplification Factor (DAF), as often used in a preliminary design stage [33]. The DAF can be determined with Equation 4.19 [10]. In this equation, f is the excitation frequency and f_0 the natural frequency, and ξ the damping ratio.

$$DAF = \frac{1}{\sqrt{(1-(\frac{f}{f_0})^2)^2 + (2\xi\frac{f}{f_0})^2}} \tag{4.19}$$

This damping ratio consists of material, soil, hydrodynamic and aerodynamic damping, where the latter one has the most contribution. The aerodynamic damping in fore-aft direction is larger than the damping in side-side direction. This damping is determined with blade element moment theory, which is not available in this tool. An estimation of the total damping can be made as well, where it is suggested [40] to use a fore-aft damping for a operational turbine between 2% and 8% and for a parked turbine a value between 1% and 4%. In [37] it is mentioned that a lot of research has been done on the estimation and determination of total damping ratio's which vary a lot and even a significant difference exists for measured damping ratios. In appendix D.2, the damping values for the three tower concepts used in this study are estimated by a stepwind load case. The damping ratio differs for each tower concept for each load case. Since it is not the scope of this project to find exact damping ratio's for each load case, the approximate values of 5% for an operational turbine and 2% for a parked turbine as used in [10] will be used here as well.

For a quasi-static evaluation of the wind loading, the wind speed can be decomposed into a mean wind speed $\bar{V}$ and a turbulent part v, as described in equation 4.20. The turbulent wind loading on the tower and the turbulent drag force of a parked turbine will be evaluated with Davenport's model [50].

$$V = \bar{V} + v \tag{4.20}$$

Assuming that the turbulent wind speed part is much smaller than the average wind speed, Davenport derived the relation as given in equation 4.21 for the total wind loading F_{wind} due to a mean wind loading F_q and fluctuating wind loading F_t. The mean wind loading on the parked turbine is given by equation 4.7 and

the mean wind loading on the tower is given by equation. 4.4. The turbulence intensity is described by I_v and the turbulence peak factor k_p has a value in the range 3 to 5 according to [50].

$$F_{wind} = F_q + F_t = F_q + k_p 2 I_v F_q \tag{4.21}$$

This turbulence intensity is site specific, and in case detailed data is missing a wind class can be used as defined in the standard [51]. The reference turbulence intensity I_{ref} is predefined at a reference wind speed of 15 m/s. According to [51], three turbulence classes can be distinguished. Turbulence class A, B and C with reference turbulence intensity of 15 m/s is 0.14, 0.12 and 0.10, respectively. The turbulence intensity for other wind speeds can be determined with equation 4.22. The standard deviation of the wind speeds σ_v depends on which turbulence model is used. For a Normal Turbulence Model (NTM) and an Extreme Turbulence Model (ETM), equation 4.23 and 4.24 can be used, respectively [10]. Here is V_{avg} the long term average wind speed at the site.

$$I_v = \frac{\sigma_v}{\bar{V}} \tag{4.22}$$

$$\sigma_{v,NTM} = I_{ref}(0.75\bar{V} + 5.6) \tag{4.23}$$

$$\sigma_{v,ETM} = 2 I_{ref}\left[0.072\left(\frac{V_{avg}}{2} + 3\right)\left(\frac{\bar{V}}{2} - 4\right) + 10\right] \tag{4.24}$$

For an operational wind turbine, the aerodynamic thrust of the rotor is calculated with equation 4.25. By [10] it was assumed that the pitch control can follow changes in wind speed that occur at a lower frequency than the maximum rotational speed of the turbine f_{1Pmax}, which is 0.16 Hz (9.6 RPM) for the Avatar 10 MW turbine. The turbulent wind speed part v can be determined with equation 4.26, where μ is the confidence interval of the standard deviation. The wind speed frequency spectrum depends on the integral length scale parameter L_k, which is assumed to have a constant value of 340.2 m [32].

$$F_T = \frac{1}{2}\rho_a A_R C_T (\bar{V} + v)^2 \tag{4.25}$$

$$v = \mu\sigma_{v,f>f_{1P}} = \mu\sigma_v \sqrt{\frac{1}{\left(\frac{6L_k}{\bar{V}_r} f_{1Pmax} + 1\right)^{\frac{2}{3}}}} \tag{4.26}$$

4.4. Load verification with Focus6

In this section, the load estimation model will be verified with time-domain simulations using Phatas [44], the integrated aero-elastic simulation tool in Focus6. The aero-elastic model of the Avatar 10 MW research turbine will be used. Three different tower concepts will be compared, to identify the differences between the quasi-static load estimation model and the effects of dynamic loading in the aero-elastic simulations:

- **Tower 1**: A stiff tower with a relatively high frequency, such that it can be considered quasi-static. It is expected that structural dynamics will have no influence on the loading on this design and therefore results close to the parametric load estimation model are expected.
- **Tower 2**: A steel-equivalent tower which represents current steel tower designs.
- **Tower 3**: A flexible tower with a natural frequency in the range of future GFRP tower. deigns.

Firstly, wind loading and wave loading will be compared separately in section 4.4.1 and 4.4.2, respectively. Then the wind and wave loading will be combined in section 4.4.3 and in section 4.4.4 the turbulence of the wind and DAF of the wave loading will be included. Finally, the maximum loading along the structure is determined in section 4.4.5. The load cases used in these comparisons are based on the load cases from the Borssele III wind farm location [21]. Some remarks have to be made regarding the time-domain simulations in Focus6:

- In Focus6, the tower dynamics are described by the modal response of the tower, using the Craig-Bampton method as described previously in section 3.3. In a dynamic time-domain simulation, the deformations of the structure are solved by the integration of the equations of motion, from which the internal stresses in the structure are solved. Potential and kinetic energy are interchanged and energy is extracted from the external forces during dynamic deformations. The internal forces and moments are directly related to the potential energy, but due to the exchange with kinetic energy this cannot be related directly to the external forces. In the quasi-static load analysis model, the internal forces are determined directly from the external forces, which will result in a different load distribution along the structure [52].

- Focus6 usually takes into account the structural flapping, edgewise and torsional deformation of the blades. These effects are not considered and are disabled for this comparison. In appendix D it is shown that the maximum loading along the support structure is affected negligibly by the blade deformations.

4.4.1. Constant wind loading

The aerodynamic thrust curve calculated with the previous described method of Frohboese & Schmuck is compared to the aerodynamic thrust curve of the Avatar 10MW turbine generated with Focus6, shown in figure 4.3. In the low wind speed (4-7 m/s) and high wind speed (12-25 m/s) regimes errors in the range of 20% are present. In the range up to rated wind speed (7 - 12m/s), errors up to 8% are present. To the knowledge of the author no other estimation methods are available and therefore this estimation method will be used in the parametric design tool. The aerodynamic thrust is estimated conservative at rated and cut-out wind speed, which are the conditions for which the ULS will be determined.

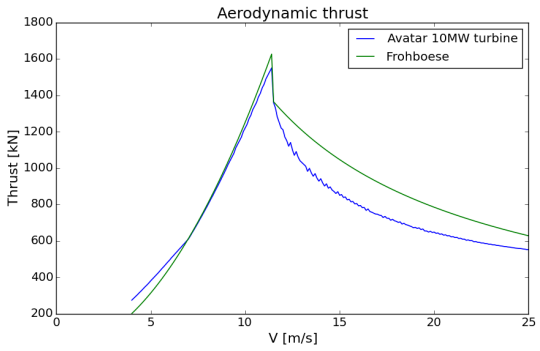

Figure 4.3: Aerodynamic thrust

For the verification of drag loading on the rotor and support structure, a load case with a constant wind speed of 50 m/s is analyzed for a duration of ten minutes. The first minutes are simulated to obtain a steady state, and the last two minutes will be used for the comparison. The tower geometry and stiffness terms of the three tower concepts are given in table 4.3. The aerodynamic thrust of the turbine in the time-domain simulations for the three tower concepts is shown in figure 4.4, together with the calculated drag loading using equation 4.7 in the load estimation model.

Table 4.3: Load case description as modelled in Focus6 and parametric model

Tower length	120 m
Tower outer diameter	5 m
Tower thickness	100 mm
Tower 1 (E = $210 \cdot 10^3$ GPa)	2.9068 Hz
Tower 2 (E = 210 GPa)	0.1883 Hz
Tower 3 (E = 90 GPa)	0.1171 Hz

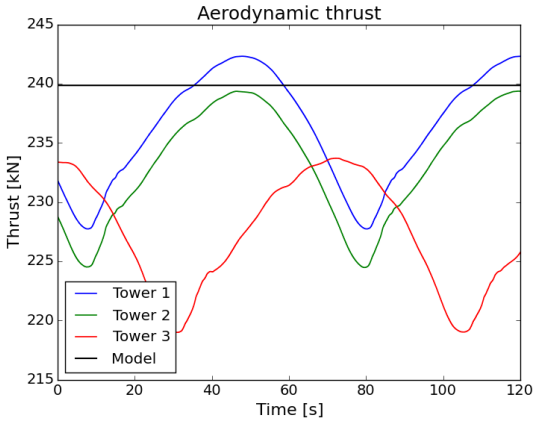

Figure 4.4: Aerodynamic thrust of the rotor in idling condition

In the simulations, the rotor is idling with a rotational speed of 0.28 RPM. The aerodynamic thrust is varying with a period of 71 seconds. This is a frequency of 0.014 Hz, three times the rotational frequency (0.28/60 = 0.0046 Hz). From this can be said that the drop in thrust occurs when a blade passes the tower. The rotor on a flexible tower produces less thrust due to the larger nacelle displacement compared with a stiff tower. The differences between the load estimation model and Tower 1, Tower 2 and 3 is 1%, 0% and -3%, respectively and considered to be negligible.

To verify the drag load along the structure, the shear force and bending moment at the root of the tower is shown in figures 4.5 and 4.6. The parametric model shows a constant shear and bending moment, while for the time-domain simulations variations are present. For the very stiff tower (Tower 1), only variation due to the variation of aerodynamic thrust is visible. The root shear and bending moment of Tower 2 and 3 vary with a period of 5.4 and 8.3 seconds, respectively, which indicate the first fore-aft natural frequencies of Tower 2 (0.1883 Hz) and Tower 3 (0.1171 Hz).

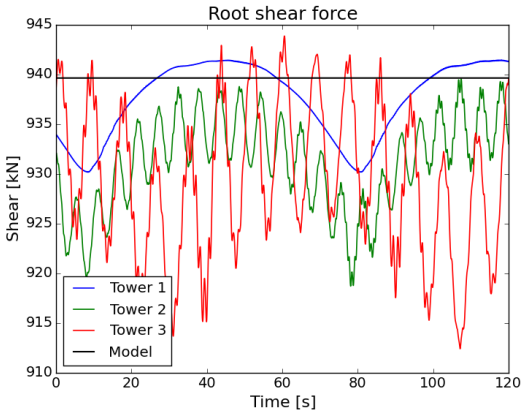

Figure 4.5: Shear force at root of tower

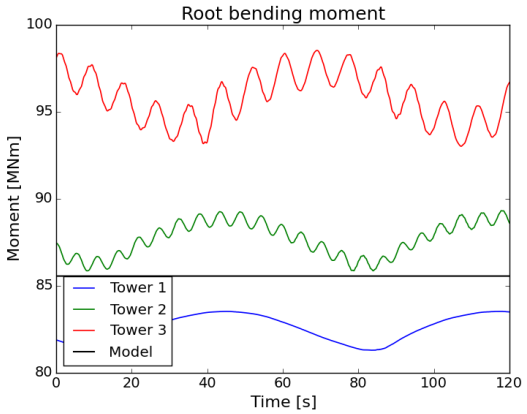

Figure 4.6: Bending moment at root of tower

The maximum shear force over time is approximately equal to the maximum shear force calculated with the parametric design model for all three towers. The bending moment shows larger differences, which can be explained by looking at the shear and bending moment distribution along the height of the structure. In figures 4.7 and 4.8, the shear and bending distribution at t=120 seconds is shown, respectively. The shear force distribution at this time instant is approximately the same for all three towers. However, the bending moment distributions show differences. First of all, a negative bending moment is present at the top of the tower, since the center of gravity of the RNA is not on top of the tower axis. For the determination of the exact center of gravity of the RNA, detailed turbine data would be required and therefore ignored in the parametric design model.

Another difference observed is the increased slope of the bending moment for Tower 2 and Tower 3. The acceleration and displacement of the nacelle shifts its center of gravity with respect to the tower axis over time causing an increased bending moment. This effect is larger for flexible towers. For Tower 1, which has a high stiffness, the displacement and acceleration terms are negligible; the difference in bending moment distribution with the load estimation model is approximately 2%. The difference in root bending moment between the parametric load estimation tool and for Tower 2 and 3 is 4% and 13%, respectively.

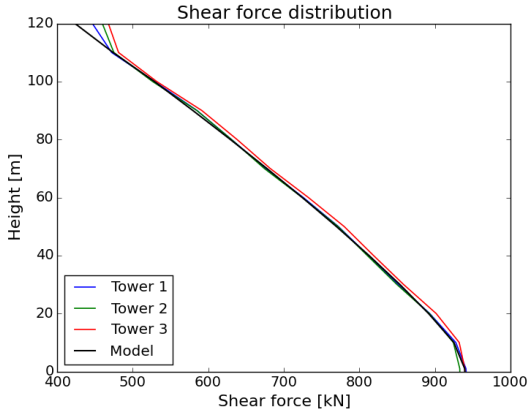

Figure 4.7: Shear force distribution at t=120 s

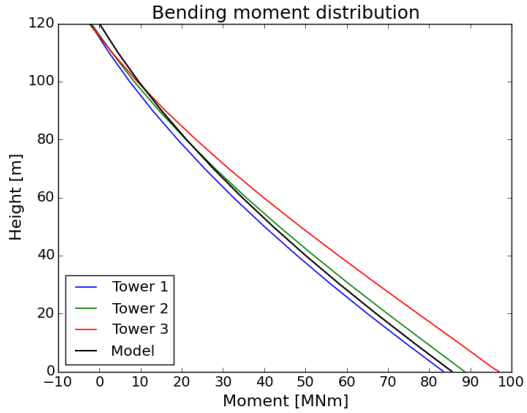

Figure 4.8: Bending moment distribution at t=120 s

From these results it is concluded that the parametric model determines the shear force and bending moment distribution due to a constant wind loading accurately for a very stiff tower. However, for flexible towers displacement and acceleration terms will increase the bending moment distribution along the height. Whether this effect should be included will be discussed when all sources of loading are combined.

4.4.2. Hydrodynamic loading

The calculation of the hydrodynamic loads on the support structure are compared with Focus6. Some remarks have to be made regarding the wave modelling in Focus6:

- Focus6 uses the program Streamfunction as method for determination of wave kinematics for a deterministic wave, based on the Fourier method described by Fenton as well [53]. Instead of a 5th order, a 11th order wave function is used. A comparison between the wave kinematics of Streamfunction and the load estimation model is given in appendix C.2 in which differences are found to be negligible.
- The structural dynamics of the tower incorporated in Focus6, will change the effective wave velocity and acceleration acting on the support structure. This effect is not taken into account in the load estimation model.

The length of the three tower concepts as given in section 4.4.1 will be increased by 35.1 meter corresponding to the water depth. The tower geometry and first fore-aft bending frequencies are given in table 4.4. Next to these natural frequencies, Focus6 generates as output the second and first three side to side natural frequencies. These are given in appendix D.1, together with the mode shape of the first two fore-aft mode shapes.

Table 4.4: Tower with artificial stiffness concepts

Tower length	155.1 m
Tower outer diameter	5 m
Tower thickness	100 mm
Tower 1 (E = $210 \cdot 10^3$ GPa)	2.2588 Hz
Tower 2 (E = 210 GPa)	0.1198 Hz
Tower 3 (E = 90 GPa)	0.0704 Hz

For the comparison of the hydrodynamic loading separately a load case is simulated with a wind velocity of 0 m/s. The 50 year maximum wave height of the Borssele III site will be used, as described before in section 4.2.

Three periods of the deterministic wave with a height of 16.42 meter and period of 11.99 seconds as created with the program Streamfunction are shown in figure 4.9. The load case is simulated for 600 seconds to reach a steady state solution, and the last completed wave period on the interval 587.51 - 599.5 seconds is used for the comparison.

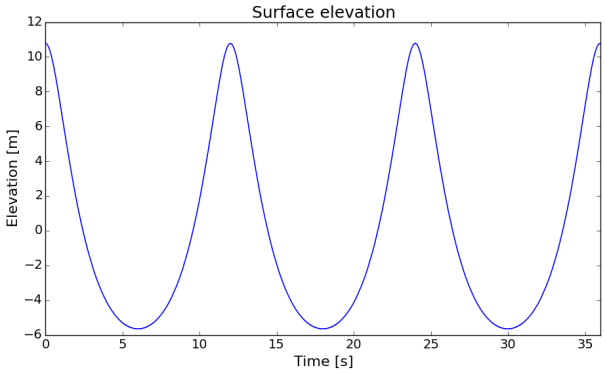

Figure 4.9: Surface elevation of wave created with Streamfunction

The simulation of Towers 1 and 2 converged to a steady state solution. In the simulation of Tower 3 resonance effects arose and no steady state solution was obtained and is therefore not included in this comparison. The resulting shear force and bending moment at the root is shown in figures 4.10 and 4.11, respectively.

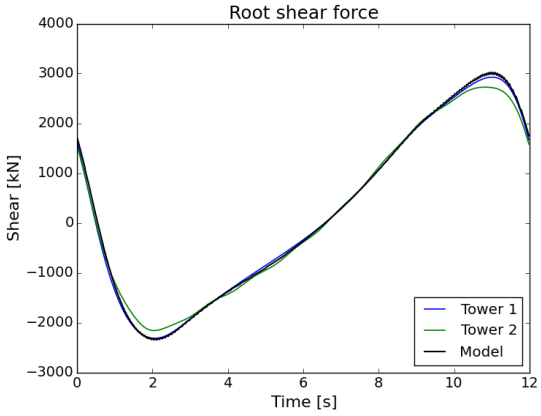

Figure 4.10: Shear force at mudline

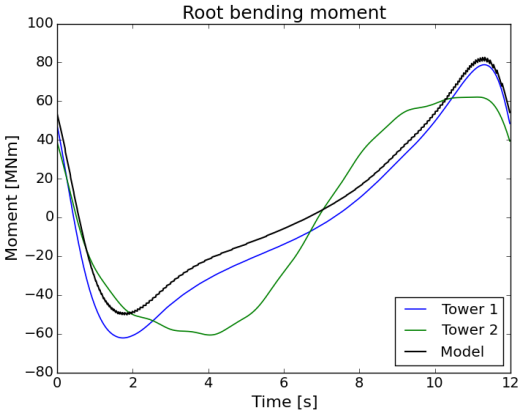

Figure 4.11: Bending moment at mudline

The shear force evolution over one wave period of the stiff Tower 1 is approximately equal to the shear force evolution calculated in the parametric load estimation model. The difference between the maximum shear force between these two is 3%. The shear force evolution of Tower 2 is approximately the same, except at the points of minimum and maximum shear where a difference of approximately 10% is present. The bending moment timeline of Tower 1 follows the same path as the bending moment of the parametric model, with a deviation around 1.75 seconds. The bending moment timeline of Tower 2 looks different, with a phase difference and lower minimum and maximum root bending moment. To analyze the differences, the shear force and bending moment distribution at minimum bending moment (t = 1.75 seconds) and maximum bending moment (t= 11.3 s) are shown in figures 4.12 - 4.15.

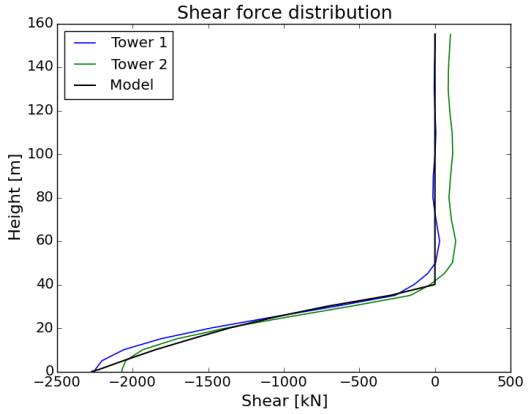

Figure 4.12: Shear force distribution at t = 1.75 s

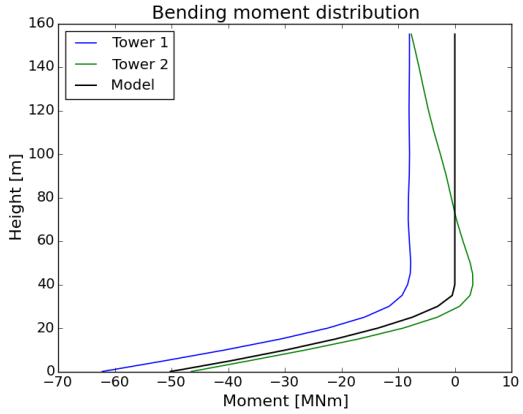

Figure 4.13: Bending moment distribution at t = 1.75 s

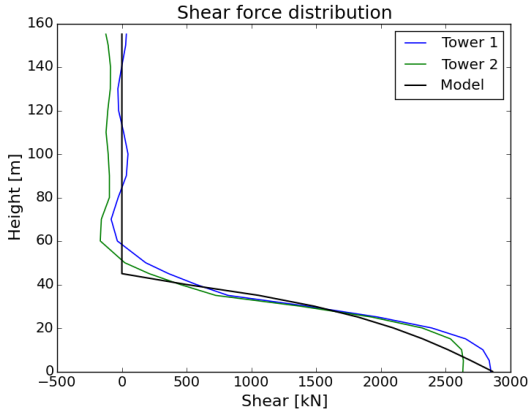

Figure 4.14: Shear force distribution at t = 11.3 s

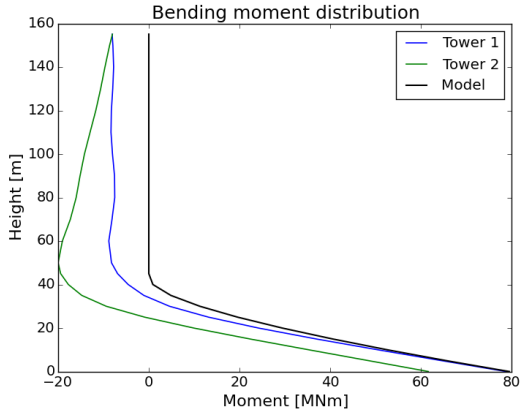

Figure 4.15: Bending moment distribution at t = 11.3 s

The differences between the shear force distribution of Tower 1 and the parametric model are close to each other. The bending moment distribution of Tower 1 and the parametric model is different due to the location of the center of gravity of the RNA as discussed in section 4.4.1. For Tower 2, the bending moment distribution is not constant and has a different path along the part above water. This is caused by the internal shear force, which is introduced at the top due to inertial (acceleration) effects. Young [7] mentioned that the inertial and gravitational forces are higher for a floating wind turbine than for a fixed support structure, because of greater structural motions. The same argument holds for a flexible tower, for which structural motions will be larger than for a stiff tower.

4.4.3. Constant wind and deterministic wave

In this section, the constant wind and wave loading will be added together. Two load cases will be analyzed; DLC 6.1 and DLC 1.6 at cut-out wind speed for the Borssele III site. The loading conditions are extracted from [21] and given in table 4.5. Again, the load cases are simulated for 600 seconds, of which the last wave period in the simulation is used for the comparison. For these load cases the simulations of Tower 3 converged to a steady state and is included in this comparison.

Table 4.5: Load case parameters

DLC	V [m/s]	H_m [m]	T_p [s]
6.1	50	16.42	11.99
1.6 cut-out	25	14.1	12.6

The root shear force and root bending moment over one wave period for DLC 6.1 are shown in figures 4.16 and 4.17. The same load evolution over time for Tower 1 and Tower 2 is present as for the load case without wind. In the shear force and bending moment evolution of Tower 3 another frequency is visible, which is the second fore-aft bending frequency of 0.5817 Hz as given in appendix D.1. No explanation has been found why this frequency is present for this specific tower concept in this loading condition. Normally, the first bending mode is the most dominant response mode, with minor contribution from higher modes [54]. Next to that, the bending moment at time instant of minimum loading is more than two times higher than for Tower 1.

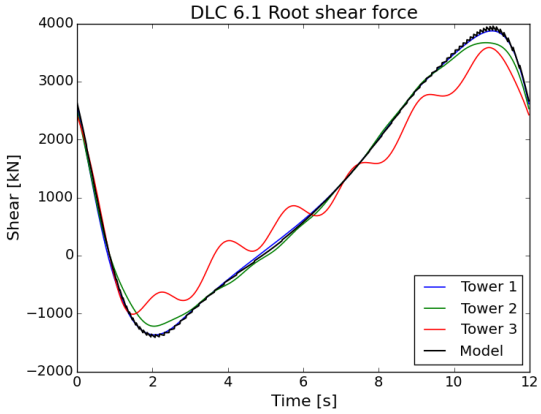

Figure 4.16: Root shear force

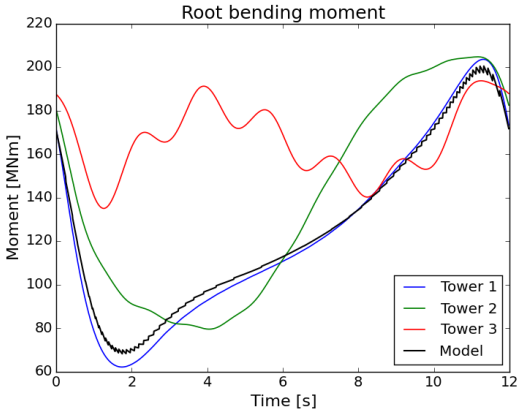

Figure 4.17: Root bending moment

The shear and bending moment distribution at the time instant of maximum root loading, at 11.3 seconds of the wave period, are shown in figures 4.18 and 4.19. At this time instant, the shear force distribution of Tower 1 and 2 is close to the shear force distribution of the load estimation model, while the shear force distribution of Tower 3 is lower above water level. The bending moment distribution along the structure is approximately equal for all three towers and the parametric model.

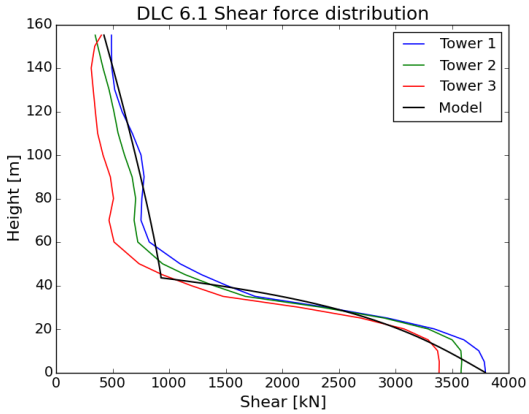

Figure 4.18: Shear force distribution at t = 11.3 s

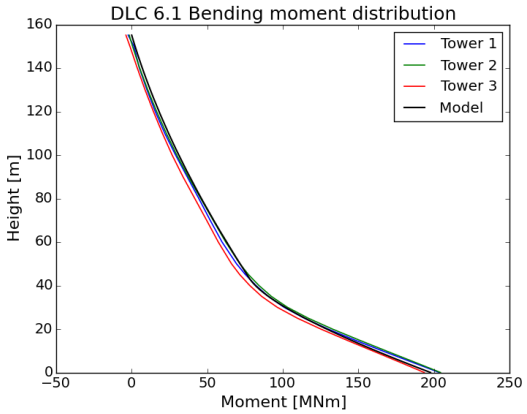

Figure 4.19: Bending moment distribution at t = 11.3 s

However, the shear and bending distribution at the time instant of minimal loading at t = 1.75 seconds looks different, as shown in figures 4.20 and 4.21. The internal shear force is larger for Tower 2 and Tower 3 than for Tower 1, starting at the top of the tower. This is due to the acceleration effects as discussed previously for the load case without wind, which induces a larger bending moment along the length of the tower.

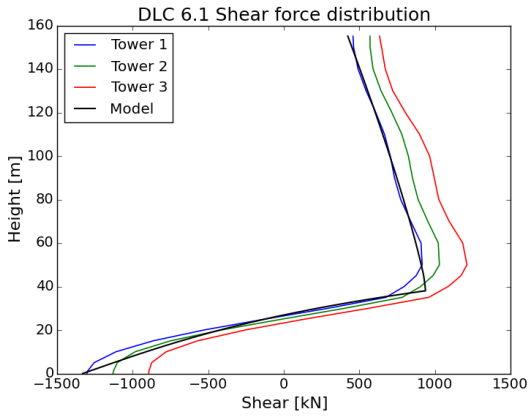

Figure 4.20: Shear force distribution at t = 1.75 s

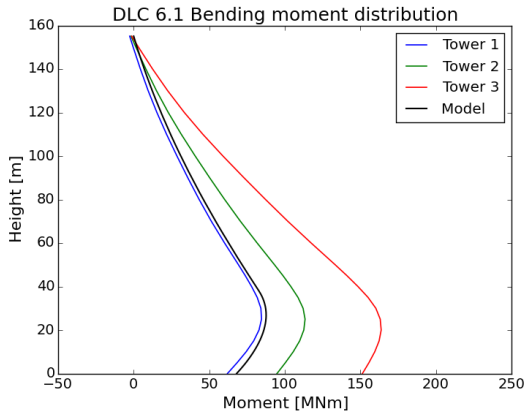

Figure 4.21: Bending moment distribution at t = 1.75 s

For this load case, the loading distribution calculated by the parametric model is approximately equal to the load distribution of Tower 1, with a maximum difference in root bending moment of 3%. However, for Towers 2 and 3 the model is less accurate. Although the maximum root bending moment is estimated with an accuracy of 3%, the maximum bending moment distribution along the length is underestimated. For these flexible towers, the maximum bending moment along the structure is not necessarily at the time instant at which the wave loading is maximal. This is caused by the aforementioned dynamic effects. For example, the maximum bending moment for Tower 3 at a height of 35 meter at time equals 1.75 seconds is 155 MNm, which is 80% higher than the bending moment at this location at time equals 11.3 seconds (86 MNm).

The shear force and bending moment evolution over one wave period at mudline for DLC 1.6 at cut-out wind speed are shown in figures 4.22 and 4.23. The same load evolution over time can be seen as previously for DLC 6.1. For Tower 1, a clear variation with the first fore-aft frequency is visible. The root shear force is approximately the same for all tower concepts and load estimation model, while the evolution of the root bending moment is different for the flexible Towers 2 and 3. In the parametric load estimation model, time of maximum and minimum bending moment for this load case was found at 11.57 seconds and 1.75 seconds respectively, for which the load distributions will be further analyzed.

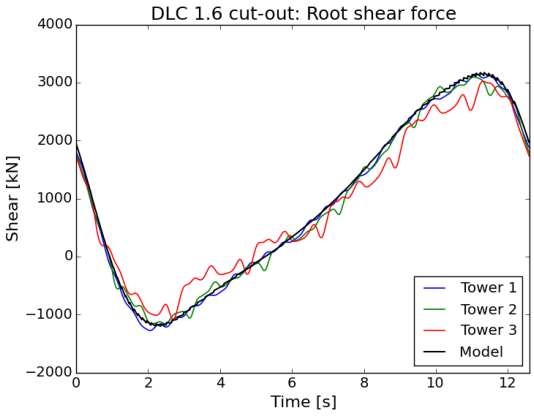

Figure 4.22: DLC 1.6 at V = 25 m/s root shear force over one wave period

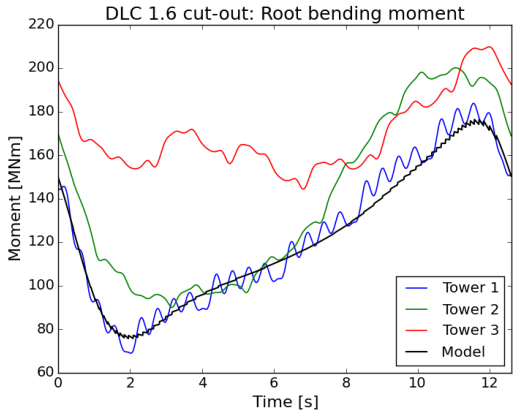

Figure 4.23: DLC 1.6 at V = 25 m/s root bending moment over one wave period

The shear and bending moment distribution at time instant 11.57 seconds is shown in figures 4.24 and 4.25. Again, the shear force distribution of Tower 1 and 2 is close to the shear distribution of the load estimation model, while the internal shear of Tower 3 is lower. The bending moment distribution of Tower 1 is approximately equal to the load estimation model, while the bending moment distribution of Tower 2 and Tower 3 is underestimated by 5% and 19%, respectively. As mentioned in section 4.4.1, the larger bending moment for more flexible towers is induced by the larger nacelle displacement. The root bending moment of Tower 2 and Tower 3 is 9 MNm and 26 MNm higher than for Tower 1 at this time instant. While the nacelle displacement

of Tower 1 equals zero, the displacement of Tower 2 and Tower 3 at this time instant are 1.27 and 3.17 m. With a RNA mass of approximately 702 tonnes, this will result in an increased bending moment of 9 MNm and 22 MNm at the root for Tower 2 and Tower 3, respectively. From this it is concluded that the increased slope of bending moment distribution is partially induced by the larger nacelle displacement for flexible towers.

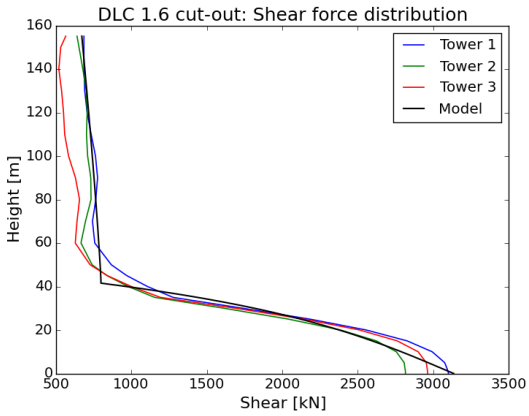

Figure 4.24: Shear force distribution at t = 11.57 s

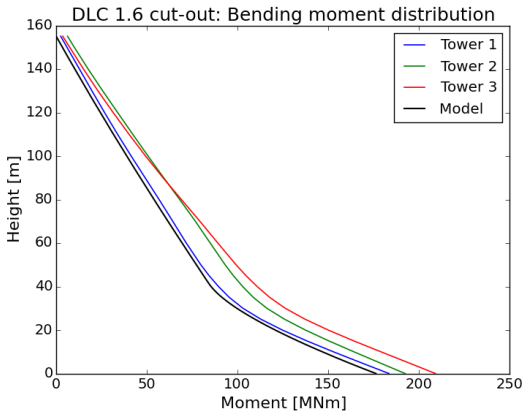

Figure 4.25: Bending moment distribution at t = 11.57 s

The time instant of minimum loading at the mudline in the parametric model is found at 1.75 seconds, while the bending moment at mudline for the flexible tower is much higher at this instant. The shear force and bending moment distribution are shown in figures 4.26 and 4.27. Again, as was shown already for DLC 6.1 at an idling condition, the maximum bending moment distribution along the support structure is not necessarily at the time instant of maximum wave loading due to the dynamic behaviour of the structure.

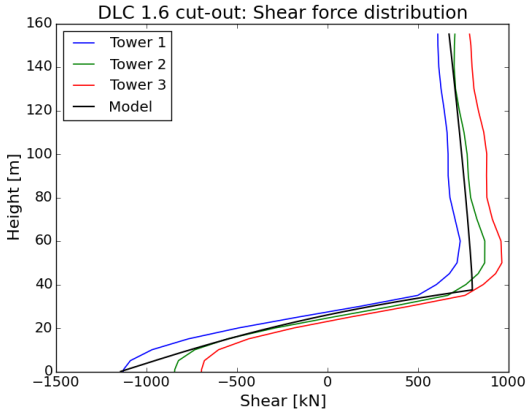

Figure 4.26: Shear force distribution at t =1.75 s

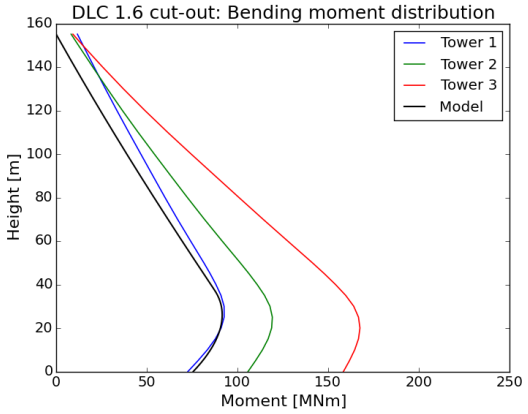

Figure 4.27: Bending moment distribution at t = 1.75 s

From these two load case analyses with constant wind and wave loading, it can be said that the load estimation model determines the loads accurately for a quasi-static tower. However, the bending moment distribution will increase up to 19% for flexible towers, partly induced by the larger nacelle displacement. Next to that, due to dynamic effects, the time instant of maximum wave loading is not the time instant of maximum loading along the complete structure for flexible towers.

4.4.4. Turbulence and DAF

In this section, turbulent wind loading and the DAF will be added to the load comparison. A parked (DLC 6.1) and two operational load cases at rated and cut-out wind speed (DLC 1.6) as described in table 4.6 will be analyzed. In Focus6, a turbulent wind field is generated with the random wind field simulator SWIFT-R [55]. For this load comparison, six different simulations with different turbulent wind fields will be analyzed. Each simulation takes 630 seconds, of which the first thirty seconds will not be taken into account due to start up effects. From these simulations, the maximum bending moment and corresponding internal shear force at this time instant at a number of stations along the height is extracted.

In the parametric load estimation model, turbulence is taken into account as described in section 4.3. For DLC 6.1, turbulence is included with an EWM, for which a turbulence intensity of 0.11 is valid [32]. For both DLC 1.6 load cases a NTM is valid with a reference turbulence intensity of 0.14. For the hydrodynamic loading, the time instant of maximum bending moment at mudline is used in the parametric load estimation model. The bending moment due to the hydrodynamic loading is now multiplied with the DAF, according equation 4.19.

Table 4.6: Load cases

DLC	$\bar{V}$ [m/s]	Wind Model (I_v)	H_m [m]	T_p [s]	Tower 1 DAF	Tower 2 DAF	Tower 3 DAF
6.1	50	EWM (0.11)	16.42	11.99	1.00	1.94	2.46
1.6 cut-out	25	NTM (0.136)	14.1	12.6	1.00	1.77	3.41
1.6 rated	11.4	NTM (0.174)	7.9	9.2	1.00	5.03	0.72

In figure 4.28, the shear force distribution along the structure for DLC 6.1 is shown corresponding with the time instant of maximum bending moment, which is shown in figure 4.29. As can been seen, the internal shear force distribution is not a smooth line. This is due to the fact that not a single load case simulation run was dominant along the complete structure, which is shown in appendix D.3.

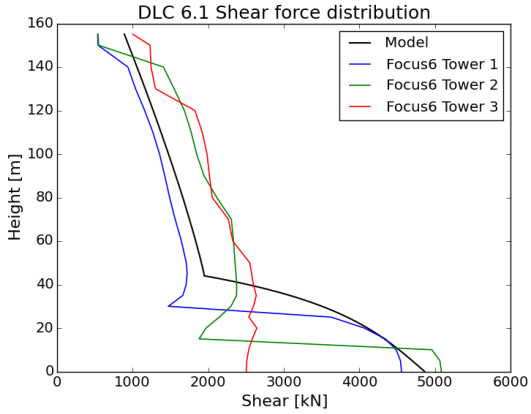

Figure 4.28: Shear distribution along structure

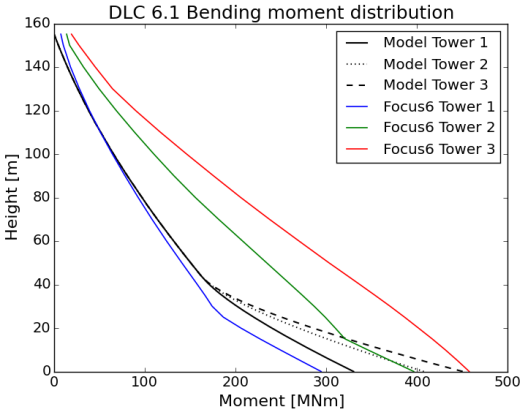

Figure 4.29: Maximum bending moment along structure

The bending moment distribution is highest for the most flexible Tower 3 and lowest for the most stiff Tower 1. This higher bending moment for the flexible Towers 2 and 3 is related to the internal shear distribution. The internal shear force is higher for the more flexible Towers 2 and 3 on the part above water, causing a higher bending moment. The internal shear force of the flexible Towers 2 and 3 is lower on the submerged part of the structure than for Tower 1. Just as for the load cases with constant wind, it can be concluded that the time instant of maximum wave loading is not necessarily the time instant of maximum loading along the complete structure for a flexible tower. The bending moment distribution calculated with the load estimation model is quiet accurate for Tower 1, with an overestimation on the submerged part of the structure. Using the time instant of maximum hydrodynamic bending moment in the load estimation model is therefore a conservative approach for a load case with a turbulent wind field. The slope of the bending moment of Tower 2 and Tower 3 is underestimated along the part above water. This is not covered by the application of the DAF applied on the submerged part of the structure only. The slope of the bending moment is overestimated on this part of the structure, while the dynamic interaction of turbulent wind and wave loading has an effect on the loading distribution along the complete structure.

The second load case analyzed is DLC 1.6 at rated wind speed. In the parametric load estimation model, the aerodynamic thrust is now calculated with equation 4.23, 4.22 and 4.26. For this load case a NTM will be used. Since it is not expected that the wind speed will vary significantly within the time of one revolution of the rotor, a confidence interval of 90% is assumed for the turbulent wind speed determination, resulting in a turbulent wind speed of 0.82 m/s. In figures 4.30 and 4.31, the maximum bending moment and corresponding shear force distribution are shown.

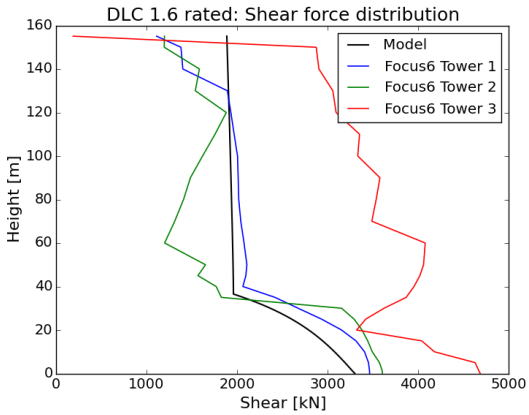

Figure 4.30: Shear distribution along structure

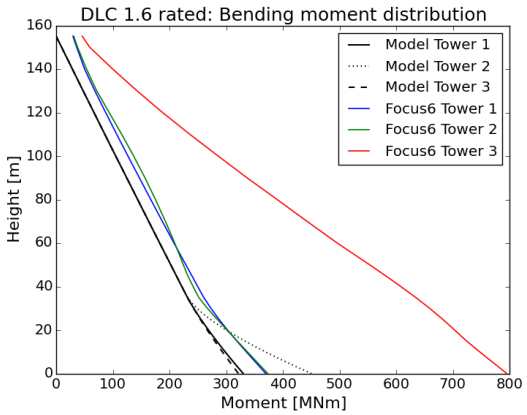

Figure 4.31: Bending distribution along structure

Again, the corresponding shear force with time instant of maximum bending moment shows large shifts along the structure, and thus not a single simulation run was dominant. The slope of the bending moment distribution of Tower 3 is much higher compared to Tower 1 and 2, resulting in a root bending moment twice as high. Resonance effects were observed for this tower in the time-domain simulations. The resonance effects in this load case can be solved with the wind turbine controller, which will be explained later in this section.

Comparing the results of the load estimation model with the aero-elastic simulations of Tower 1 and Tower 2, it can be seen that a tower top bending moment of approximately 30 MNm is missing, which will be explained later in this section. The slope of the bending moment of the bending moment is approximately equal to the simulation results. However, for Tower 2 the slope is overestimated on the submerged part due to the DAF.

Thirdly, DLC 1.6 at cut-out wind speed is analyzed. Again, the aerodynamic thrust is calculated with equation 4.23, 4.22 and 4.26 in the load estimation model. During the ten minutes, the turbine will stay in operational condition and therefore a confidence interval of 99.7% is used for the wind speed variation, for which μ in equation 4.26 equals 3.0. This results in an added turbulent wind speed of 3.3 m/s for the calculation of the aerodynamic thrust. In figures 4.32 and 4.33, the bending moment distribution and corresponding shear force distribution are shown.

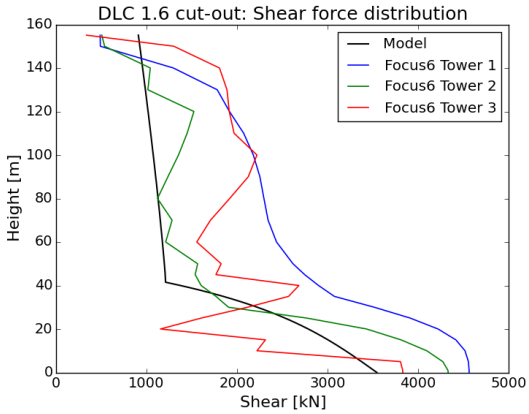

Figure 4.32: Shear distribution for DLC 1.6 at 25 m/s

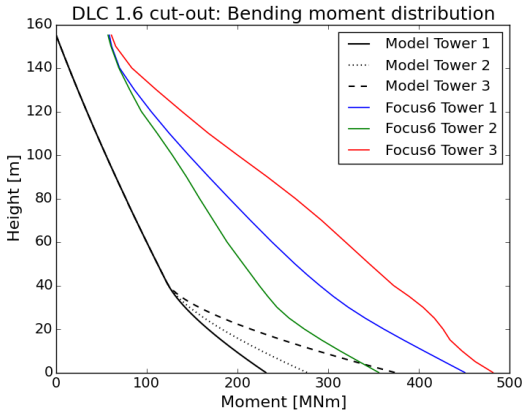

Figure 4.33: Moment distribution for DLC 1.6 at 25 m/s

Again, the shear force distributions show large shifts and not one single time instant results in the maximum bending moment along the complete structure. Just as for the other two load cases, the flexible Tower 3 has the highest bending moment distribution. For this load case, the slope of the bending moment is higher for Tower 1 than for Tower 2, vice versa with respect to the two previously analyzed load cases. Therefore, it can not be said that structural flexibility and larger nacelle displacements for flexible towers, as found in section

4.4.3, results in a higher bending moment distribution for turbulent load cases by definition.

Comparing the results of the load estimation model with the aero-elastic simulations, the slope of the bending moment of the load estimation model is approximately equal to the simulation results of Tower 2. The slope Tower 1 and Tower 3 is underestimated. Apart from this, the bending moment distribution is underestimated since a top bending moment of approximately 60 MNm is missing for all three towers. The origin of this tower top bending moment is examined in more detail.

Tower top bending moment
For all three load cases, a tower top bending moment is present in the results of the aero-elastic simulations, highest at cut-out wind speed. Since the maximum tower top bending moment is approximately equal for all three towers, it can be concluded that it is not affected by the flexibility of the support structure.

Vertical wind shear is one of the expected effects inducing this tower top bending moment. However, time-domain simulations without vertical wind shear result in a tower top bending moment of 47 MNm, and therefore it is concluded that this is not the only cause. To identify the effects of turbulence on the tower top bending moment, a comparison is made by simulating a turbulent wind field and a constant wind field at cut-out wind speed in Focus6. Hydrodynamic loading is excluded. The tower top bending moment and rotor shaft bending moment are shown on the one minute interval in which the maximum top bending moment was found in figures 4.34 and 4.35.

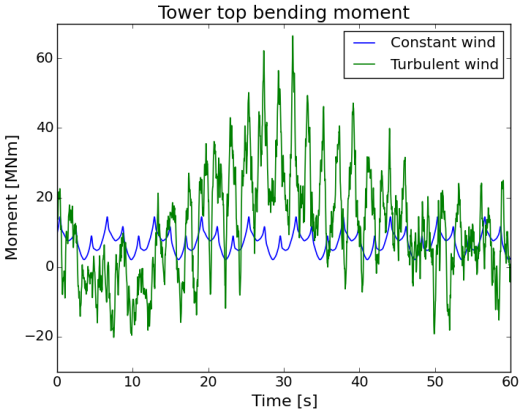

Figure 4.34: Bending moment in top of the tower

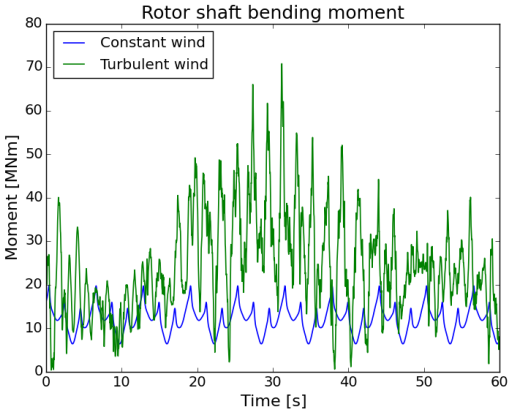

Figure 4.35: Resulting bending moment in rotor shaft

As can been seen, the resultant bending moment in the rotor shaft has the same profile as the tower top bending moment, from which it is concluded that the tower top bending moment is determined by the resulting bending moment in the rotor shaft, caused by the blades. The tower top bending moment varies periodically with a 3P period for the constant wind load case, with a maximum of approximately 15 MNm. The bending moment in the tower top for the turbulent wind load case shows more variation, with a maximum at 31.2 seconds. The wind velocity and wind direction on this time interval are shown in figures 4.36 and 4.37. At time instant 31.2 seconds, the wind misalignment is at its maximum, while the wind velocity is not within this time interval. Therefore it is concluded that the tower top bending moment is caused by a wind misalignment. To the knowledge of the author, no quasi-static evaluation of the bending moment in rotor shaft due to a turbulent wind field does exist and will be disregarded in the parametric load estimation tool.

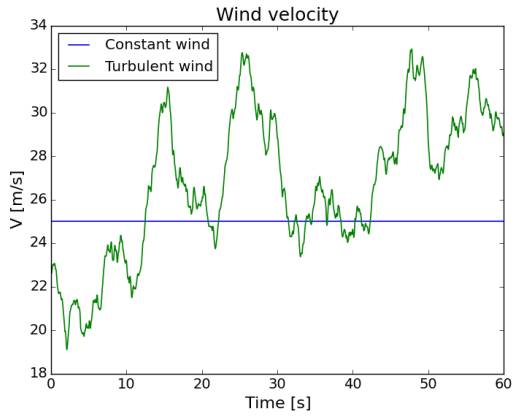

Figure 4.36: Wind velocity at hub height

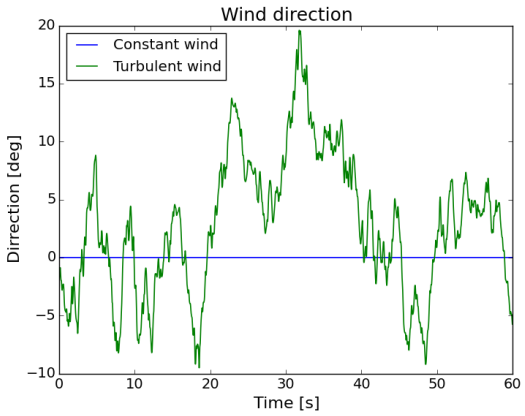

Figure 4.37: Wind direction at hub height

Influence of controller

DLC 1.6 at rated and cut-out wind speed are in the operational regime, and therefore the wind turbine controller will influence the loading along the structure. As mentioned earlier, the default controller of Focus6 is used for all three tower concepts. However, for Tower 3 resonance effects were observed. Within a different project at the company Jules Dock a wind turbine controller was designed by ECN part of TNO for flexible support structures with a frequency of approximately 0.09 Hz. A comparison is made for the maximum bending moment distribution along the structure between the default controller and the ECN controller for the three tower concepts. Note that the frequency of the three tower concepts are not exact at the design frequency of the controller, and therefore the controller is not expected to be optimal for these tower designs. The resulting bending moment distributions for DLC 1.6 at rated and cut-out wind speed are shown in figures 4.38 and 4.39, respectively.

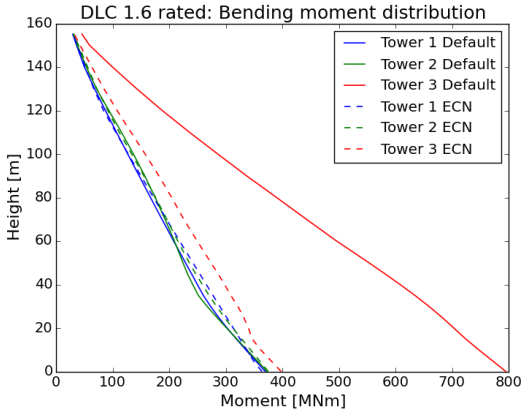

Figure 4.38: Moment distribution for DLC 1.6 at rated wind speed, Default vs ECN controller

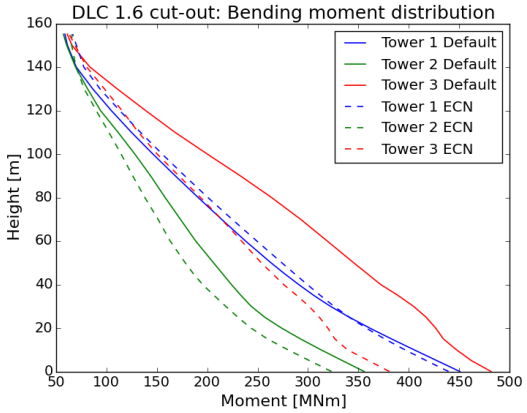

Figure 4.39: Moment distribution for DLC 1.6 at 25 m/s, Default vs ECN controller

For Tower 1, the maximum bending moment for both load cases remain approximately the same. For Tower 2, the root bending moment for DLC 1.6 at rated wind speed is the same as well, while for DLC 1.6 at cut-out wind speed a reduction of 9% is achieved. For Tower 3, the maximum bending moment is reduced significantly for both production load cases. The root bending moment for DLC 1.6 at rated and cut-out wind speed is reduced by 50% and 21% respectively by the use of this controller and is even lower than the bending distribution of Tower 1. For a fair comparison of the maximum loading of Tower 3, the results of the simulations with the ECN controller will be used in section 4.4.5.

4.4.5. Maximum loading

In this section, the maximum loading on the support structure will be determined according to the three load cases as described in section 4.4.4 with the parametric load estimation tool and will be compared to the maximum loading according to aero-elastic simulations in Focus6. Only the bending moment will be considered, since this load is the dominant force along the structure [52], which is found as well in the the results for the bending moment and shear distribution along the structure in section 4.4. In section 4.4.4, the largest bending moment in the six simulations was used for comparison. The randomness of turbulence gives different results between the different seeds, whose differences are largest for DLC 6.1 for the flexible towers, as can been seen in Appendix D.3. According to the design standards [32], the characteristic value for maximum loading is obtained with extrapolation methods, corresponding to a 50 year return value. Since this design tool will not be used for verification purposes and only different designs will be compared, the average and maximum loading along the structure of the different seeds will be used for comparison.

Tower 1

The average of the maxima found for all simulation runs and the maximum bending moment of the simulations runs and the bending moment distributions calculated with the load estimation model for Tower 1 are shown in figures 4.40 and 4.41, respectively. In the time-domain simulations of Focus6, the maximum bending moment is determined by DLC 1.6 at cut-out wind speed along the complete structure, while the maximum of the averages is shared by DLC 1.6 at cut-out and rated wind speed. DLC 6.1 does not have any influence on the maximum loading. In the load estimation model, DLC 1.6 at rated wind speed is the critical load case along the complete structure.

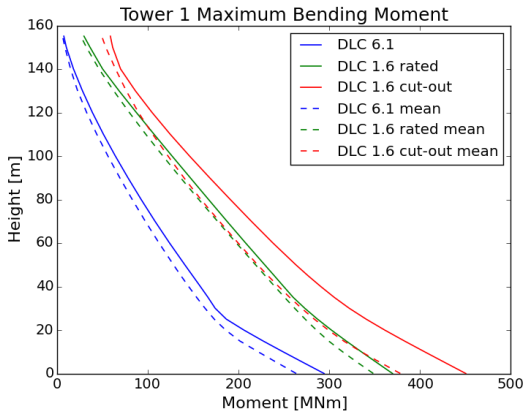

Figure 4.40: Maximum bending moment of Tower 1 in Focus6 simulations

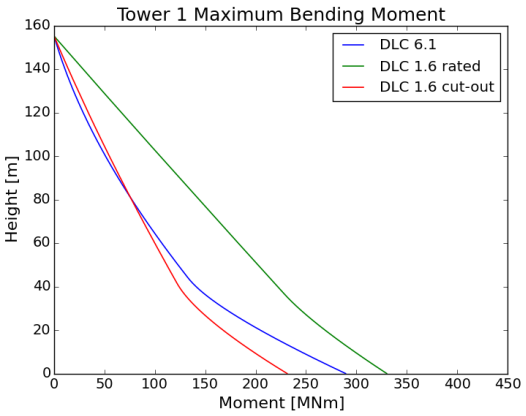

Figure 4.41: Maximum bending moment of Tower 1 in load estimation model

As found in section 4.4.4, a tower top bending moment is missing in the load estimation model for each load case. In figure 4.42 the top bending moments of 7 MNm (DLC 6.1), 30 MNm (DLC 1.6 rated) and 59 MNm (DLC 1.6 cut-out) found in the simulations are added to the results of the load estimation model. Now the top is dominated by DLC 1.6 at cut-out wind speed, and the remaining part by DLC 1.6 at rated wind speed.

In figure 4.43, the maximum of all load cases are combined. If the top bending moments are included, the maximum bending moment distribution found with the load estimation model is between the average and maximum found with the time-domain simulations, except for the bottom 20 meters.

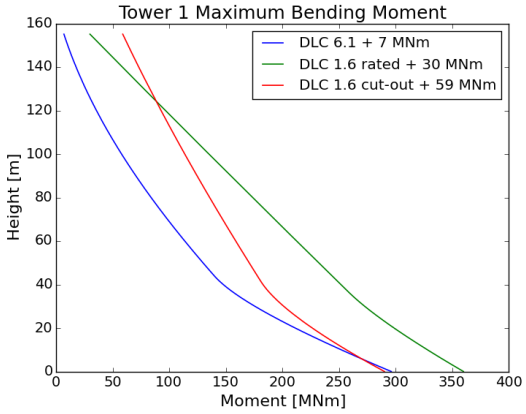

Figure 4.42: Maximum bending moment of Tower 1 in load estimation model with top bending moment

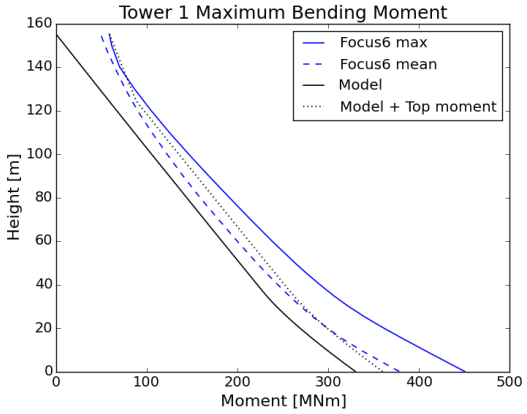

Figure 4.43: Maximum bending moment comparison of Tower 1 between Model and Focus6

Tower 2

In figure 4.44 and 4.45 the results of the simulations and the load estimation model are shown for Tower 2. In the time-domain simulations, DLC 1.6 at cut out gives the largest loading at the top, from 120 meter downwards till 60 meter DLC 1.6 at rated wind speed gives maximum bending moment and from 60 meter downwards DLC 6.1 will be determinative. Looking at the averages, DLC 6.1 will not be determinative. In the parametric load model, DLC 1.6 at rated wind speed gives the highest bending moment along the complete structure, same as for Tower 1.

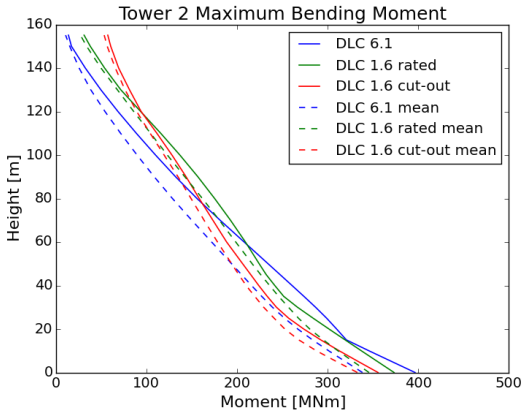

Figure 4.44: Maximum bending moment of Tower 2 in Focus6 simulations

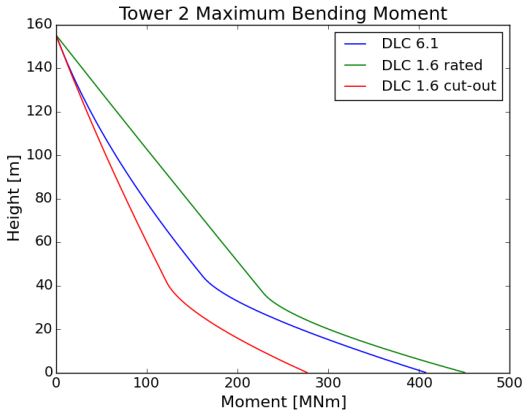

Figure 4.45: Maximum bending moment of Tower 2 in load estimation model

In figure 4.46 the top bending moments found in the simulations for DLC 6.1 (14 MNm), DLC 1.6 at rated wind speed (31 MNm) and DLC 1.6 at cut-out wind speed (57 MNm) are added to the bending moment distributions of the parametric load model. Just as for Tower 1, the top is dominated by DLC 1.6 at cut-out wind speed, while the remaining part is dominated by DLC 1.6 at rated wind speed.

In figure 4.47 the maximum bending moment of all three load cases along the structure are combined resulting in the maximal bending moment distribution. The results including the tower top bending moment is between the average and maximum of the time-domain simulations up till water level. As can been seen, the parametric load estimation model underestimates the bending moment distribution on the part above water level due to the missing tower top bending moment. The parametric load estimation results including these tower top bending moments is shown as well and is between the average and maximum of the Focus6 results up till water level. On the submerged part, the parametric load estimation model overestimates the slope of the bending moment due to the high DAF of DLC 1.6 at rated wind speed.

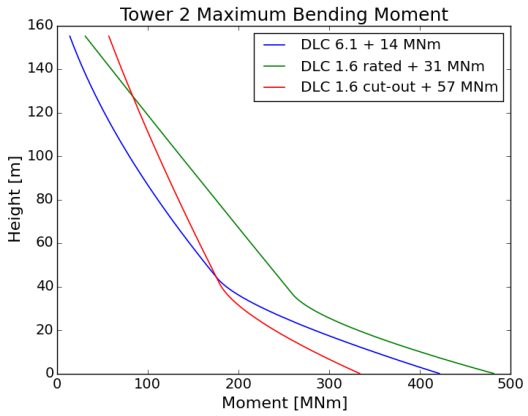

Figure 4.46: Maximum bending moment of Tower 2 in load estimation model with top bending moment

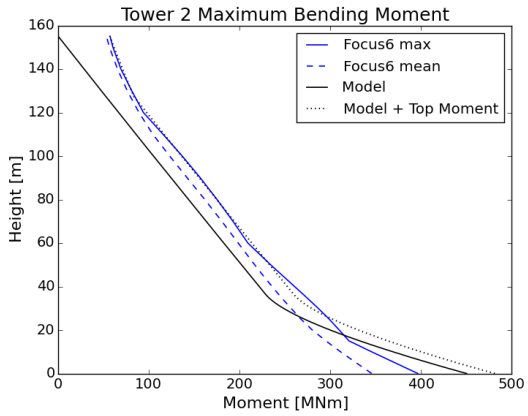

Figure 4.47: Maximum bending moment comparison of Tower 2 between Model and Focus6

Tower 3

As concluded in section 4.4, the results of the Focus6 simulations with the default controller showed resonance effects, which were solved by the implementation of the ECN controller. Therefore, the comparison of maximum loading of Tower3 will be made with the results of the time-domain simulations with this controller designed for flexible towers. As shown in figure 4.48, DLC 1.6 at cut-out wind is dominant at the top, while from 80 meter downwards DLC 6.1 is the determinative load case. The results of the load estimation model are shown in figure 4.49. DLC 1.6 at rated wind speed is dominant up till water level, where DLC 6.1 becomes dominant till the root.

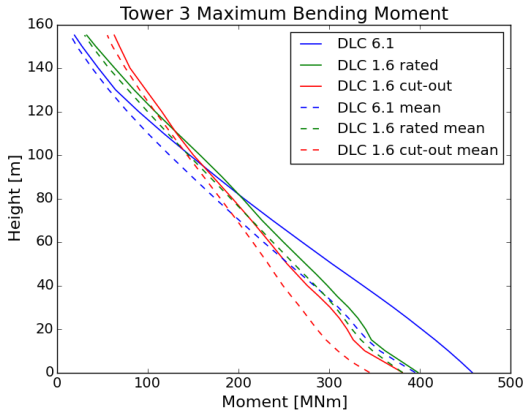

Figure 4.48: Maximum bending moment of Tower 3 with ECN controller

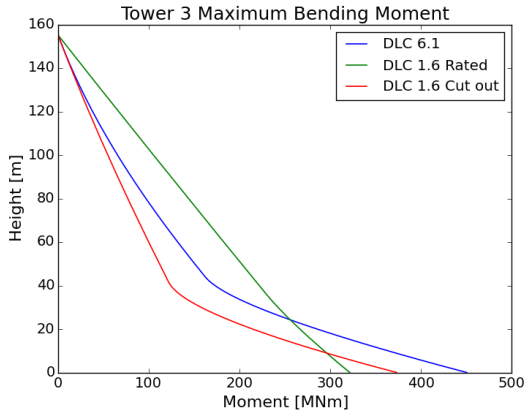

Figure 4.49: Maximum bending moment of Tower 3 in load estimation model

The tower top bending moments of the time-domain simulations are added to the results of the load estimation model, and shown in figure 4.51. Now, the top is dominated by DLC 1.6 at cut-out wind speed, from 120 till 35 meter is dominated by DLC 1.6 at rated wind speed and the submerged part is dominated by DLC 6.1.

In figure 4.51 the maximum bending moment of all three load cases combined is shown. For the results including the tower top bending moment, the load estimation model underestimates the loading from 80 meter downwards. This is caused by the underestimation of the bending moment distribution of DLC 6.1 on the part above water, while the slope of the bending moment is overestimated on the submerged part of the structure. A maximum difference is found at water level of 11% with respect to the average and 25% with respect to the maximum found in the time-domain simulations.

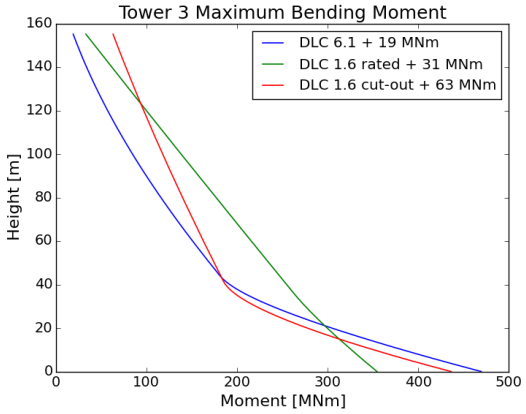

Figure 4.50: Maximum bending moment of Tower 3 in load estimation model with top bending moment

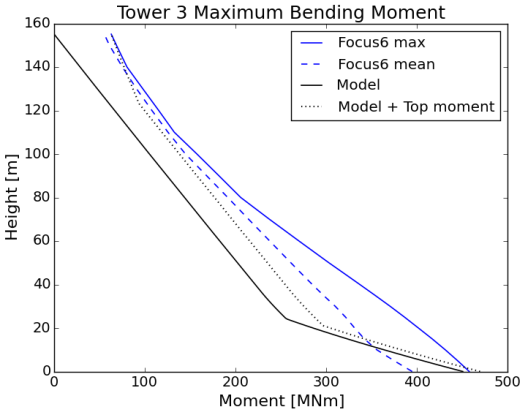

Figure 4.51: Maximum bending moment comparison of Tower 3 between Model and Focus6 with ECN controller

4.5. Conclusion

If the tower top bending caused by the turbulent nature of the wind is included in the load estimation model, the maximum bending moment distribution is estimated quiet accurately for a tower which can be considered quasi-static. For such a tower, dynamic interactions effects of the wind and wave loading are negligible, such that operational load cases will determine the maximum loading along the structure and DLC 6.1 has not an effect at all.

For flexible Towers, dynamic interaction effects will have an influence on the loading distribution, especially if the natural frequency is close to the wave excitation frequency. This dynamic interaction is included in the load estimation model by the application of the DAF. However, dynamic interaction influences the loading distribution along the complete structure, while the DAF is only applied on the submerged part. Therefore, the slope of the bending moment distribution is underestimated on the part above water, while the slope is overestimated on the submerged part. These effects might lead to an underestimation of the maximum loading on a flexible structure, since DLC 6.1 might determine the maximum loading along a substantial part of the support structure.

5

Structural Analysis Tool

In this chapter the structural analysis tool developed in the parametric design model is discussed. As explained in chapter 4, the dominant forces are the bending moment and axial compression load. Therefore, only these two loading components will be considered for the structural analysis. In section 5.1 the analysis of the steel monopile and transition piece is explained according the design standards. For the composite tower, a design standard is not yet available. The maximum stress and buckling analysis will be compared with the WMC FEM tool in section 5.2.

5.1. Steel monopile and transition piece

According to the DNV-OS-J101 standard [32], for the ULS requirement for the steel monopile and transition piece, the failure criteria that have to be assessed are the maximum yield, global and local buckling criteria. Steel S355 will be used in this analysis, which has a yield stress σ_{yield} of 355 MPa.

5.1.1. Yield stress analysis

The requirement for the yield criteria is given in equation 5.1. The material factor γ_M is 1.10. Assuming that the cross section will not deform due to loading and will remain planar, simple beam theory can be used. The maximum stress σ_{max}, a linear combination of axial stress σ_a and bending stress σ_m, for a simple beam can be determined with equation 5.2 [56]. In this equation, M_y is the maximum bending moment along the structure, as determined in section 4.4.5. N is the compressive axial load, which is caused by the mass of the RNA and the mass of the structure itself. Furthermore in this equation, r_m the radius till midplane and t the wall thickness of the cylinder.

$$\sigma_{max} < \frac{\sigma_{yield}}{\gamma_M} \tag{5.1}$$

$$\sigma_{max} = \sigma_a - \sigma_m = \frac{N}{2\pi r_m t} - \frac{M_y}{\pi r_m^2 t} \tag{5.2}$$

5.1.2. Buckling analysis

The buckling criteria is assessed according the DNV-RP-C202 standard, which are based on semi-empirical methods. The stability requirement for shells is given by equation 5.3. The material factor γ_M is for this case defined by equation 5.4, dependent on the slenderness of the shell $\bar{\lambda}_s$.

$$\sigma_{max} \leq \frac{\sigma_{cr}}{\gamma_M} \tag{5.3}$$

$$\begin{aligned} \gamma_M &= 1.15 && \text{for} \quad \bar{\lambda_s} < 0.5 \\ \gamma_M &= 0.85 + 0.6\bar{\lambda_s} && \text{for} \quad 0.5 \leq \bar{\lambda_s} \leq 1.0 \\ \gamma_M &= 1.45 && \text{for} \quad \bar{\lambda_s} > 1 \end{aligned} \tag{5.4}$$

The monopile will be considered as an unstiffened cylindrical shell. The critical buckling stress σ_{cr} is determined with equation 5.5, in which the shell slenderness $\bar{\lambda_s}$ is given by equation 5.6. The characteristic buckling strength for axial σ_{Ea} and bending loading σ_{Em} is determined with equation 5.7, where l_p is the length of the monopile or transition piece, for which the reduced buckling coefficient C is given by equation 5.8. The reduced buckling coefficient parameters ζ and ρ are load dependent and given in table 5.1. The curvature parameter Z_l is determined with equation 5.9.

$$\sigma_{cr} = \frac{\sigma_{yield}}{\sqrt{1+\bar{\lambda_s}^4}} \tag{5.5}$$

$$\bar{\lambda_s}^2 = \frac{\sigma_{yield}}{\sigma_{max}}\left[\frac{\sigma_a}{\sigma_{Ea}} + \frac{\sigma_m}{\sigma_{Em}}\right] \tag{5.6}$$

$$\sigma_{Ea,m} = C\frac{\pi^2 E}{12(1-\nu^2)}\left(\frac{t}{l_p}\right)^2 \tag{5.7}$$

$$C = \sqrt{1+(\rho\zeta)^2} \tag{5.8}$$

$$Z_l = \frac{l_p^2}{r_m t}\sqrt{1-\nu^2} \tag{5.9}$$

Table 5.1: Reduced buckling coefficient parameters

	ζ	ρ
Axial loading	$0.702Z_l$	$0.5\left(1+\frac{r_m}{150t}\right)^{-0.5}$
Bending loading	$0.702Z_l$	$0.5\left(1+\frac{r_m}{300t}\right)^{-0.5}$

5.2. Composite tower

For the composite material, the aforementioned methods for steel are not applicable, due to the anisotropic properties of the GFRP material. In the current design process of the composite tower, the stress and buckling in the composite tower are analyzed using the FEM program WMC FEM. However, finite element models are computationally expensive [57] and therefore analytical solutions will be included in the parametric model. The stress solutions of Lekhnitskii for a homogenized cylindrical composite structure [58] will be used and will be explained in section 5.2.1. This method requires homogenized elastic constants of the composite tower in the cylindrical coordinate system, given in figure 5.1.

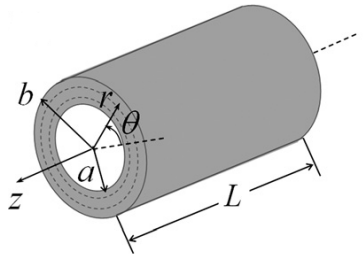

Figure 5.1: Tube coordinate system [58]

5.2.1. Stress analysis

The Lekhnitskii stress solutions are applicable for a homogenized hollow cylinder, for which the following assumptions have been made:

- The strains on the $\theta - z$ plane for each layer i ($\epsilon_\theta^{(i)}$, $\epsilon_z^{(i)}$ and $\gamma_{\theta z}^{(i)}$) are continuous through the thickness. The stresses ($\sigma_\theta^{(i)}$, $\sigma_z^{(i)}$ and $\tau_{\theta_z}^{(i)}$) through the thickness are discontinuous. For clarity, this is shown in figure 5.2.

- The tower is globally cylindrical orthotropic, which means that the elastic properties differ in three orthogonal directions. Next to that, the laminate layup should be balanced.

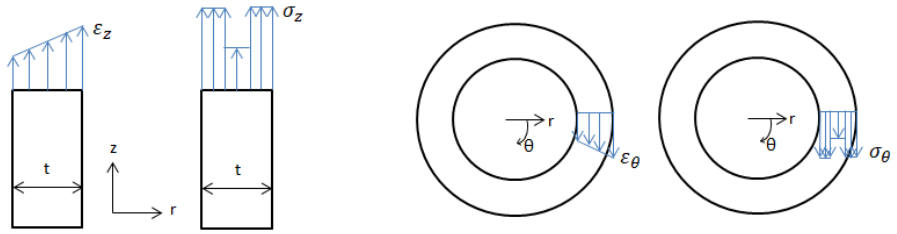

Figure 5.2: Stress and strains in z and θ direction

The homogenized stress solutions due to an axial load N and bending load M in the cylindrical coordinate system (figure 5.1) are given in equation 5.10 and 5.11, respectively.

$$\begin{aligned}
\sigma_r &= \frac{Nh(1-c_N^r)}{\Omega} \\
\sigma_\theta &= \frac{Nh(1-c_N^\theta)}{\Omega} \\
\sigma_z &= \frac{Nh(1-c_N^z)}{\Omega} \\
\tau_{\theta z} &= \tau_{rz} = \tau_{r\theta} = 0
\end{aligned} \tag{5.10}$$

$$\begin{aligned}
\sigma_r &= \frac{Mg(1-c_M^r)r\sin\theta}{K} \\
\sigma_\theta &= \frac{Mg(1-c_M^\theta)r\sin\theta}{K} \\
\sigma_z &= \frac{M(1-c_M^z)r\sin\theta}{K} \\
\tau_{r\theta} &= -\frac{Mg(1-c_M^r)r\cos\theta}{K} \\
\tau_{\theta z} &= \tau_{rz} = 0
\end{aligned} \tag{5.11}$$

In these equations, r is the radius of the tube and θ the hoop angle coordinate. The definition of the parameters h, g, Ω, K, c_N and c_M are lengthy and therefore added to appendix A.1. The input for these parameters is the homogenized compliance matrix $[\boldsymbol{S_h}]$, given in equation 5.12.

$$[\boldsymbol{S_h}] = \begin{bmatrix}
\frac{1}{E_r} & \frac{-\nu_{\theta r}}{E_\theta} & \frac{-\nu_{zr}}{E_z} & 0 & 0 & 0 \\
\frac{-\nu_{r\theta}}{E_r} & \frac{1}{E_\theta} & \frac{-\nu_{z\theta}}{E_z} & 0 & 0 & 0 \\
\frac{-\nu_{rz}}{E_r} & \frac{-\nu_{\theta z}}{E_\theta} & \frac{1}{E_z} & 0 & 0 & 0 \\
0 & 0 & 0 & \frac{1}{G_{\theta z}} & 0 & 0 \\
0 & 0 & 0 & 0 & \frac{1}{G_{rz}} & 0 \\
0 & 0 & 0 & 0 & 0 & \frac{1}{G_{r\theta}}
\end{bmatrix} \tag{5.12}$$

This matrix contains nine homogenized elastic constants for a homogenized hollow cylinder. Sun [58] proposed a method to determine these homogenized elastic constants by considering the composite tube as assemblies of multiple cylinders, as shown in figure 5.3. Each layer will have a contribution to the homogenized properties of the cylinder, dependent on its area ratio $A_r^{(i)}$ and thickness ratio $t_r^{(i)}$, determined with equation 5.13 and 5.14, respectively. The derivation of the nine elastic constants for each individual layer and the assembly to the homogenized elastic constants of the cylinder is given in appendix A.3.

$$A_r^{(i)} = \frac{c_{i+1}^2 - c_i^2}{1 - c^2} \tag{5.13}$$

$$t_r^{(i)} = \frac{c_{i+1} - c_i}{1 - c} \tag{5.14}$$

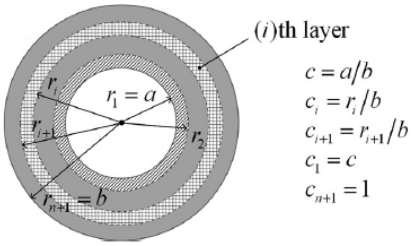

Figure 5.3: Position of laminate layers [58]

Each layer has its own elastic properties $a_{ij}^{(i)}$ which are written in the compliance matrix $[\boldsymbol{S_L}^{(i)}]$ in the cylindrical coordinate system. This compliance matrix is determined from the transformation of the compliance matrix of an unidirectional ply $[\boldsymbol{S}^{(i)}]$, as given in equation 5.15 [59]. The compliance matrix for an individual unidirectional ply and the transformation matrices $[\boldsymbol{P}]$ and $[\boldsymbol{T}]$ are given in Appendix A.2.

$$[\boldsymbol{S_L}^{(i)}] = \begin{bmatrix} a_{11}^{(i)} & a_{12}^{(i)} & a_{13}^{(i)} & a_{14}^{(i)} & 0 & 0 \\ a_{12}^{(i)} & a_{22}^{(i)} & a_{23}^{(i)} & a_{24}^{(i)} & 0 & 0 \\ a_{13}^{(i)} & a_{23}^{(i)} & a_{33}^{(i)} & a_{34}^{(i)} & 0 & 0 \\ a_{14}^{(i)} & a_{24}^{(i)} & a_{34}^{(i)} & a_{44}^{(i)} & 0 & 0 \\ 0 & 0 & 0 & 0 & a_{55}^{(i)} & a_{56}^{(i)} \\ 0 & 0 & 0 & 0 & a_{56}^{(i)} & a_{66}^{(i)} \end{bmatrix} = [\boldsymbol{P}]\left([\boldsymbol{T}]^T[\boldsymbol{S}^{(i)}][\boldsymbol{T}]\right)[\boldsymbol{P}] \tag{5.15}$$

The developed model for the determination of the elastic constants of the composite tower is verified in appendix A.3 using an example described in [58]. After the determination of the stress in the homogenized cylinder using equations 5.10 and 5.11, the stress resultants in each individual layer are obtained using equation 5.16. The terms $\Phi_{ij}^{(i)}$ are provided by equation 5.17. Here are the terms a_{ij} the terms of the compliance matrix of the homogenized cylinder $[\boldsymbol{S_h}]$ and the terms $a_{ij}^{(i)}$ are the compliance terms of the individual layers $[\boldsymbol{S_L}]$.

$$\boldsymbol{\sigma}^{(i)} = \boldsymbol{\Phi}^{(i)}\boldsymbol{\sigma} = \begin{bmatrix} 1 & 0 & 0 & 0 & 0 & 0 \\ \Phi_{21}^{(i)} & \Phi_{22}^{(i)} & \Phi_{23}^{(i)} & \Phi_{24}^{(i)} & 0 & 0 \\ \Phi_{31}^{(i)} & \Phi_{32}^{(i)} & \Phi_{33}^{(i)} & \Phi_{34}^{(i)} & 0 & 0 \\ \Phi_{41}^{(i)} & \Phi_{42}^{(i)} & \Phi_{43}^{(i)} & \Phi_{44}^{(i)} & 0 & 0 \\ 0 & 0 & 0 & 0 & 1 & 0 \\ 0 & 0 & 0 & 0 & 0 & 1 \end{bmatrix} \begin{bmatrix} \sigma_r \\ \sigma_\theta \\ \sigma_z \\ \tau_{\theta z} \\ \tau_{rz} \\ \tau_{r\theta} \end{bmatrix} \tag{5.16}$$

$$\begin{bmatrix} \Phi_{21}^{(i)} & \Phi_{22}^{(i)} & \Phi_{23}^{(i)} & \Phi_{24}^{(i)} \\ \Phi_{31}^{(i)} & \Phi_{32}^{(i)} & \Phi_{33}^{(i)} & \Phi_{34}^{(i)} \\ \Phi_{41}^{(i)} & \Phi_{42}^{(i)} & \Phi_{43}^{(i)} & \Phi_{44}^{(i)} \end{bmatrix} = \begin{bmatrix} d_{22}^{(i)} & d_{23}^{(i)} & d_{24}^{(i)} \\ d_{23}^{(i)} & d_{33}^{(i)} & d_{34}^{(i)} \\ d_{24}^{(i)} & d_{34}^{(i)} & d_{44}^{(i)} \end{bmatrix} \begin{bmatrix} a_{12} - a_{12}^{(i)} & a_{22} & a_{23} & 0 \\ a_{13} - a_{13}^{(i)} & a_{23} & a_{33} & 0 \\ -a_{14}^{(i)} & 0 & 0 & a_{44} \end{bmatrix} \tag{5.17}$$

5.2.2. Failure criteria

Several failure criteria do exist for the failure analysis of composite materials. Research did not point out one single failure criteria to be most accurate, but criteria in which a distinction is made between fiber and matrix failure look promising [60]. Two of these criteria are the Hashin-Rotem theory and Pucks failure criteria, of which the latter one is used in the WMC FEM tool [27]. The Hashin-Rotem theory is more simple and requires no additional material properties [61] and will therefore be used in the parametric design tool. The criteria is given in equation 5.18. In this equation X^t and X^c are the tensile and compressive strength in fiber direction, respectively. The tensile and compressive strength in matrix direction are given by Y^t and Y^c. S is the shear strength of the composite material. The material factors for fiber failure γ_{FF} and inter-fiber γ_{IFF} failure are 2.43 and 1.69, respectively [27].

$$\begin{aligned}
&\frac{\sigma_1}{X^t} < 1 && \text{if} \quad \sigma_1 > 0 \\
&\frac{\sigma_1}{X^c} < 1 && \text{if} \quad \sigma_1 < 0 \\
&\frac{\sigma_2^2}{(Y^t)^2} + \frac{\tau_{12}^2}{S^2} < 1 && \text{if} \quad \sigma_2 > 0 \\
&\frac{\sigma_2^2}{(Y^c)^2} + \frac{\tau_{12}^2}{S^2} < 1 && \text{if} \quad \sigma_2 < 0
\end{aligned} \tag{5.18}$$

The stresses σ_1, σ_2 and τ_{12} given here are the stresses in principal material directions. The obtained layer stresses from equation 5.16 have to be transformed to this material coordinate system using equation 5.19.

$$\boldsymbol{\sigma_{12}}^{(i)} = [\boldsymbol{T}][\boldsymbol{P}]\boldsymbol{\sigma}^{(i)} \tag{5.19}$$

5.2.3. Stress analysis verification

The stress analysis method described in section 5.2.1 was written for composite risers with diameters of 0.3 meter and thickness of 5 mm. To verify the applicability of this method for composite wind turbine towers with diameters of approximately 5 meter and wall thicknesses in the range of 100 to 200 mm, a comparison will be made with the program WMC FEM, a finite element solver for thick shell elements. Two load situations (pure compressive load of 10000 kN and bending load of 300 MNm) are compared for a composite tube of 100 and 200 mm thickness. The material properties and tower geometry are given in table 5.2.

Table 5.2: Material properties and tower geometry

E_1 [GPa]	32.85
E_2 [GPa]	10.4
G_{12} [GPa]	2.595
ν_{12} [-]	0.2735
Laminate layup [deg]	$[0, 45, -45, 90]_s$
Thickness fraction [%]	$[30, 7.5, 7.5, 5]_s$
Mean diameter [m]	5.0
Thickness [mm]	100, 200

In figure 5.4 the stresses in each individual layer in their respective material coordinate system of the included method and the FEM results are shown. In the FEM solver, each layer is analyzed on the bottom, center and top. The model solves the stress resultants only on the top of each layer. Only in-plane resultant stresses are shown, whereas out-of-plane stresses are negligible small and can therefore be neglected. Maximum difference between the FEM solver and the included method are within 0.2% and therefore it is concluded that compressive force stress resultants are accurately determined.

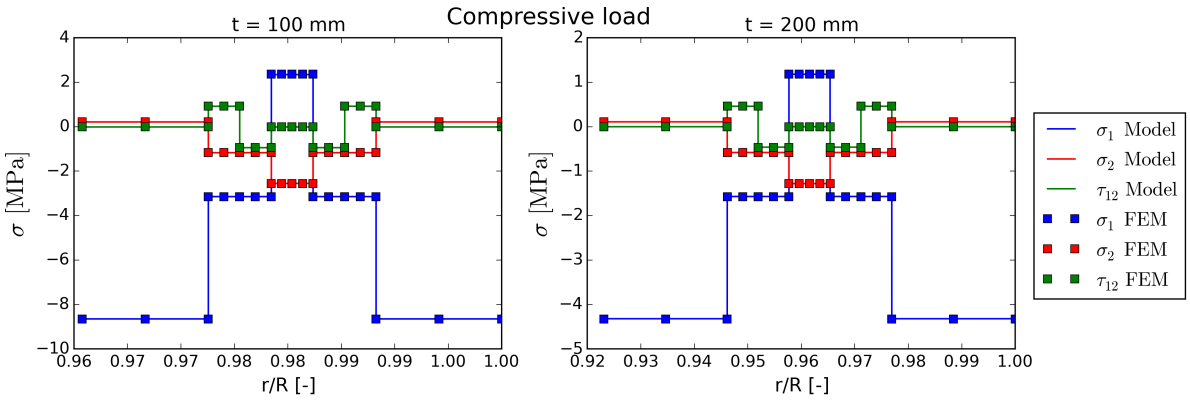

Figure 5.4: Compressive load of 1000 kN

In figure 5.5 the results for a a bending moment of 300 MNm are shown. Again, only in-plane resultant stresses are shown, whereas out-of-plane stresses can be neglected. Although differences between the FEM model and the included method are now larger (maximum of 0.9%), it is concluded that bending stress resultants are calculated accurately for towers with these dimensions. The increased thickness does not influence the accuracy.

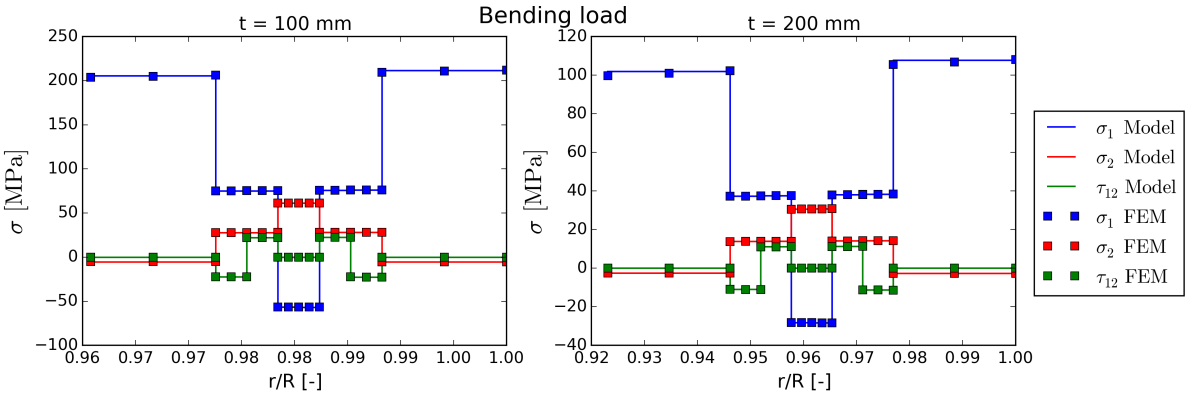

Figure 5.5: Bending load of of 300 MNm

5.2.4. Buckling analysis

The composite tower will be loaded in bending and compression. However, to the knowledge of the author only approximate expressions for a pure compression load do exist. As mentioned in [62], the maximum critical bending stress is more or less the same as the critical buckling stress due to an axial compression load. Therefore, a simplified method analyzing the composite tower as cylindrical shells under uniform axial compression is expected to be legitimate. Use is made of approximate solution for the critical axial compressive load described by [63]. The solution is based on shallow shell theory using the the Kirchhoff-Love-type assumption. Simply supported boundary conditions are used, which is a conservative choice. The following assumptions using shallow shell theory and the Kirchhoff-Love assumption do hold [64]:

- The shell is thin, implying that the thickness is much smaller than the other dimensions.
- Straight lines perpendicular to the mid-plane remain perpendicular after deformation.
- No transverse shear flexibility.
- The transverse normal stress σ_r is small compared to σ_z and σ_θ.
- The laminate is considered orthotropic (D_{13}, D_{23}, D_{31}, D_{32}, B_{13}, B_{23}, B_{31} and B_{32} are zero).

The critical buckling load N_0 as determined with equation 5.20 is the minimum that can be found for any combination of axial halfwaves m (equation 5.21) and circumferential waves n (equation 5.22).

$$N_0 = \frac{1}{\beta^2}\left(\tilde{D}_{11}\beta^4 + 2(\tilde{D}_{12}+2\tilde{D}_{66})\beta^2\eta^2 + \tilde{D}_{22}\eta^4 + \frac{(e_{21}\beta^4 + (e_{11}+e_{22}-2e_{33})\beta^2\eta^2 + e_{12}\eta^4 + \frac{\beta^2}{r_m})^2}{a_{22}\beta^4 + (2a_{12}+a_{33})\beta^2\eta^2 + a_{11}\eta^4}\right) \tag{5.20}$$

$$\beta = \frac{m\pi}{L} \tag{5.21}$$

$$\eta = \frac{n}{r_m} \tag{5.22}$$

For non-symmetric laminates, the bending stiffness matrix D has to be modified according to equation 5.23. Next to that, eccentricity terms e_{ij} will have an influence as well, which are determined with equation 5.24.

$$\tilde{D} = D - B^T A^{-1} B \tag{5.23}$$

$$e = A^{-1} B \tag{5.24}$$

The implementation of this buckling analysis method is verified with the example in the paper of Geier [63], for which the exact same results are obtained. However, this example consists of a cylinder with a inner radius of 250 mm, thickness of 1.25 mm and a length of 510 mm. To see if this buckling analysis method is valid for composite towers with a length of approximately 100 meter, a diameter of 5 meter and thickness between 100 and 200 mm, a comparison will be made with the buckling analysis tool Finstrip in section 5.2.5.

5.2.5. Finstrip buckling comparison

To see if the analytical method is accurate enough for a tube with the dimensions of a tower and to identify the differences between the implemented analytical solution for axial compression and the bending load situation of the tower, a comparison will be made with the program Finstrip. In Finstrip, the cross-section is divided in a finite number of strips to predict the initial buckling of prismatic beams for a given applied compression and bending load [65]. The same tower configuration as described in table 5.2 will be used, with a tower length of 100 m. The diameter to thickness ratio (D/t ratio) is varied between 25 and 150. In Finstrip, engineering bending theory is used to calculate the critical buckling stress [65]. It must be mentioned that this is not the actual stress in the layers but the stress for an isotropic material. To make a comparison with the axial and bending load, the critical stress is compared. The results are shown in figure 5.6.

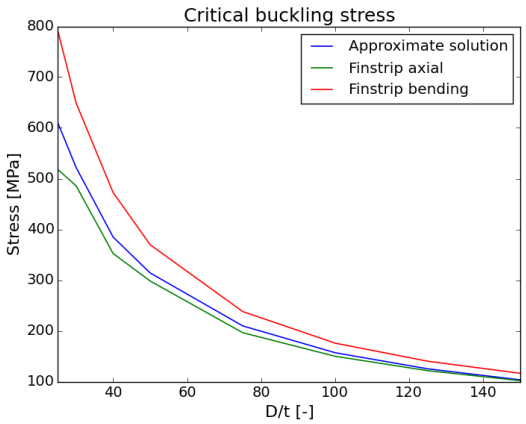

Figure 5.6: Critical buckling stress

As can been seen, the critical stress found with Finstrip due to a bending load is higher than for a pure axial compression load. This can be explained by looking at the buckling modes. The critical buckling modes for an axial compression and bending load for a D/t ratio of 40 are shown in figures 5.7 and 5.8, respectively. The buckling modes are different for these two load situations due to the fact that in a bending situation one side of the tube is loaded in tension and therefore not prone for buckling.

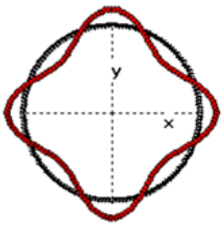

Figure 5.7: Axial compression buckling mode for D/t = 40

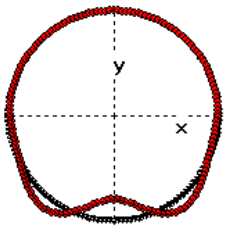

Figure 5.8: Bending compression buckling mode for D/t =40

Comparing the approximate solution of Geier with the results of Finstrip, it can be seen that the approximate solution underestimates the critical stress for a pure compression load. This underestimation grows bigger for smaller D/t, with a maximum difference of 17% for a D/t of 25. However, as found in chapter 4, the bending moment is much larger than the compressive load and will have a bigger contribution to the buckling load. For a D/t ratio of 150, the critical buckling stress for a bending load found with Finstrip is 12% higher than the critical buckling stress for a pure compression load found with the approximate method. For a D/t

ratio of 25, this difference grows to 30%. Therefore, the expression of Geier implemented in the parametric model can be considered to be conservative for the buckling analysis of the composite tower and will result in a conservative design. If the buckling criteria is found to be design driving, it is recommended to use a more accurate method such as FEM to analyze the buckling load.

According to the design standard for wind turbine blades [35], analytical expressions for buckling analysis can be used if an extra reduction factor of 1.5 is applied. Taking into account the other reduction factors due to criticality of failure mode (1.08), long-term degradation (1.05), temperature effects (1.05), material and production tolerances (1.1) and accuracy of load assumptions (1.2), the total reduction factor for the stability analysis of the tower will then becomes 2.36.

5.3. Global buckling

Next to local buckling, the support structure might buckle as a whole due to the axial load on the top (the mass of the RNA), known as global buckling. The critical global buckling load can be calculated with the Euler buckling formula (equation 5.25).

$$P_{cr} = \frac{C\pi^2 EI_{av}}{L^2} \tag{5.25}$$

The factor C depends on the boundary conditions of the column, whereas a support structure can be considered one end free; one end fixed, as shown in figure 5.9. Since the support structure consists of a steel and composite part, the bending stiffness EI will be different. Therefore, a weighted average, dependent on length, will be used, as given in equation 5.26. The material factor for global buckling is 1.2 [32].

$$EI_{av} = \frac{EI_{mp+tp}L_{mp+tp} + EI_{tower}L_{tower}}{L} \tag{5.26}$$

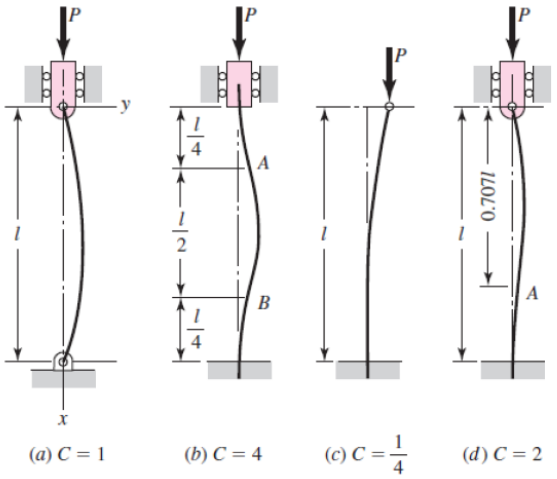

Figure 5.9: Global buckling for a) both ends simply supported b) both ends fixed c) one end free; one end fixed d) one end simply supported, one end fixed [11]

6

Optimization Module

In this chapter the optimization strategy and algorithm included in the parametric model will be explained. This optimization algorithm will then be used to perform a sensitivity a sensitivity analysis on the load estimation model, DAF and natural frequency estimation.

6.1. Optimization algorithm

The optimization algorithm used is a GA. This optimization algorithm is based on the natural selection process of Darwinian evolution theory, in which a population (a predefined number of support structure solutions) evolves into an optimal support structure through selection and generation of better solutions [4]. The structure of this optimization algorithm is shown in figure 6.1. The different steps will be explained in more detail.

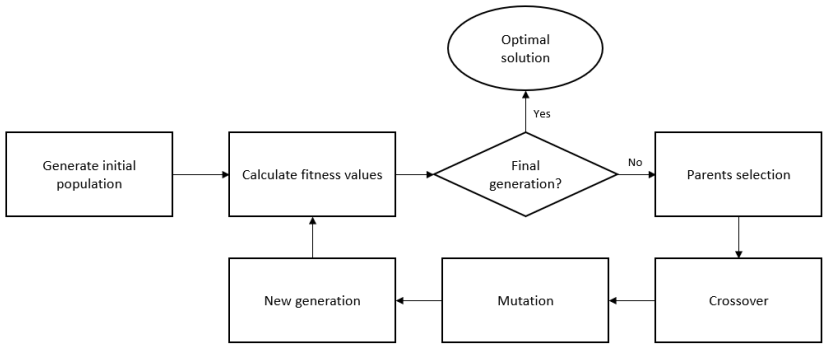

Figure 6.1: Genetic algorithm

Generate initial population

The algorithm starts by creating an initial population with a predefined number of solutions by choosing random initial values for the optimization variables within the given design space. The number of solutions in the initial population should be at least ten times the number of optimization variables, such that solutions across the complete design space are present [4]. However, to increase the possibility of finding a global optimum, this number is increased to 150 in this study. These assigned values of each optimization variable for each solution are called genes.

The optimization variables used in the algorithm are shown in figure 6.2. The number of optimization variables is kept small such that the optimization will run for 8 hours as maximum. For the monopile, the optimization variables are the bottom diameter D_0, bottom thickness $t_{mp,0}$ and top thickness $t_{mp,1}$. The bottom and top three meters are cylindrical due to installation requirements [13], while the remaining part is conical with an angle δ_{mp}. The transition piece has a constant thickness t_{tp} and constant cone angle δ_{tp} over its

entire length. The diameter of the tower is set by the bottom diameter and two cone angles of the monopile and transition piece, and remains constant along its length because of production constraints. The tower is optimized by varying the thickness at the bottom $t_{tw,0}$, middle $t_{tw,1}$ and top $t_{tw,2}$. The thickness variables of the monopile top, tower middle and tower top are related to the bottom thickness of the monopile and tower, as it is assumed that these thicknesses will not be bigger than the bottom thicknesses. Next to that, it is assumed that the thickness of the transition piece will be smaller or equal to the monopile top thickness. The thickness of the sections in between these thickness variables are calculated by linear interpolation.

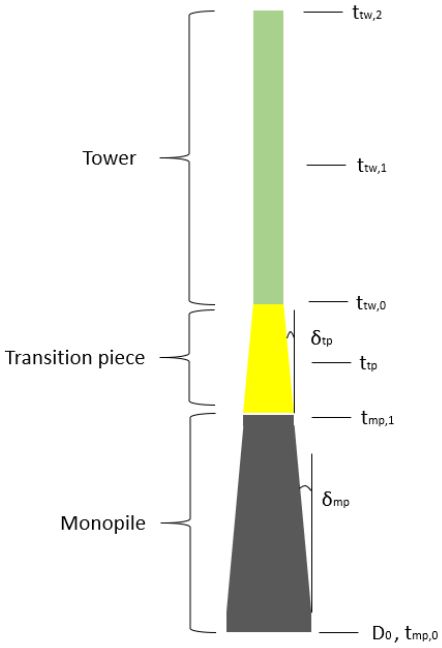

Figure 6.2: Optimization variables

Fitness calculation

For all these solutions in the population, it will be checked how well it performs with respect to the objective function (minimal mass of the support structure). This is called the fitness value. The function for the fitness value is based on the fitness function described in [66]. The feasibility of all these solutions will be checked by analyzing the constraint functions (natural frequency, yield and buckling constraints). If all constraints are met, the fitness value of the solution equals the mass of the support structure. If one or multiple of these constraints are not met, a penalty value will be assigned. The fitness value of the solution F_{M_s} in this situation equals the sum of all penalties times the mass of the support structure (equation 6.1).

$$F_{M_s} = M_s \cdot (1 + p_f + p_{yield} + p_{Hashin,t} + p_{Hashin,c} + p_{buck} + p_{gb}) \tag{6.1}$$

The first feasibility criteria to be checked is the natural frequency constraint. As already mentioned in chapter 2 the optimal tower design will have its natural frequency below the 1P area. This region is prone to wave frequencies and therefore this frequency range has to be considered as well. The frequency of the support structure has to be at least 10% lower as the lowest of these two excitation frequencies [10]. The frequency penalty function p_f is given by equation 6.2.

$$p_f = \begin{cases} 0.0 & \text{if} \quad \frac{f_{nat}}{0.9\left(\min\left(f_{1P}, \frac{1}{T_{pmax}}\right)\right)} < 1.0 \\ \frac{f_{nat}}{0.9\left(\min\left(f_{1P}, \frac{1}{T_{pmax}}\right)\right)} - 1.0 & \text{if} \quad \frac{f_{nat}}{0.9\left(\min\left(f_{1P}, \frac{1}{T_{pmax}}\right)\right)} \geq 1.0 \end{cases} \tag{6.2}$$

The penalty function for the yield stress constraint for the monopile and transition piece will be analyzed along a predefined number of cross sections. The yield stress penalty function on cross section i $p_{yield,i}$,

based on 5.1 is given by equation 6.3. The penalty values which value are higher then zero will be stored in a vector. The sum of this vector equals the penalty function for the yield stress constraint p_{yield} (6.4).

$$p_{yield,i} = \begin{cases} 0.0 & \text{if} \quad \frac{\sigma_{max} \cdot \gamma_M}{\sigma_{yield}} < 1.0 \\ \frac{\sigma_{max} \cdot \gamma_M}{\sigma_{yield}} - 1.0 & \text{if} \quad \frac{\sigma_{max} \cdot \gamma_M}{\sigma_{yield}} \geq 1.0 \end{cases} \tag{6.3}$$

$$p_{yield} = \text{sum}\left[p_{yield,1}, p_{yield,2} \quad \cdots \quad p_{yield,n} \right] \tag{6.4}$$

Since GFRP has different strength properties in tension and compression, both sides of the tower will be analyzed for material failure. If a ply is loaded in tension, a penalty function $p_{Hashin,t,i}$ is assessed according to equation 6.5. If a ply is loaded in compression, a penalty function $p_{Hashin,c,i}$ according to equation 6.7 will be applied. Again, the penalty values will be stored in a vector, of which the sum equals the penalty value for the failure criteria $p_{Hashin,t}$ (equation 6.6) and $p_{Hashin,c}$ (equation 6.8).

$$p_{Hashin,t,i} = \begin{cases} 0.0 & \text{if} \quad \frac{\gamma_{FF} \cdot \sigma_1}{X^t} < 1.0 \\ 0.0 & \text{if} \quad \gamma_{IFF}\left(\frac{\sigma_2^2}{(Y^t)^2} + \frac{\tau_{12}^2}{S^2} \right) < 1.0 \\ \frac{\gamma_{FF} \cdot \sigma_1}{X^t} - 1.0 & \text{if} \quad \frac{\gamma_{FF} \cdot \sigma_1}{X^t} \geq 1.0 \\ \gamma_{IFF}\left(\frac{\sigma_2^2}{(Y^t)^2} + \frac{\tau_{12}^2}{S^2} \right) - 1.0 & \text{if} \quad \gamma_{IFF}\left(\frac{\sigma_2^2}{(Y^t)^2} + \frac{\tau_{12}^2}{S^2} \right) \geq 1.0 \end{cases} \tag{6.5}$$

$$p_{Hashin,t} = \text{sum}\left[p_{Hashin,t,1}, p_{Hashin,t,2} \quad \cdots \quad p_{Hashin,t,n} \right] \tag{6.6}$$

$$p_{Hashin,c,i} = \begin{cases} 0.0 & \text{if} \quad \frac{\gamma_{FF} \cdot \sigma_1}{X^c} < 1.0 \\ 0.0 & \text{if} \quad \gamma_{IFF}\left(\frac{\sigma_2^2}{(Y^c)^2} + \frac{\tau_{12}^2}{S^2} \right) < 1.0 \\ \frac{\gamma_{FF} \cdot \sigma_1}{X^c} - 1.0 & \text{if} \quad \frac{\gamma_{FF} \cdot \sigma_1}{X^t} \geq 1.0 \\ \gamma_{IFF}\left(\frac{\sigma_2^2}{(Y^c)^2} + \frac{\tau_{12}^2}{S^2} \right) - 1.0 & \text{if} \quad \gamma_{IFF}\left(\frac{\sigma_2^2}{(Y^c)^2} + \frac{\tau_{12}^2}{S^2} \right) \geq 1.0 \end{cases} \tag{6.7}$$

$$p_{Hashin,c} = \text{sum}\left[p_{Hashin,c,1}, p_{Hashin,c,2} \quad \cdots \quad p_{Hashin,c,n} \right] \tag{6.8}$$

In equation 6.9, the penalty function for local buckling p_{buck_i} on cross section i is shown. Just as for the yield and material failure, the values with a value higher then zero will be stored in a vector. The sum of this vector will equal the penalty function for the local buckling constraint p_{buck} (equation 6.10) Note that the determination of critical buckling stress and material factor are different for the steel and composite part, as discussed in chapter 5.

$$p_{buck_i} = \begin{cases} 0.0 & \text{if} \quad \frac{\sigma_{max} \cdot \gamma_M}{\sigma_{cr}} < 1.0 \\ \frac{\sigma_{max} \cdot \gamma_M}{\sigma_{cr}} - 1.0 & \text{if} \quad \frac{\sigma_{max} \cdot \gamma_M}{\sigma_{cr}} \geq 1.0 \end{cases} \tag{6.9}$$

$$p_{buck} = \text{sum}\left[p_{buck_1}, p_{buck_2}, \quad \cdots \quad p_{buck_n} \right] \tag{6.10}$$

The global buckling constraint is analyzed with equation 6.11. A penalty function p_{gb} will be assigned if the constraint is not met.

$$p_{gb} = \begin{cases} 0.0 & \text{if} \quad \frac{N \cdot \gamma_M}{P_{cr}} < 1.0 \\ \frac{N \cdot \gamma_M}{P_{cr}} - 1.0 & \text{if} \quad \frac{N \cdot \gamma_M}{P_{cr}} \geq 1.0 \end{cases} \tag{6.11}$$

Parents selection, crossover and mutation

By a selection operator, a number of solutions will be chosen to be parents to make a new generation. This number of solutions to be selected depends on the crossover probability, which is often set at 0.9 [4]. This means that the best 90% of the population will be selected as parents. The 10% best solutions of the population will go to the next generation without modification. The remaining part of the next generation is constructed by crossover and mutation [1] of the 90% best solutions of the generation. In crossover, two parents are selected to make children. A single-point crossover [67] is used, in which a randomly chosen point

divides the genes of one of the parents in two strings. One child is formed by taking the genes on the left hand side of this point of parent 1 and the genes on the right hand side of this point of parent 2. The two parents to form a child are chosen randomly from the selection.

After the crossover operation, the mutation operator may change one or more of the optimization variables of a child randomly (within the design boundaries). This is done such that diversity is maintained within the population [67]. The chance this mutation will take place depends on the mutation probability, which is often set at 0.01 [4].

6.2. Optimization study

In this section, the optimization algorithm will be used to identify the design constraints of the support structure and to identify the limitations of the load estimation model. First, an optimization will be performed using the load estimations of the parametric design model in section 6.2.1. In section 6.2.2 the effect of tower top bending moment on the optimization is analysed, and in section 6.2.3 and 6.2.4 the sensitivity on damping ratio and frequency will be analysed. For this case study, the load cases for the offshore site of Borssele III as described in section 4.4.4 will be used. The length of the monopile is assumed to go to water level (35.1 meter), while the transition piece and tower length have assumed values of 17.6 and 106.5 meter, respectively. For the soil stiffness, the same soil conditions as used in section 3.3.3 will be used. The monopile is considered to be slender. For the monopile and transition piece, S355 steel is used. For the composite tower the material properties are given in table 6.1. These material properties were acquired with material coupon tests at LM Wind Power. As mentioned previously, the number of optimization variables is restricted to reduce computational time, and therefore a fixed laminate layup $[0,45,\text{-}45,90]_s$ with thickness fraction $[30, 7.5, 7.5, 5]_s$ is used.

Table 6.1: Material properties

ρ [kg/m^3]	E_1 [GPa]	E_2 [GPa]	G_{12} [GPa]	ν_{12} [-]	X^t [MPa]	X^c [MPa]	Y^t [MPa]	Y^c [MPa]	S [MPa]
1614.0[1]	32.85	10.40	2.595	0.2735	754.0	484.8	62.5	150	38.8

The design boundaries for the previous described optimization variables are shown in table 6.2. The lowest and highest support structure mass possible within this design space is 187.2 tonnes and 2183.7 tonnes, respectively. These design boundaries are a first guess. If solutions tend to be found with variables on the limits of the design space given, it is likely that the optimum is found outside this range, hence the design space should be changed. Three optimization runs are performed with this initial design space, after which the design space is altered for a fourth optimization run.

Table 6.2: Design space 1

Design variable	Design boundaries
D_0 [m]	5.0 - 8.0
$t_{\text{mp},0}$ [mm]	50 - 120
$t_{\text{mp},1}$ [mm]	(0.5 - 1.0)$\cdot t_{\text{mp},0}$
t_{tp} [mm]	(0.5 - 1.0)$\cdot t_{\text{mp},1}$
$t_{\text{tw},0}$ [mm]	50 - 200
$t_{\text{tw},1}$ [mm]	(0.3 - 1.0)$\cdot t_{\text{tw},0}$
$t_{\text{tw},2}$ [mm]	(0.3 - 1.0)$\cdot t_{\text{tw},1}$
δ_{mp} [deg]	0.0 - 1.6
δ_{tp} [deg]	0.0 - 1.6

[1] Due to a misreading, 1614 kg/m^3 was used instead of 1850 kg/m^3 The results were analyzed with this higher density as well, resulting in a slightly higher tower mass. The solutions still remain feasible.

6.2.1. General optimization

This optimization run uses the load calculations as they are calculated in the parametric design model. First, three optimization runs are performed using the design space given in table6.2, each analyzing 25 generations of 150 solutions. The results of the three initial optimization runs are shown in 6.3. Each solution is different, whereas the largest difference between the optimization results are the bottom diameters and cone angles of the monopile and transition piece. The difference between the total mass of the best run (A1.1) and worst run (A1.3) is less than 1%, and therefore it is expected that these solutions have to be close to the optimal solution.

Table 6.3: Optimization results

	Design space 1			Design space 2a
	Run A1.1	**Run A1.2**	**Run A1.3**	**Run A2.1**
Total mass [tonnes]	728.1	729.8	730.8	706.1
Mp mass [tonnes]	374.4	385.5	377.9	366.6
Tp mass [tonnes]	139.3	132.6	142.4	133.5
Tower mass [tonnes]	214.4	211.7	210.5	206.0
Frequency [Hz]	0.0535	0.0593	0.0502	0.0551
D_0 [m]	5.64	5.62	5.05	5.39
$t_{mp,0}$ [mm]	87	93	96	88
$t_{mp,1}$ [mm]	81	71	83	74
t_{tp} [mm]	69	60	71	62
$t_{tw,0}$ [mm]	148	139	154	138
$t_{tw,1}$ [mm]	92	83	86	81
$t_{tw,2}$ [mm]	32	31	39	35
δ_{mp} [deg]	1.20	0.63	0.57	0.54
δ_{tp} [deg]	0.39	0.77	0.59	0.72

In figures 6.3 and 6.4 the inner diameter and thickness distribution of the three optimized designs are shown, respectively. The yield and buckling constraint violation along the support structure length are shown in figures 6.5 and 6.6. These values should be below one, whereas an optimum is as close to one as possible. The monopile and transition piece are design driven by the buckling constraint. The bottom of the tower is limited by the yield constrained, while the upper part is more sensitive for buckling.

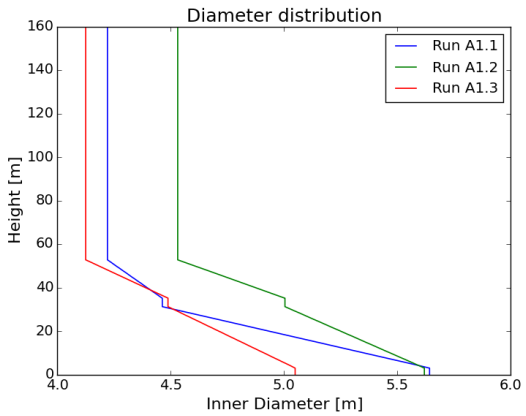

Figure 6.3: Inner diameter distribution of optimization runs

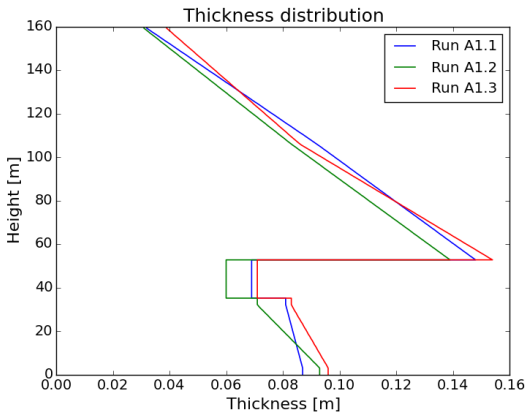

Figure 6.4: Thickness distribution of optimization runs

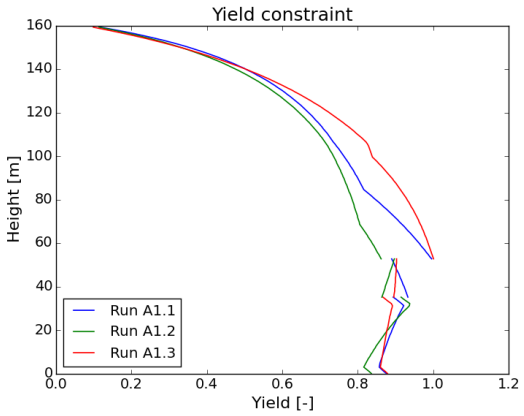

Figure 6.5: Yield constraint of optimization runs

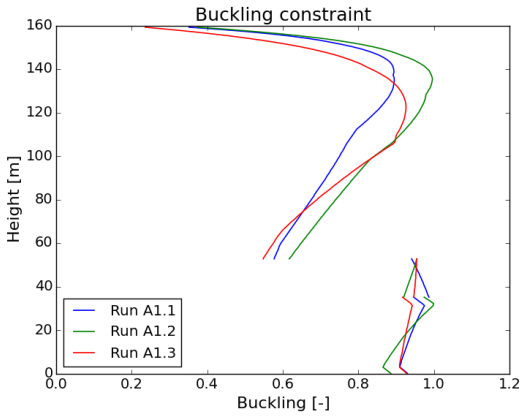

Figure 6.6: Buckling constraint of optimization runs

The fourth optimization run A2.1 is performed using the concentrated design space 2a given in table 6.4. The result of this optimization run is added to table 6.3. For this optimization run, the support structure mass is reduced with 3% compared to optimization run A1.1.

Table 6.4: Design space 2a

Design variable	**Design boundaries**
D_0 [m]	5.0 - 6.0
$t_{\mathrm{mp},0}$ [mm]	70 - 100
$t_{\mathrm{mp},1}$ [mm]	(0.5 - 1.0)$\cdot t_{\mathrm{mp},0}$
t_{tp} [mm]	(0.5 - 1.0)$\cdot t_{\mathrm{mp},1}$
$t_{\mathrm{tw},0}$ [mm]	120 - 160
$t_{\mathrm{tw},1}$ [mm]	(0.3 - 1.0)$\cdot t_{\mathrm{tw},0}$
$t_{\mathrm{tw},2}$ [mm]	(0.3 - 1.0)$\cdot t_{\mathrm{tw},1}$
δ_{mp} [deg]	0.0 - 1.6
δ_{tp} [deg]	0.0 - 1.6

In figure 6.7 a contour plot of the mass of optimization run A2.1 is shown, in which all optimization variables are constrained except for the transition piece cone angle and tower bottom thickness. The mass of the support structure can be reduced by increasing the transition piece cone angle or reducing the tower bottom thickness. These two variables are varied manually to find an indicative border for which no feasible solutions can be found anymore. If the transition piece cone angle is increased above 0.75 degrees, the transition piece and tower will violate the buckling and yield constraint, respectively. If the transition piece cone angle is decreased, the tower bottom thickness can be reduced. However, this decrease in thickness is restricted by the tower yield constraint, such that no feasible solutions with a lower mass with respect to the solution of A2.1 can be obtained. From this it is concluded that for these two parameters and the other parameters fixed an optimal solution has been found.

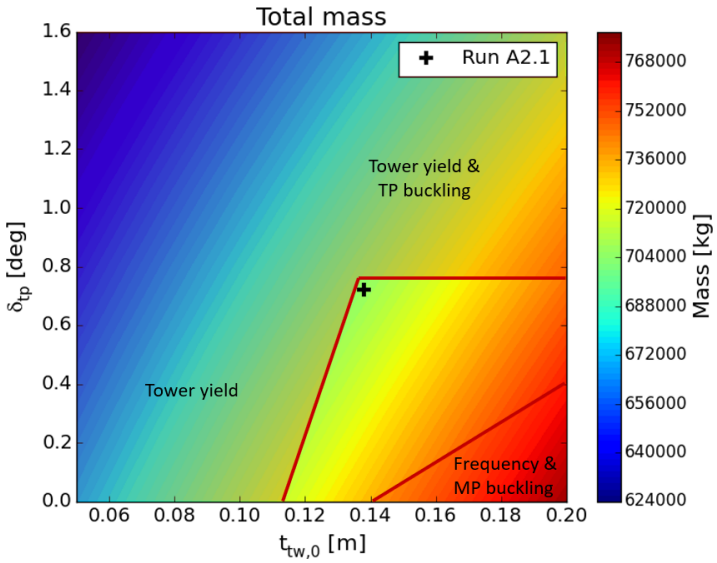

Figure 6.7: Mass contour plot for optimization run A2.1

In figure 6.8 a contour plot of run A2.1 for the optimization variables D_0 en δ_{mp} is shown, together with the optimum found in optimization run A2.1. As can been seen, these two optimization variables will have an influence on the design constraints of the complete support structure. An increase in cone angle will violate the monopile, transition piece and tower yield and buckling constraints. Without changing the other design variables, the optimal solution would have been found at point A, with a cone angle of approximately 0.4 degree and a bottom diameter of 5.25 meter. The mass of this solution is 700.7 tonnes, which is a reduction of only 0.1% compared to solution A2.a and therefore negligible.

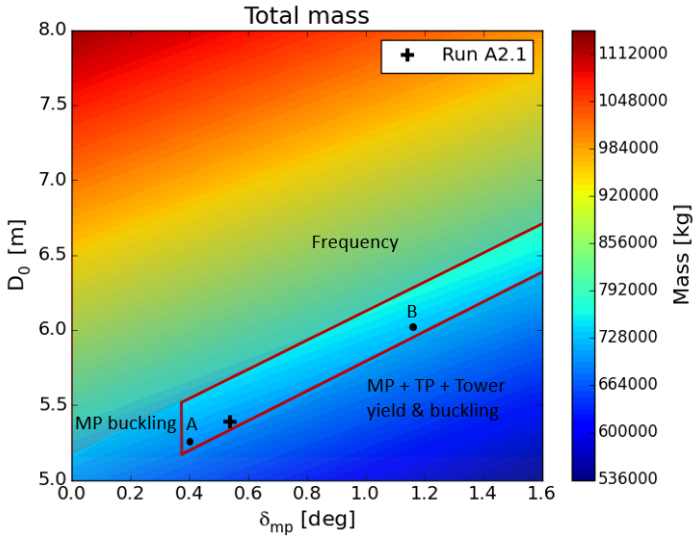

Figure 6.8: Mass contour plot for optimization run A2.1

As said before, the remaining variables are not changed in these contour plots. However, for solution at point B in figure 6.8, with a bottom diameter of 6.0 meter and cone angle of 1.2 degrees, the thicknesses can be changed without violating the constraints. Due to the increased bottom diameter, the bottom monopile thickness can be reduced to 78 mm. Due to the increased cone angle, the tower bottom and middle thickness have to be increased by 1 mm each. This solution will have a mass of 700 tonnes, a reduction of only 1% compared to run A2.1. From this it is concluded that multiple solutions can be found with approximately the same mass.

6.2.2. Top bending moment effect

As found in chapter 4, the maximum tower top bending moment of each load case is missing in the load estimation model, leading to an underestimation of the maximum bending moment. To identify the effect of this top bending moment on the mass, the optimization has been performed including the top bending moments of the three load cases of Tower 2 as found in chapter 4, which were the average values found of the three tower concepts. It must be mentioned here that this bending moment is multiplied by the load factor of 1.35 as well. Again, initially three optimization runs are performed for which the results are given in table 6.5. The difference between the best (B1.1) and worst (B1.2) solution is 7%.

Table 6.5: Optimization results with tower top bending moment

	Design space 1			Design space 2b
	Run B1.1	**Run B1.2**	**Run B1.3**	**Run B2.1**
Total mass [tonnes]	965.2	896.6	915.1	848.6
Mp mass [tonnes]	478.1	443.2	453.2	415.7
Tp mass [tonnes]	197.4	167.9	167.1	169.4
Tower mass [tonnes]	289.7	285.5	294.8	263.5
Frequency [Hz]	0.0701	0.0646	0.0639	0.0604
D_0 [m]	5.68	5.54	5.51	5.63
$t_{mp,0}$ [mm]	113	107	114	97
$t_{mp,1}$ [mm]	97	86	80	91
t_{tp} [mm]	94	80	78	85
$t_{tw,0}$ [mm]	179	172	183	179
$t_{tw,1}$ [mm]	110	124	106	105
$t_{tw,2}$ [mm]	69	65	104	62
δ_{mp} [deg]	1.13	0.74	0.52	1.28
δ_{tp} [deg]	0.25	1.01	1.30	0.34

The natural frequencies of these initial three solutions are closer to the wave excitation frequencies of DLC 1.6 at cut-out (0.0794 Hz) and DLC 6.1 (0.0834 Hz) than the optimization solutions of run A, which induces a higher loading on the submerged part of the structure. The loading on the submerged part of the support structure of Runs A and Run B are shown in figures 6.9 and 6.10, respectively. As can been, the difference between monopile loading for the obtained solutions is larger for runs B. Due to the increased sensitivity on the DAF for support structures with a natural frequency closer to the excitation frequencies of the waves, the optimization algorithm has more difficulty finding a (near-) optimal solution.

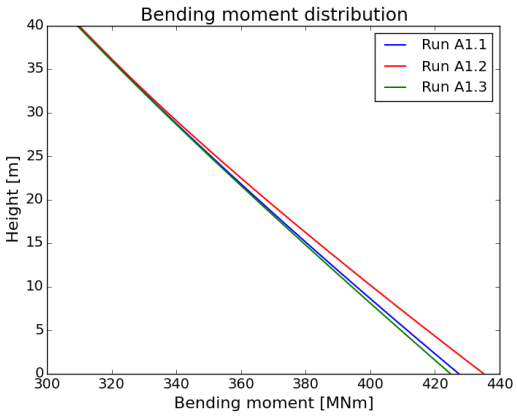

Figure 6.9: Loading on submerged part of Runs A1.1 - A1.3

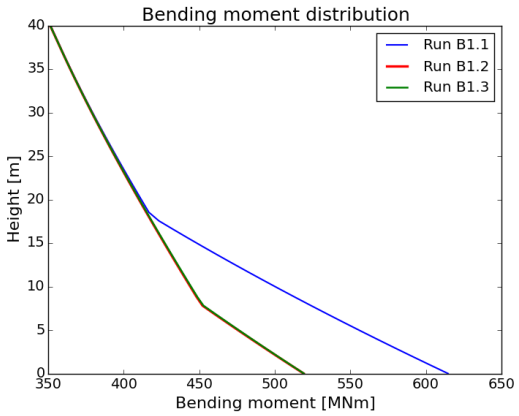

Figure 6.10: Loading on submerged part of Runs B1.1 - B1.3

For the fourth optimization run, the design space is concentrated to design space 2b as given in table 6.6.

Since larger variation in mass of the initial three runs is present than for runs A, the number of generations is increased to 35. The result is added to table 6.5. An additional mass reduction of 5% is achieved compared to run B1.2.

Table 6.6: Design space 2b

Design variable	Design boundaries
D_0 [m]	5.0 - 6.5
$t_{\text{mp},0}$ [mm]	70 - 120
$t_{\text{mp},1}$ [mm]	(0.5 - 1.0)$\cdot t_{\text{mp},0}$
t_{tp} [mm]	(0.5 - 1.0)$\cdot t_{\text{mp},1}$
$t_{\text{tw},0}$ [mm]	120 - 200
$t_{\text{tw},1}$ [mm]	(0.3 - 1.0)$\cdot t_{\text{tw},0}$
$t_{\text{tw},2}$ [mm]	(0.3 - 1.0)$\cdot t_{\text{tw},1}$
δ_{mp} [deg]	0.0 - 1.6
δ_{tp} [deg]	0.0 - 1.6

The solution of run B2.1 is compared with the solution of run A2.1 to identify the effect of the tower top bending moment. As can been seen in figures 6.13 and 6.14, the increased loading (shown in figures 6.11 and 6.12) is mainly captured by an increase in thickness. In figure 6.15 and 6.16 can be seen that the design driving constraints along the structure do not change by including the tower top bending moment.

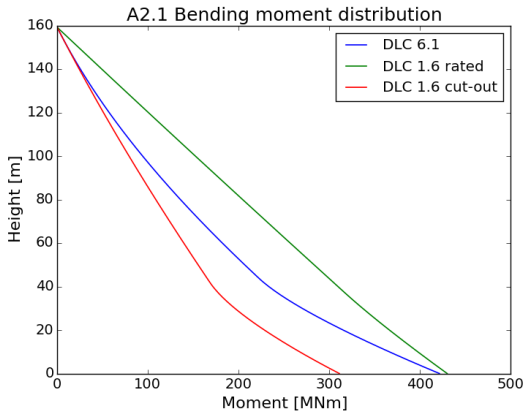

Figure 6.11: Bending moment distribution of Run A2.1

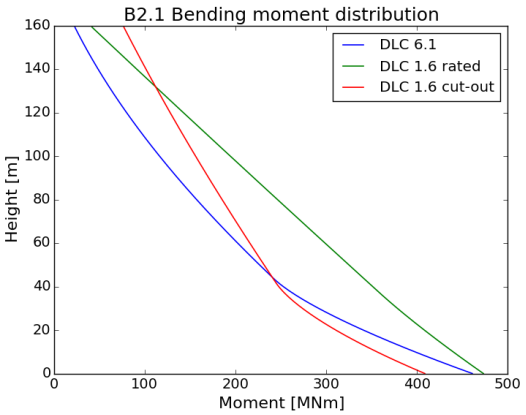

Figure 6.12: Bending moment distribution of Run B2.1

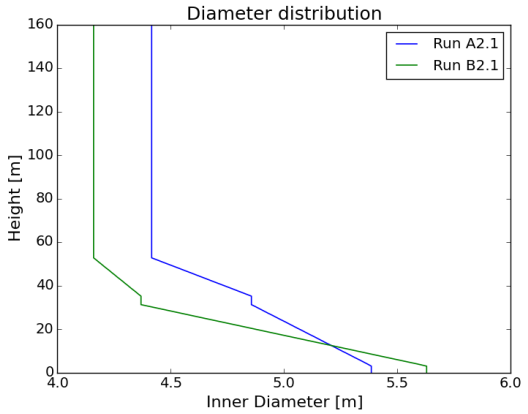

Figure 6.13: Inner diameter distribution

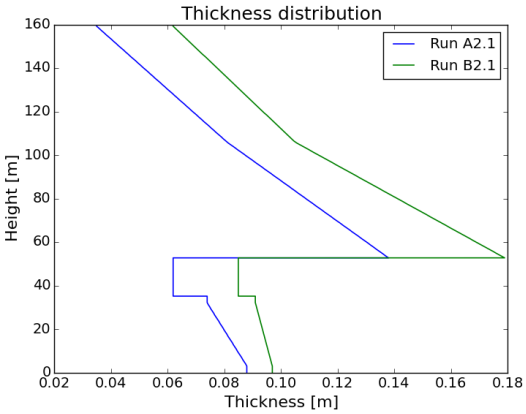

Figure 6.14: Thickness distribution

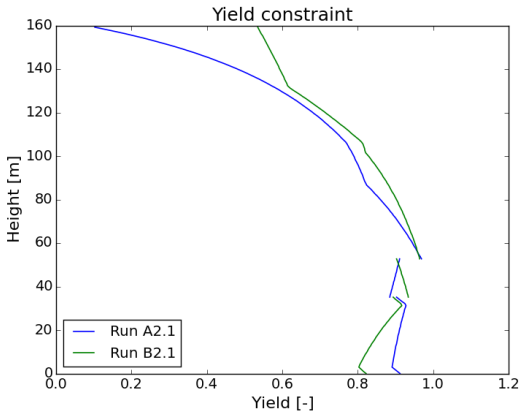

Figure 6.15: Yield constraint

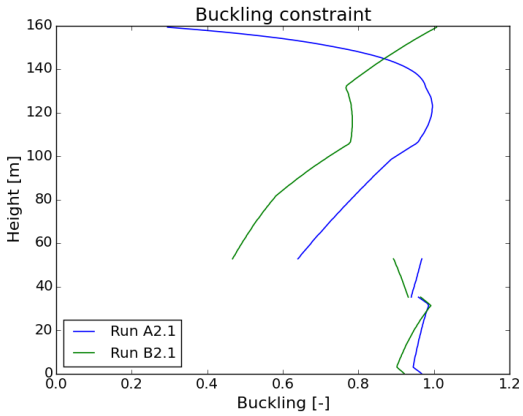

Figure 6.16: Buckling constraint

The solution of run B2.1 has an increased monopile mass of 13%, transition piece mass of 27% and tower mass of 27& compared to run A2.1. Therefore it can be concluded that the tower top bending moment has significant effect on the mass of the support structure and should not be ignored in the determination of maximum bending distribution.

6.2.3. Sensitivity on damping ratio

As found in section 4.4.5, the slope of the bending moment on the submerged part of the structure of the production load cases for the flexible Towers 2 and 3 is overestimated compared to the Focus6 results. As found in appendix D.2, the value of 5% damping ratio is on the conservative side and might be increased to 10% for production load cases. Therefore, new optimization runs have been performed with a damping ratio of 10% for the two production load cases. The damping ratio of 2% for load case DLC 6.1 is not changed. The results for the initial three runs using design space 1 and the fourth run using design space 2b are shown in table 6.7.

Table 6.7: Optimization results for DAF of 10%

	Design space 1			Design space 2b
	Run C1.1	**Run C1.2**	**Run C1.3**	**Run C2.1**
Total mass [tonnes]	944.2	891.7	887.5	853.8
Mp mass [tonnes]	472.6	424.1	483.1	413.4
Tp mass [tonnes]	199.3	160.8	157.4	167.1
Tower mass [tonnes]	272.3	306.8	247.0	273.3
Frequency [Hz]	0.0689	0.0614	0.0650	0.0582
D_0 [m]	6.26	5.04	6.04	5.39
$t_{mp,0}$ [mm]	102	104	111	101
$t_{mp,1}$ [mm]	93	94	87	91
t_{tp} [mm]	92	79	72	86
$t_{tw,0}$ [mm]	146	190	158	192
$t_{tw,1}$ [mm]	100	117	89	115
$t_{tw,2}$ [mm]	80	108	60	65
δ_{mp} [deg]	1.59	0.41	1.12	1.08
δ_{tp} [deg]	0.19	0.89	0.77	0.56

In figures 6.17 and 6.18 the DAF for DLC 1.6 at rated and DLC 1.6 at cut-out wind speed of the four solutions are shown, respectively. Next to that, the DAF for these solutions with a damping ratio of 5% are shown, marked with a *. For the solution of run C1.1, which has its frequency closest to the wave excitation frequency of DLC 1.6 at cut-out wind speed (0.0794 Hz), the DAF is decreased from 2.90 to 2.51. For the solution of run C2.1, with its frequency most far away from the wave excitation frequency, the DAF is only decreased from 1.15 to 1.11. The differences for the DAF's of DLC 1.6 at rated wind speed are negligible.

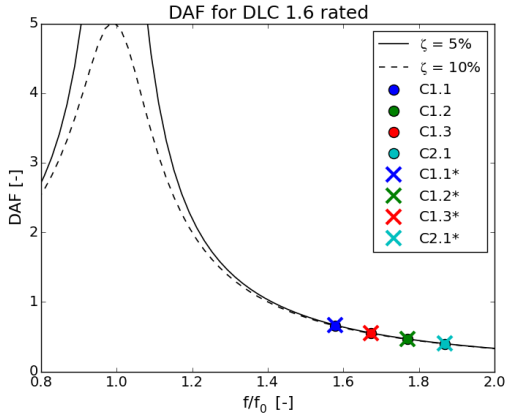

Figure 6.17: DAF for DLC 1.6 at rated wind speed

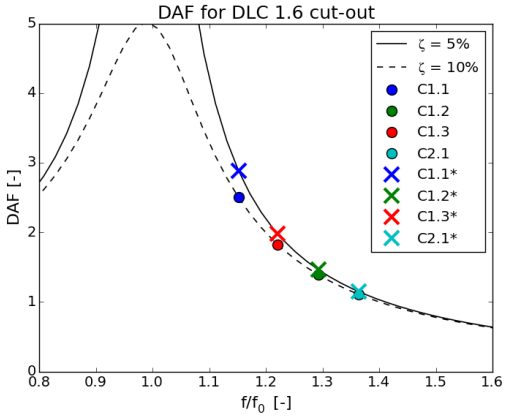

Figure 6.18: DAF for DLC 1.6 at cut-out wind speed

The maximum loading distribution of the solution of run C1.1 does not change when the damping ratio is increased from 5% to 10%, as can been seen in figures 6.19 and 6.20. DLC 6.1 remains the decisive load case at the lower section of the monopile. In figures 6.21 and 6.22, the maximum loading distribution of D2.1 are shown for a damping ratio of 10% and 5% respectively. For this solution, DLC 1.6 at rated wind speed is decisive at the bottom section, for which the loading hardly changes varying the damping ratio. The mass of solution C2.1 is approximately the same as the mass of solution B2.1 and therefore it is concluded that the increase in damping ratio for production load cases will have a negligible impact on the optimal solutions found with the optimization module.

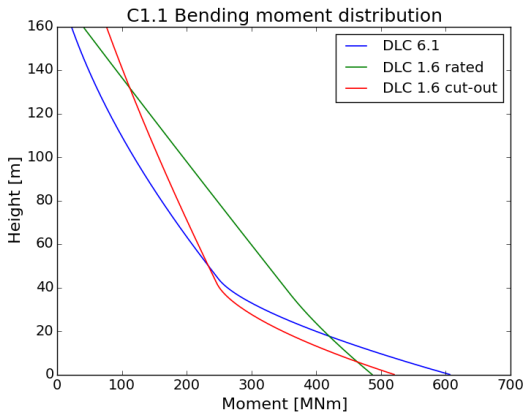

Figure 6.19: Bending distribution of Run C1.1, with ζ = 10%

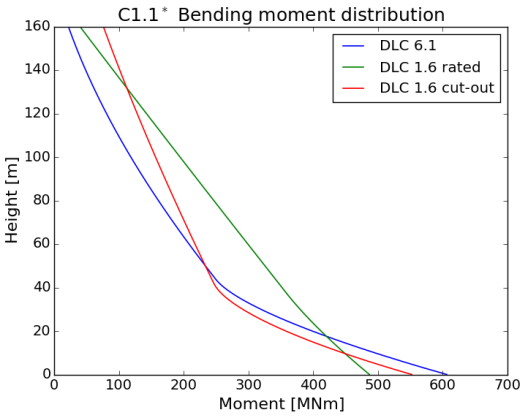

Figure 6.20: Bending distribution of Run C1.1*, with ζ = 5%

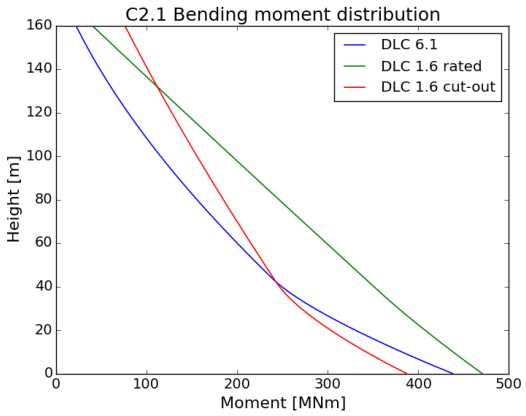

Figure 6.21: Bending distribution of Run C2.1, with ζ = 10%

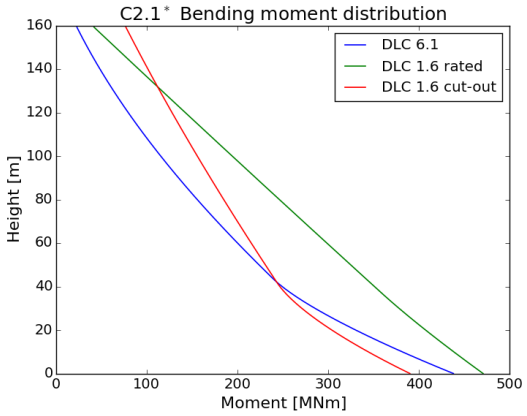

Figure 6.22: Bending distribution of Run C2.1*, with ζ = 5%

6.2.4. Sensitivity on natural frequency

In chapter 3 it was found that the natural frequency is overestimated with approximately 5% in the parametric design model. To identify the influence of this overestimation, optimization runs are carried out in which the natural frequency is corrected with a 5% reduction. The results of the initial three runs using design space 1 and the fourth run using design space 2b are shown in table 6.8.

Table 6.8: Optimization results with frequency correction of 5%

	Design space 1			Design space 2b
	Run D1.1	**Run D1.2**	**Run D1.3**	**Run D2.1**
Total mass [tonnes]	914.7	848.4	883.9	805.6
Mp mass [tonnes]	478.8	435.7	445.7	398.8
Tp mass [tonnes]	155.2	149.7	167.1	154.5
Tower mass [tonnes]	280.7	263.0	271.1	252.3
Frequency [Hz]	0.0625	0.0625	0.0653	0.0584
D_0 [m]	5.80	5.24	5.79	5.90
$t_{mp,0}$ [mm]	118	106	101	87
$t_{mp,1}$ [mm]	86	86	87	80
t_{tp} [mm]	74	67	76	72
$t_{tw,0}$ [mm]	176	147	177	168
$t_{tw,1}$ [mm]	108	91	89	95
$t_{tw,2}$ [mm]	74	80	73	62
δ_{mp} [deg]	1.10	0.23	0.88	0.98
δ_{tp} [deg]	0.69	0.66	0.65	1.05

For all solutions found, the natural frequency constraint would be met as well if the frequency correction of 5% was not applied. However, as found in section 6.2.2, this frequency correction has an effect on the DAF and therefore the loading as well. The DAF for DLC 6.1 for all solutions are shown in figure 6.23. The DAF for D1.1 is the same as D1.2 and therefore not shown. Next to that, the DAF's for these solutions if frequency was not corrected are plotted, marked with a *. For Run D1.3, with a natural frequency closest to the wave excitation frequency, the DAF is increased with 34% from 1.57 to 2.10. The DAF of D2.1, the solution with the lowest natural frequency, the DAF for DLC 6.1 is increased with 24% from 0.96 to 1.19.

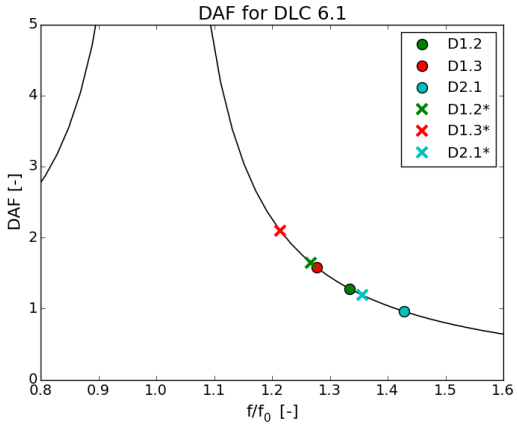

Figure 6.23: Dynamic amplification factor for DLC 6.1

This increase in DAF for solution D1.3 leads to an increase of root bending moment of 10%, as shown in figures 6.24 and 6.25. The root bending moment of solution D2.1 is only increased by 4%, as shown in figures 6.26 and 6.27, respectively.

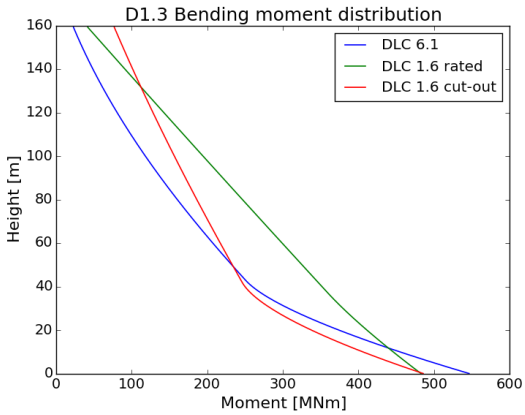

Figure 6.24: Bending moment distribution for Run D1.3

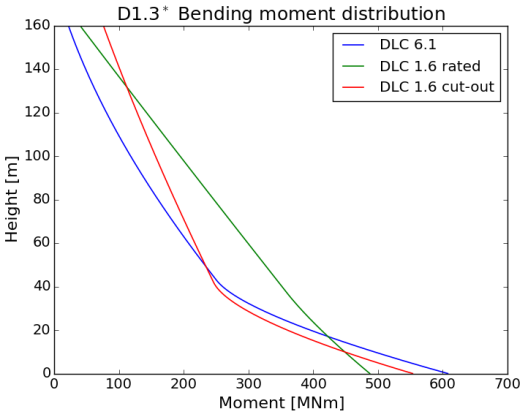

Figure 6.25: Bending moment distribution for Run D1.3*

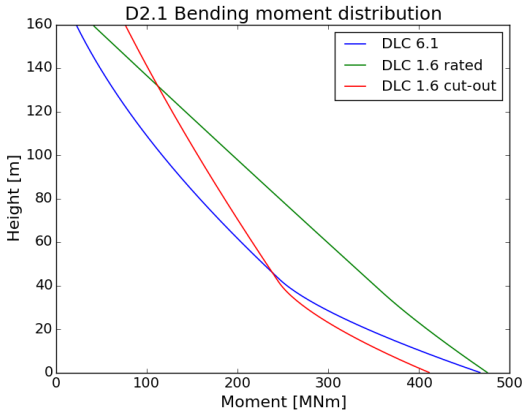

Figure 6.26: Bending moment distribution for Run D2.1

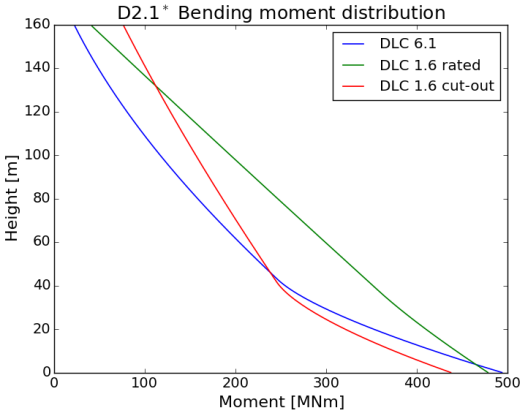

Figure 6.27: Bending moment distribution for Run D2.1*

Due to this increase in maximum loading, the solutions become unfeasible since the monopile buckling constraint will be violated. Therefore, the solutions found with the natural frequency correction would not have been found otherwise. The overestimation of natural frequency will have more effect on feasible solutions found with a natural frequency close to the wave frequency, for which the DAF is increased more intensively

than for solutions with a frequency relatively far from the wave excitation frequency. The correction of 5% lower natural frequency does not necessarily lead to solutions with a significant lower support structure mass, but it will more importantly increase the number of feasible solutions with a natural frequency more close to the wave excitation frequency.

6.3. Conclusion

The optimization module can be used to find multiple feasible solutions with a negligible mass difference for a preliminary design phase. The chance of finding an optimal solution is increased by restricting the design space. The tower top bending moment has significant influence on the mass of the optimal solution, and can therefore not be neglected. Care must be taken if only feasible solutions can be found near the wave excitation frequencies, since the frequency overestimation might lead to an overestimation of the loading on the lower part of the monopile. With a less conservative value of damping ratios for production load cases, no better solutions will be found whereas DLC 6.1 or DLC 1.6 at rated will be decisive along the structure. The optimization algorithm tends to find a solution with a lowest frequency possible, such that DLC 1.6 at rated will be the decisive load case along the support structure, except for the top. However, in chapter 4 it was found that the bending distribution of DLC 6.1 was underestimated in the load estimation model for flexible support structures and should therefore be examined in more detail before it can be concluded that this parametric design and optimization module can be used for preliminary designs.

7

Conclusions & Recommendations

In this chapter, the most important conclusions of this research are discussed. Also recommendations for future work will be provided.

7.1. Conclusions

The goal of this thesis project was to develop a parametric design model with optimization module for a composite wind turbine tower with monopile foundation for offshore wind turbines. From this research, the following conclusions can be drawn:

- The load estimation model uses a quasi-static load analysis method to determine the maximum loading along the support structure. Three load case have been used: DLC 1.6 at rated wind speed, DLC 1.6 at cut-out wind speed and DLC 6.1. If the tower top bending moment is included in the load estimation model, the calculated maximum bending moment distribution will appear to be situated between the average and the maximum loading as obtained with time-domain simulations for a very stiff support structure.
- For flexible support structures, the maximum load estimation is less accurate since dynamic interaction between turbulent wind and wave loading will influence the loading distribution. This is not considered in the quasi-static load model. This dynamic interaction is highest for DLC 1.6 at cut-out wind speed and DLC 6.1, in which the wave excitation frequencies are close to the natural frequency of the support structure. For a flexible support structure, a deviation of approximately 25% has been found between the load estimation model and the results of the time-domain simulations for DLC 6.1. The latter might be the dominant load case along a significant part of a flexible support structure.
- In the load estimation model, the time instant of maximum wave loading has been used for the load analysis. However, time-domain simulations have shown that this time instant is not necessarily equal to the time instant of maximum loading along the complete support structure. This causes the slope in a graph of the bending moment distribution to be larger along the submerged part of the support structure than found with the time-domain simulations.
- In the parametric design model, the yield and buckling constraints of the steel part of the support structure are analyzed using design standard methods. Since these are not valid for composite structures, however, stress analysis methods for composite risers have been used in the parametric design model. These methods were compared with FEM stress analysis and appeared to be applicable for large composite tubes. An approximate solution for pure axial compression has been used for buckling analysis, which gives conservative results compared to semi-analytical buckling analysis for a bending moment using Finstrip.
- Overall, the optimization module using a genetic algorithm can be used to determine multiple (near-) optimal solutions with approximately the same mass. The design of the monopile, transition piece and the top of the tower is driven by the buckling constraint, whereas the design of the lower part of the tower is driven by the yield constraint.

- If the tower top bending moment is taken into account in the maximum loading distribution, the optimization module finds solutions with a mass increase of approximately 20%. Therefore, it is obvious that the maximum tower top bending moment loading can not be omitted in the preliminary design phase.
- The genetic algorithm tends to converge to a solution with a natural frequency to be as low as possible, such that the dynamic amplification of the wave loading is minimzed. Hence, DLC 1.6 at rated wind speed will be the dominant load case. However, as mentioned before, DLC 6.1 is underestimated along a substantial part of the length of a flexible support structure and therefore the maximum loading might be underestimated.

7.2. Recommendations

To improve the accuracy of the parametric design model for a preliminary design phase, the following recommendations are given for future work:

- The fatigue constraint has not been implemented in the parametric model, although this might be a design driving factor. Without the need of computationally demanding time-domain simulations and detailed turbine data, simplified methods in the frequency-domain can be used. However, for the SN-curve of composite materials, apart from the number of cycles for a certain stress range, the mean stress of a load case should be determined as well.
- The optimization module converges to a solution in which DLC 1.6 at rated wind speed is the dominant load case, whereas it has been found that DLC 6.1 was underestimated for flexible support structures compared to the time-domain simulations. To identify the accuracy of the load estimation model, the optimal solution found should be compared with time-domain simulations as well. If DLC 6.1 is indeed the dominant load case, a more accurate load prediction method for flexible towers for this load case should be found.
- The soil factors used in the determination of the soil stiffness show a large variation, which will have an impact on the natural frequency of the support structure. Since the natural frequency of the support structure has an influence on the loading, too, a sensitivity study on these factors needs to be made.
- The optimization algorithm is designed such that it finds a solution with a minimal mass. However, the price of steel and composite materials are not equal, and therefore the lightest support structure will not necessarily be the cheapest. Next to material costs, installation and maintenance will have an effect as well on the levelized cost of energy, and these factors should be taken into account as well to find the optimal design in terms of costs.

A

Composite Tube Properties

In this appendix, the Lekhnitskii stress solutions for a homogenized composite tower and the the method for the determination of the elastic properties of the composite tower are described.

A.1. Lekhnitskii stress solution parameters

In this section, the description of the parameters used in the stress solutions of Lekhnitskii (equations 5.10 and 5.11) are given [58]. The parameters used for the stress determination due to an axial force are given by equations A.1 - A.3. The parameters used for the stress determination due to a bending moment are given by equations A.4 - A.7.

$$\begin{aligned} c_P^r &= \frac{1-c^{k+1}}{1-c^{2k}}\rho^{k-1} + \frac{1-c^{k-1}}{1-c^{2k}}c^{k+1}\rho^{-k-1} \\ c_P^\theta &= \frac{1-c^{k+1}}{1-c^{2k}}k\rho^{k-1} - \frac{1-c^{k-1}}{1-c^{2k}}kc^{k+1}\rho^{-k-1} \\ c_P^z &= \frac{h}{a_{33}}\left[(1-c_P^r)a_{13} + (1-c_P^\theta)a_{23}\right] \end{aligned} \tag{A.1}$$

$$h = \begin{cases} \frac{a_{23}-a_{13}}{\beta_{11}-\beta_{22}} & \text{if } \beta_{11} \neq \beta_{22} \\ 0 & \text{if } \beta_{11} = \beta_{22} \end{cases} \tag{A.2}$$

$$\Omega = \pi b^2(1-c^2) - \frac{2\pi b^2 h}{a_{33}}\left[\frac{1-c^2}{2}(a_{13}+a_{23}) - \frac{(1-c^{k+1})^2}{1-c^{2k}}\frac{a_{13}+ka_{23}}{k+1} - \frac{(1-c^{k-1})^2}{1-c^{2k}}\frac{a_{13}-ka_{23}}{k-1}\right] \tag{A.3}$$

$$\begin{aligned} c_M^r &= \frac{1-c^{m+2}}{1-c^{2m}}\rho^{m-2} + \frac{1-c^{m-2}}{1-c^{2m}}c^{m+2}\rho - m - 2 \\ c_M^\theta &= \frac{1-c^{m+2}}{1-c^{2m}}(1+m)\rho^{m-2} + \frac{1-c^{m-2}}{1-c^{2m}}c^{m+2}(1-m)\rho - m - 2 - 2 \\ c_M^z &= \frac{g}{a_{33}}\left[(1-c_M^r)a_{13} + (1-c_M^\theta)a_{23}\right] \end{aligned} \tag{A.4}$$

$$m = \sqrt{1 + \frac{\beta_{11} + 2\beta_{12} + \beta_{66}}{\beta_{22}}} \tag{A.5}$$

$$g = \begin{cases} \frac{a_{23}-a_{13}}{\beta_{11}+2\beta_{12}+\beta_{66}-3\beta_{22}} & \text{if } m \neq 2 \\ 0 & \text{if } m = 2 \end{cases} \tag{A.6}$$

$$K = \frac{\pi b^4}{4}(1-c^4) - \frac{\pi b^4 g}{a_{33}}\left[\frac{1-c^4}{4}(a_{13}+3a_{23}) - \frac{(1-c^{m+2})^2}{1-c^{2m}}\frac{a_{13}+(1+m)a_{23}}{m+2} - \frac{(1-c^{m-2})^2 c^4}{1-c^{2m}}\frac{a_{13}+(1-m)a_{23}}{m-2}\right] \tag{A.7}$$

A.2. Lekhnitskii coordinate transformation

In this section, the derivation from the compliance matrix of a unidirectional ply to the coordinate system of Lekhnitskii is given. For an unidirectional ply, transverse isotropy can be assumed, by which the general strain stress equation is given by equation A.8 [61].

$$[\boldsymbol{\epsilon}] = [\mathbf{S}][\boldsymbol{\sigma}] = \begin{bmatrix} \epsilon_1 \\ \epsilon_2 \\ \epsilon_3 \\ \gamma_{23} \\ \gamma_{13} \\ \gamma_{12} \end{bmatrix} = \begin{bmatrix} \frac{1}{E_1} & \frac{-\nu_{12}}{E_1} & \frac{-\nu_{12}}{E_1} & 0 & 0 & 0 \\ \frac{-\nu_{12}}{E_1} & \frac{1}{E_2} & \frac{-\nu_{23}}{E_2} & 0 & 0 & 0 \\ -\frac{-\nu_{12}}{E_1} & \frac{-\nu_{23}}{E_2} & \frac{1}{E_2} & 0 & 0 & 0 \\ 0 & 0 & 0 & \frac{1}{G_{23}} & 0 & 0 \\ 0 & 0 & 0 & 0 & \frac{1}{G_{12}} & 0 \\ 0 & 0 & 0 & 0 & 0 & \frac{1}{G_{12}} \end{bmatrix} \begin{bmatrix} \sigma_1 \\ \sigma_2 \\ \sigma_3 \\ \tau_{23} \\ \tau_{13} \\ \tau_{12} \end{bmatrix} \tag{A.8}$$

The reduced compliance matrix $[\bar{\mathbf{S}}^{(i)}]$ for each layer, which has a fiber angle $\phi^{(i)}$ with respect to the global z coordinate is determined with equation A.9, in which $[\mathbf{T}]$ is the transformation matrix, given in A.10.

$$[\bar{\mathbf{S}}^{(\mathbf{i})}] = [\mathbf{T}]^T[\mathbf{S}][\mathbf{T}] \tag{A.9}$$

$$[\mathbf{T}] = \begin{bmatrix} \cos^2\phi^{(i)} & \sin^2\phi^{(i)} & 0 & 0 & 0 & 2\sin\phi^{(i)}\cos\phi^{(i)} \\ \sin^2\phi^{(i)} & \cos^2\phi^{(i)} & 0 & 0 & 0 & -2\sin\phi^{(i)}\cos\phi^{(i)} \\ 0 & 0 & 1 & 0 & 0 & 0 \\ 0 & 0 & 0 & \cos\phi^{(i)} & -\sin\phi^{(i)} & 0 \\ 0 & 0 & 0 & \sin\phi^{(i)} & \cos\phi^{(i)} & 0 \\ -\sin\phi^{(i)}\cos\phi^{(i)} & \sin\phi^{(i)}\cos\phi^{(i)} & 0 & 0 & 0 & \cos^2\phi^{(i)} - \sin^2\phi^{(i)} \end{bmatrix} \tag{A.10}$$

Lekhnitskii uses a different coordinate system. Therefore, the reduced compliance components $a_{ij}^{(i)}$ have to be transformed to this coordinate system using equation A.11, where $[\mathbf{P}]$ is the transformation matrix as given in equation [59].

$$[\bar{\mathbf{S}}_{\mathbf{L}}^{(\mathbf{i})}] = [\mathbf{P}][\bar{\mathbf{S}}^{(\mathbf{i})}][\mathbf{P}] = \begin{bmatrix} a_{11}^{(i)} & a_{12}^{(i)} & a_{13}^{(i)} & a_{14}^{(i)} & 0 & 0 \\ a_{12}^{(i)} & a_{22}^{(i)} & a_{23}^{(i)} & a_{24}^{(i)} & 0 & 0 \\ a_{13}^{(i)} & a_{23}^{(i)} & a_{33}^{(i)} & a_{34}^{(i)} & 0 & 0 \\ a_{14}^{(i)} & a_{24}^{(i)} & a_{34}^{(i)} & a_{44}^{(i)} & 0 & 0 \\ 0 & 0 & 0 & 0 & a_{55}^{(i)} & a_{56}^{(i)} \\ 0 & 0 & 0 & 0 & a_{56}^{(i)} & a_{66}^{(i)} \end{bmatrix} \tag{A.11}$$

$$[\mathbf{P}] = \begin{bmatrix} 0 & 0 & 1 & 0 & 0 & 0 \\ 0 & 1 & 0 & 0 & 0 & 0 \\ 1 & 0 & 0 & 0 & 0 & 0 \\ 0 & 0 & 0 & 0 & 0 & 1 \\ 0 & 0 & 0 & 0 & 1 & 0 \\ 0 & 0 & 0 & 1 & 0 & 0 \end{bmatrix} \tag{A.12}$$

A.3. Homogenized constants

In this section, the homogenized elastic constants for the composite tower are determined using the method of Sun [58]. Next to the reduced compliance terms of each individual layer in the Lekhnitskii coordinate system $a_{ij}^{(i)}$ (equation A.11), the in-plane elastic constants $d_{ij}^{(i)}$ are required for each layer, determined with equation A.13.

$$\begin{bmatrix} d_{22}^{(i)} & d_{23}^{(i)} & d_{24}^{(i)} \\ d_{23}^{(i)} & d_{33}^{(i)} & d_{34}^{(i)} \\ d_{24}^{(i)} & d_{34}^{(i)} & d_{44}^{(i)} \end{bmatrix} = \begin{bmatrix} a_{22}^{(i)} & a_{23}^{(i)} & a_{24}^{(i)} \\ a_{23}^{(i)} & a_{33}^{(i)} & a_{34}^{(i)} \\ a_{24}^{(i)} & a_{34}^{(i)} & a_{44}^{(i)} \end{bmatrix}^{-1} \tag{A.13}$$

From these compliance terms and elastic constants for each individual layer terms the elastic constants for a homogenized cylinder can be determined with the method of Sun. The elastic stiffness in longitudinal direction E_z and Poisson ratio $\nu_{z\theta}$ are determined with equation A.14 and A.16, respectively.

$$E_z = \sum_{i=1}^{n} A_r^{(i)} (d_{33}^{(i)} - d_{23}^{(i)} \nu_{z\theta}) \tag{A.14}$$

$$\nu_{z\theta} = \frac{\sum_{i=1}^{n} t_r^{(i)} d_{23}^{(i)}}{\sum_{i=1}^{n} t_r^{(i)} d_{22}^{(i)}} \tag{A.15}$$

The Poisson ratio's in thickness direction ν_{zr} and ν_{rtheta}, radial stiffness E_r and circumferential stiffness E_θ are determined with equations A.16, A.19, A.17 and A.16.

$$\nu_{zr} = \sum_{i=1}^{n} t_r^{(i)} \left(D_{21}^{(i)} \nu_{z\theta} - D_{31}^{(i)} \right) \tag{A.16}$$

$$E_r = \left(k^2 B_2 + \frac{\nu_{zr}^2}{E_z} \right)^{-1} \tag{A.17}$$

$$E_\theta = \left(B_2 + \frac{\nu_{z\theta}^2}{E_z} \right)^{-1} \tag{A.18}$$

$$\nu_{r\theta} = -E_r \left(C_0 B_2 + \frac{\nu_{zr} \nu_{z\theta}}{E_z} \right) \tag{A.19}$$

A number of new parameters are introduced in these equations. The terms $D_{21}^{(i)}$ and $D_{31}^{(i)}$ for each layer are given by equation A.20.

$$\begin{aligned} D_{21}^{(i)} &= d_{22}^{(i)} a_{12}^{(i)} + d_{23}^{(i)} a_{13}^{(i)} + d_{24}^{(i)} a_{14}^{(i)} \\ D_{31}^{(i)} &= d_{23}^{(i)} a_{12}^{(i)} + d_{33}^{(i)} a_{13}^{(i)} + d_{34}^{(i)} a_{14}^{(i)} \end{aligned} \tag{A.20}$$

The parameters B_0 (equation A.22), B_1 (equation A.23), B_2 (equation A.24) and C_0 (equation A.25) are deducted from the reduced compliance components $\beta_{ij}^{(i)}$, provided with equation A.21.

$$\beta_{jl}^{(i)} = a_{jl}^{(i)} - \frac{a_{j3}^{(i)} a_{l3}^{(i)}}{a_{33}^{(i)}} \tag{A.21}$$

$$B_0 = \sum_{i=1}^{n} C^{(i)} \left(\beta_{12}^{(i)} \frac{\beta_{12}^{(i)} \beta_{44}^{(i)} - \beta_{14}^{(i)} \beta_{24}^{(i)}}{\beta_{22}^{(i)} \beta_{44}^{(i)} - \beta_{24}^{(i)} \beta_{24}^{(i)}} - \beta_{14}^{(i)} \frac{\beta_{12}^{(i)} \beta_{24}^{(i)} - \beta_{14}^{(i)} \beta_{22}^{(i)}}{\beta_{22}^{(i)} \beta_{44}^{(i)} - \beta_{24}^{(i)} \beta_{24}^{(i)}} \right) \tag{A.22}$$

$$B_1 = \sum_{i=1}^{n} C^{(i)} \beta_{11}^{(i)} \tag{A.23}$$

$$\frac{1}{B_2} = \sum_{i=1}^{n} \frac{\beta_{44} C^{(i)}}{\beta_{22}^{(i)} \beta_{44}^{(i)} - \beta_{24}^{(i)} \beta_{24}^{(i)}} \tag{A.24}$$

$$C_0 = \sum_{i=1}^{n} \frac{C^{(i)} \left(\beta_{12}^{(i)} \beta_{44}^{(i)} - \beta_{14}^{(i)} \beta_{24}^{(i)} \right)}{\beta_{22}^{(i)} \beta_{44}^{(i)} - \beta_{24}^{(i)} \beta_{24}^{(i)}} \tag{A.25}$$

The geometric parameter $C^{(i)}$ (equation A.26) depends on the inner and outer radius of each layer, and the parameter k. This parameter k is an indication of transverse isotropy of the homogenized cylinder. Since the properties of the homogenized tube are not known at this point, Sun introduced a nonlinear equation (A.27), which can be solved with the root function in Python.

$$C^{(i)} = \frac{c_{i+1}^k - c_i^k}{1 - c^k} \tag{A.26}$$

$$f(k) = k^2 - C_0^2 - \frac{B_1 - B_0}{B_2} = 0 \tag{A.27}$$

Finally, the three shear moduli $G_{\theta z}$, G_{rz} and $G_{r\theta}$ are obtained with equation A.28, A.29 and A.30. In these equations, $G_{rz}^{(i)}$ and $G_{r\theta}^{(i)}$ are shear moduli of layer i. Since transverse isotropy is assumed for an individual layer, $G_{rz}^{(i)} = G_{\theta z}$. The parameter $Q_{\theta z}^{(i)}$ is determined with equation A.31.

$$G_{\theta z} = \sum_{i=1}^{n} \frac{c_{i+1}^4 - c_i^4}{1 - c^4} Q_{\theta z}^{(i)} \tag{A.28}$$

$$\frac{1}{G_{rz}} = \sum_{i=1}^{n} \frac{\ln(\frac{c_{i+1}}{c_i})}{\ln(\frac{1}{c})} \frac{1}{G_{rz}^{(i)}} \tag{A.29}$$

$$\frac{1}{G_{r\theta}} = \frac{c^2}{1 - c^2} \sum_{i=1}^{n} \left(\frac{1}{c_i^2} - \frac{1}{c_{i+1}^2} \right) \frac{1}{G_{r\theta}^{(i)}} \tag{A.30}$$

$$Q_{\theta z}^{(i)} = \frac{\beta_{22}^{(i)}}{\beta_{22}^{(i)} \beta_{44}^{(i)} - \beta_{24}^{(i)} \beta_{24}^{(i)}} \tag{A.31}$$

The developed model for the determination of the elastic constants of the composite tower is verified using an example described in [58]. A carbon/epoxy ply is used with a [0/90/0] laminate layup, each layer 10 mm thick. The inner and outer radius of the tube are 20 mm and 50 mm, respectively. The mechanical properties of the carbon/epoxy ply and homogenized elastic properties listed in table A.1. The Poisson ratio's are given in opposite direction as determined, and are interchanged using equation A.32 [58].

Table A.1: Homogenized tube properties

Carbon/epoxy ply [58]			**Ref [58]**	**Model**
E_1 [GPa]	138.0	E_r [GPa]	14.94	15.06
E_2 [GPa]	14.5	E_θ [GPa]	55.91	55.91
E_3 [GPa]	14.5	E_z [GPa]	97.12	97.12
G_{23} [GPa]	5.86	$G_{\theta z}$ [GPa]	5.86	5.86
G_{13} [GPa]	5.86	G_{rz} [GPa]	5.86	5.86
G_{12} [GPa]	5.86	$G_{r\theta}$ [GPa]	5.86	5.86
ν_{23} [-]	0.21	$\nu_{\theta z}$ [-]	0.031	0.031
ν_{13} [-]	0.21	ν_{rz} [-]	0.035	0.035
ν_{12} [-]	0.21	$\nu_{r\theta}$ [-]	0.059	0.059

$$\frac{\nu_{ij}}{E_i} = \frac{\nu_{ji}}{E_j} \tag{A.32}$$

A.4. Bending stiffness

The bending stiffness of the composite tube is determined with the prescribed method by Chan [41], in which the following assumptions are made:

- An infinitesimal element of the tube is considered as a plate, as shown in figure A.1. The effect of curvature is neglected.
- Thin walled: Higher order thickness terms are neglected.

The bending stiffness EI_{eff} of the composite tube can be determined with equation A.4, in which d_{11} is the (4,4) element of the inverse $[\bar{\boldsymbol{A}}\bar{\boldsymbol{B}}\bar{\boldsymbol{D}}]$ matrix.

$$EI_{eff} = \frac{1}{d_{11}}$$

These stiffness matrices can be determined with equations A.33, A.34 and A.35. In these Equations, the $[\boldsymbol{A}]$, $[\boldsymbol{B}]$ and $[\boldsymbol{D}]$ terms are the ABD matrix of a composite plate, determined with classical lamination theory.

$$\bar{\boldsymbol{A}} = \int_0^{2\pi} [\boldsymbol{A}] \cdot R d\theta = [\boldsymbol{A}] \cdot \left(\frac{D_{inner}}{2} + \frac{t}{2} \right) \cdot 2\pi \tag{A.33}$$

$$\bar{\boldsymbol{B}} = \int_0^{2\pi} ([\boldsymbol{B}] + R \cdot \cos(\theta)[\boldsymbol{A}]) \cdot R d\theta = [\boldsymbol{B}] \cdot \left(\frac{D_{inner}}{2} + \frac{t}{2} \right) \cdot 2\pi \tag{A.34}$$

$$\begin{aligned} \bar{\boldsymbol{D}} = & \int_0^{2\pi} \left([\boldsymbol{D}] + 2R \cdot \cos(\theta) \cdot [\boldsymbol{B}] + (R \cdot \cos(\theta))^2 [\boldsymbol{A}] \right) \cdot R d\theta = \\ & [\boldsymbol{D}] \cdot \left(\frac{D_{inner}}{2} + \frac{t}{2} \right) \cdot 2\pi + \pi \left(\frac{D_{inner}}{2} + \frac{t}{2} \right)^3 \cdot [\boldsymbol{A}] \end{aligned} \tag{A.35}$$

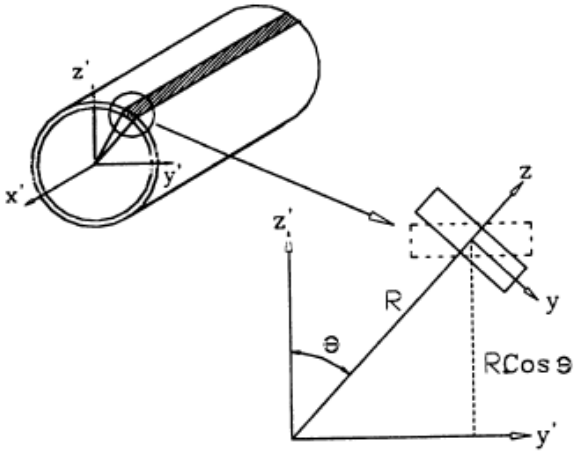

Figure A.1: Plate element of composite tube [41]

B

Timoshenko Mass and Stiffness Matrices

The stiffness matrix of a beam element $\boldsymbol{K^e}$ with three degrees of freedom at each of the two nodes can be separated into four stiffness matrices [11, 68]:

$$\bar{\boldsymbol{K}}^{\boldsymbol{e}} = \bar{\boldsymbol{K}}_{\boldsymbol{b}}^{\boldsymbol{e}} + \bar{\boldsymbol{K}}_{\boldsymbol{t}}^{\boldsymbol{e}} + \bar{\boldsymbol{K}}_{\boldsymbol{s}}^{\boldsymbol{e}} - \bar{\boldsymbol{K}}_{\boldsymbol{g}}^{\boldsymbol{e}} \tag{B.1}$$

These five matrices are determined using Timoshenko beam elements. The element bending stiffness matrix is given by:

$$\bar{\boldsymbol{K}}_{\boldsymbol{b}}^{\boldsymbol{e}} = \int_0^l \boldsymbol{B_b}^T EI \boldsymbol{B_b} dx \tag{B.2}$$

The translational stiffness matrix is given by:

$$\bar{\boldsymbol{K}}_{\boldsymbol{t}}^{\boldsymbol{e}} = \int_0^l \boldsymbol{B_t}^T EA \boldsymbol{B_t} dx \tag{B.3}$$

The shear stiffness matrix is given by:

$$\bar{\boldsymbol{K}}_{\boldsymbol{s}}^{\boldsymbol{e}} = \int_0^l \boldsymbol{B_s}^T kGA \boldsymbol{B_s} dx \tag{B.4}$$

The geometric stiffness matrix is given by:

$$\bar{\boldsymbol{K}}_{\boldsymbol{g}}^{\boldsymbol{e}} = \int_0^l P \boldsymbol{B_v}^T \boldsymbol{B_v} dx \tag{B.5}$$

Here is P the load on the element due to the weight of the RNA and the weight of the structure. The **B** terms are derivates of the shape functions, provided later on in this appendix. The element mass matrix consists of a translational and a rotary inertia part:

$$\bar{\boldsymbol{M}}^{\boldsymbol{e}} = \bar{\boldsymbol{M}}_{\boldsymbol{t}}^{\boldsymbol{e}} + \bar{\boldsymbol{M}}_{\boldsymbol{r}}^{\boldsymbol{e}} \tag{B.6}$$

The translational mass matrix is given by:

$$\bar{\boldsymbol{M}}_{\boldsymbol{t}} = \int_0^l \boldsymbol{N_u}^T \rho A \boldsymbol{N_u} dx + \int_0^l \boldsymbol{N_v}^T \rho A \boldsymbol{N_v} dx \tag{B.7}$$

The rotational mass matrix is given by:

$$\bar{\boldsymbol{M}}_{\boldsymbol{r}} = \int_0^l \boldsymbol{N_\theta}^T \rho I \boldsymbol{N_\theta} dx \tag{B.8}$$

The shape functions for a two degree of freedom Timoshenko beam element, including a lateral and rotational displacement, have been given by [69]. To include the axial displacement, shape functions of a bar element as provided by [11] have been added. The shape functions for the axial displacement u are given by:

$$\boldsymbol{N_u} = [N_{u_1} \quad N_{u_2} \quad N_{u_3} \quad N_{u_4} \quad N_{u_5} \quad N_{u_6}] \tag{B.9}$$

$$N_{u_1} = 1-\zeta \tag{B.10}$$
$$N_{u_2} = 0 \tag{B.11}$$
$$N_{u_3} = 0 \tag{B.12}$$
$$N_{u_4} = \zeta \tag{B.13}$$
$$N_{u_5} = 0 \tag{B.14}$$
$$N_{u_6} = 0 \tag{B.15}$$

The shape functions for the lateral displacement v are given by:

$$\boldsymbol{N_v} = [N_{v_1} \quad N_{v_2} \quad N_{v_3} \quad N_{v_4} \quad N_{v_5} \quad N_{v_6}] \tag{B.16}$$

$$N_{v_1} = 0 \tag{B.17}$$
$$N_{v_2} = \frac{1-3\zeta^2+2\zeta^3+(1-\zeta)\phi}{1+\phi} \tag{B.18}$$
$$N_{v_3} = \frac{(\zeta-2\zeta^2+\zeta^3+(\zeta-\zeta^2)\frac{\phi}{2})l}{1+\phi} \tag{B.19}$$
$$N_{v_4} = 0 \tag{B.20}$$
$$N_{v_5} = \frac{3\zeta^2-2\zeta^3+\zeta\phi}{1+\phi} \tag{B.21}$$
$$N_{v_6} = \frac{(-\zeta^2+\zeta^3-(\zeta-\zeta^2)\frac{\phi}{2})l}{1+\phi} \tag{B.22}$$

The shape functions for the rotational displacement θ are given by:

$$\boldsymbol{N_\theta} = [N_{\theta_1} \quad N_{\theta_2} \quad N_{\theta_3} \quad N_{\theta_4} \quad N_{\theta_5} \quad N_{\theta_6}] \tag{B.23}$$

$$N_{\theta_1} = 0 \tag{B.24}$$
$$N_{\theta_2} = \frac{6(-\zeta+\zeta^2)}{l(1+\phi)} \tag{B.25}$$
$$N_{\theta_3} = \frac{1-4\zeta+3\zeta^2+(1-\zeta)\phi}{1+\phi} \tag{B.26}$$
$$N_{\theta_4} = 0 \tag{B.27}$$
$$N_{\theta_5} = \frac{6(\zeta-\zeta^2)}{l(1+\phi)} \tag{B.28}$$
$$N_{\theta_6} = \frac{-2\zeta+3\zeta^2+\zeta\phi}{1+\phi} \tag{B.29}$$

The shear parameter ϕ, shear correction parameter k and nondimensional coordinate ζ are given by:

$$\phi = \frac{12EI}{kGAl^2} \tag{B.30}$$
$$\zeta = \frac{x}{l} \tag{B.31}$$
$$k = \frac{6\left(R_i^2+R_o^2\right)^2\cdot(1+\nu)^2}{7R_i^4+34R_i^2R_o^2+7R_o^4+\nu\left(12R_i^4+48R_i^2R_o^2+12R_o^4\right)+\nu^2\left(4R_i^4+16R_i^2R_o^2+4R_o^4\right)} \tag{B.32}$$

And the derivatives of the shape functions are given by:

$$\boldsymbol{B_b} = \frac{\partial}{\partial x}\boldsymbol{N_\theta} \tag{B.33}$$
$$\boldsymbol{B_t} = \frac{\partial}{\partial x}\boldsymbol{N_u} \tag{B.34}$$
$$\boldsymbol{B_s} = \frac{\partial}{\partial x}\boldsymbol{N_v} - \boldsymbol{N_\theta} \tag{B.35}$$
$$\boldsymbol{B_v} = \frac{\partial}{\partial x}\boldsymbol{N_v} \tag{B.36}$$

The resulting matrix terms for the rotational and lateral displacements are taken from [68, 70] [1] [2]. For the translational terms, the matrix terms as given in [11] are used. The derivation of these matrices is checked.

$$\boldsymbol{\bar{K}_b^e} = \frac{EI}{l^3(1+\phi)^2}\begin{bmatrix} 0 & 0 & 0 & 0 & 0 & 0 \\ 0 & 12 & 6l & 0 & -12 & 6l \\ 0 & 6l & (4+2\phi+\phi^2)l^2 & 0 & -6l & (2-2\phi-\phi^2)l^2 \\ 0 & 0 & 0 & 0 & 0 & 0 \\ 0 & -12 & -6l & 0 & 12 & -6l \\ 0 & 6l & (2-2\phi-\phi^2)l^2 & 0 & -6l & (4+2\phi+\phi^2)l^2 \end{bmatrix} \tag{B.37}$$

[1] In [68] a typo is made in the bending stiffness matrix: $\frac{EI}{l^2(1+\phi)^2}$ should be $\frac{EI}{l^3(1+\phi)^2}$.

[2] The $M_r^e(3,6)$ and $M_r^e(6,3)$ matrix elements have a typo in [68], there should be a $-$ sign in front of the term $\frac{\phi^2}{6}$ according to [70]

$$\tilde{\boldsymbol{K}}_{\boldsymbol{t}}^{\boldsymbol{e}} = \begin{bmatrix} \frac{EA}{l} & 0 & 0 & -\frac{EA}{l} & 0 & 0 \\ 0 & 0 & 0 & 0 & 0 & 0 \\ 0 & 0 & 0 & 0 & 0 & 0 \\ -\frac{EA}{l} & 0 & 0 & \frac{EA}{l} & 0 & 0 \\ 0 & 0 & 0 & 0 & 0 & 0 \\ 0 & 0 & 0 & 0 & 0 & 0 \end{bmatrix} \tag{B.38}$$

$$\tilde{\boldsymbol{K}}_{\boldsymbol{s}}^{\boldsymbol{e}} = \frac{kGA\phi^2}{4l(1+\phi)^2} \begin{bmatrix} 0 & 0 & 0 & 0 & 0 & 0 \\ 0 & 4 & 2l & 0 & -4 & 2l \\ 0 & 2l & l^2 & 0 & -2l & l^2 \\ 0 & 0 & 0 & 0 & 0 & 0 \\ 0 & -4 & -2l & 0 & 4 & -2l \\ 0 & 2l & l^2 & 0 & -2l & l^2 \end{bmatrix} \tag{B.39}$$

$$\tilde{\boldsymbol{K}}_{\boldsymbol{g}}^{\boldsymbol{e}} = \frac{P}{l(1+\phi)^2} \begin{bmatrix} (0 & 0 & 0 & 0 & 0 & 0 \\ 0 & \frac{6}{5}+2\phi+\phi^2 & \frac{1}{10}l & 0 & -(\frac{6}{5}+2\phi+\phi^2) & \frac{1}{10}l \\ 0 & \frac{1}{10}l & (\frac{2}{15}+\frac{\phi}{6}+\frac{\phi^2}{12})l^2 & 0 & -\frac{1}{10}l & -(\frac{1}{30}+\frac{\phi}{6}+\frac{\phi^2}{12})l^2 \\ 0 & 0 & 0 & 0 & 0 & 0 \\ 0 & -(\frac{6}{5}+2\phi+\phi^2) & -\frac{1}{10}l & 0 & \frac{6}{5}+2\phi+\phi^2 & -\frac{1}{10}l \\ 0 & \frac{1}{10}l & -(\frac{1}{30}+\frac{\phi}{6}+\frac{\phi^2}{12})l^2 & 0 & -\frac{1}{10}l & (\frac{2}{15}+\frac{\phi}{6}+\frac{\phi^2}{12})l^2 \end{bmatrix} \tag{B.40}$$

$$\tilde{\boldsymbol{M}}_{\boldsymbol{t}}^{\boldsymbol{e}} = \frac{\rho Al}{(1+\phi)^2} \begin{bmatrix} \frac{1}{3}(1+\phi)^2 & 0 & 0 & \frac{1}{6}(1+\phi)^2 & 0 & 0 \\ 0 & \frac{13}{35}+\frac{7\phi}{10}+\frac{\phi^2}{3} & \left(\frac{11}{210}+\frac{11\phi}{120}+\frac{\phi^2}{24}\right)l & 0 & \frac{9}{70}+\frac{3\phi}{10}+\frac{\phi^2}{6} & -\left(\frac{13}{420}+\frac{3\phi}{40}+\frac{\phi^2}{24}\right)l \\ 0 & \left(\frac{11}{210}+\frac{11\phi}{120}+\frac{\phi^2}{24}\right)l & \left(\frac{1}{105}+\frac{\phi}{60}+\frac{\phi^2}{120}\right)l^2 & 0 & \left(\frac{13}{420}+\frac{3\phi}{40}+\frac{\phi^2}{24}\right)l & -\left(\frac{1}{140}+\frac{\phi}{60}+\frac{\phi^2}{120}\right)l^2 \\ \frac{1}{6}(1+\phi)^2 & 0 & 0 & \frac{1}{3}(1+\phi)^2 & 0 & 0 \\ 0 & \frac{9}{70}+\frac{3\phi}{10}+\frac{\phi^2}{6} & \left(\frac{13}{420}+\frac{3\phi}{40}+\frac{\phi^2}{24}\right)l & 0 & \frac{13}{35}+\frac{7\phi}{10}+\frac{\phi^2}{3} & -\left(\frac{11}{210}+\frac{11\phi}{120}+\frac{\phi^2}{24}\right)l \\ 0 & -\left(\frac{13}{420}+\frac{3\phi}{40}+\frac{\phi^2}{24}\right)l & -\left(\frac{1}{140}+\frac{\phi}{60}+\frac{\phi^2}{120}\right)l^2 & 0 & -\left(\frac{11}{210}+\frac{11\phi}{120}+\frac{\phi^2}{24}\right)l & \left(\frac{1}{105}+\frac{\phi}{60}+\frac{\phi^2}{120}\right)l^2 \end{bmatrix} \tag{B.41}$$

$$\tilde{\boldsymbol{M}}_{\boldsymbol{r}}^{\boldsymbol{e}} = \frac{\rho Al}{(1+\phi)^2}\left(\frac{r_g}{l}\right)^2 \begin{bmatrix} 0 & 0 & 0 & 0 & 0 & 0 \\ 0 & \frac{6}{5} & (\frac{1}{10}-\frac{\phi}{2})l & 0 & -\frac{6}{5} & (\frac{1}{10}-\frac{\phi}{2})l \\ 0 & (\frac{1}{10}-\frac{\phi}{2})l & (\frac{2}{15}+\frac{\phi}{6}+\frac{\phi^2}{3})l^2 & 0 & -(\frac{1}{10}-\frac{\phi}{2})l & -(\frac{1}{30}+\frac{\phi}{6}-\frac{\phi^2}{6})l^2 \\ 0 & 0 & 0 & 0 & 0 & 0 \\ 0 & -\frac{6}{5} & -(\frac{1}{10}-\frac{\phi}{2})l & 0 & \frac{6}{5} & -(\frac{1}{10}-\frac{\phi}{2})l \\ 0 & (\frac{1}{10}-\frac{\phi}{2})l & -(\frac{1}{30}+\frac{\phi}{6}-\frac{\phi^2}{6})l^2 & 0 & -(\frac{1}{10}-\frac{\phi}{2})l & (\frac{2}{15}+\frac{\phi}{6}+\frac{\phi^2}{3})l^2 \end{bmatrix} \tag{B.42}$$

Where the radius of gyration r_g is given by:

$$r_g = \sqrt{\frac{I}{A}} \tag{B.43}$$

C

Elaboration on Hydrodynamics

In this appendix the coefficients used for the 5th order Stokes wave theory are provided, together with the derivation of the other kinematic terms. Next to that, the drag and inertia coefficient are provided.

C.1. 5th Order Stokes wave theory

The coefficients used for the 5th order Stokes wave as used by Fenton [47] are given in figure C.1.

$$
\begin{aligned}
A_{11} &= 1/\sinh kd \\
A_{22} &= 3S^2/[2(1-S)^2] \\
A_{31} &= (-4-20S+10S^2-13S^3)/[8\sinh kd\,(1-S)^3] \\
A_{33} &= (-2S^2+11S^3)/[8\sinh kd\,(1-S)^3] \\
A_{42} &= (12S-14S^2-264S^3-45S^4-13S^5)/[24(1-S)^5] \\
A_{44} &= (10S^3-174S^4+291S^5+278S^6)/[48(3+2S)(1-S)^5] \\
A_{51} &= (-1{,}184+32S+13{,}232S^2+21{,}712S^3+20{,}940S^4+12{,}554S^5-500S^6 \\
&\quad -3{,}341S^7-670S^8)/[64\sinh kd\,(3+2S)(4+S)(1-S)^6] \\
A_{53} &= (4S+105S^2+198S^3-1{,}376S^4-1{,}302S^5-117S^6+58S^7)/ \\
&\quad [32\sinh kd\,(3+2S)(1-S)^6] \\
A_{55} &= (-6S^3+272S^4-1{,}552S^5+852S^6+2{,}029S^7+430S^8)/ \\
&\quad [6\sinh kd\,(3+2S)(4+S)(1-S)^6] \\
B_{22} &= \coth kd\,(1+2S)/[2(1-S)] \\
B_{31} &= -3(1+3S+3S^2+2S^3)/[8(1-S)^3] \\
B_{42} &= \coth kd\,(6-26S-182S^2-204S^3-25S^4+26S^5)/[6(3+2S)(1-S)^4] \\
B_{44} &= \coth kd\,(24+92S+122S^2+66S^3+67S^4+34S^5)/[24(3+2S)(1-S)^4] \\
B_{53} &= 9(132+17S-2{,}216S^2-5{,}897S^3-6{,}292S^4-2{,}687S^5+194S^6 \\
&\quad +467S^7+82S^8)/[128(3+2S)(4+S)(1-S)^6] \\
B_{55} &= 5(300+1{,}579S+3{,}176S^2+2{,}949S^3+1{,}188S^4+675S^5+1{,}326S^6 \\
&\quad +827S^7+130S^8/[384(3+2S)(4+S)(1-S)^6] \\
C_0 &= (\tanh kd)^{1/2} \\
C_2 &= (\tanh kd)^{1/2}\,(2+7S^2)/[4(1-S)^2] \\
C_4 &= (\tanh kd)^{1/2}\,(4+32S-116S^2-400S^3-71S^4+146S^5)/[32(1-S)^5] \\
D_2 &= -(\coth kd)^{1/2}/2 \\
D_4 &= (\coth kd)^{1/2}\,(2+4S+S^2+2S^3)/[8(1-S)^3] \\
E_2 &= \tanh kd\,(2+2S+5S^2)/[4(1-S)^2] \\
E_4 &= \tanh kd\,(8+12S-152S^2-308S^3-42S^4+77S^5)/[32(1-S)^5]
\end{aligned}
$$

Figure C.1: Fenton coefficients, with S = $\cosh^{-1}$ (kd) [71][1]

[1] In [71] a correction was made for the A_{55} coefficient

.

The total derivative of the wave velocity is given by equation C.1 [49]. The derivation of $\frac{\partial u}{\partial t}$, v, $\frac{\partial u}{\partial x}$ and $\frac{\partial u}{\partial z}$ is given in equation C.2, C.3, C.4 and C.5, respectively.

$$a(x,z,t) = \frac{Du}{Dt} = \frac{\partial u}{\partial t} + u\frac{\partial u}{\partial x} + v\frac{\partial u}{\partial z} \tag{C.1}$$

$$\begin{aligned}\frac{\partial u}{\partial t} = C_0\sqrt{\frac{g}{k}}\big[&\omega(\epsilon^1 A_{11} + \epsilon^3 A_{31} + \epsilon^5 A_{51})\cosh(kz)\sin(\theta)\\ &+4\omega(\epsilon^2 A_{22} + \epsilon^4 A_{42})\cosh(2kz)\sin(2\theta)\\ &+9\omega(\epsilon^3 A_{33} + \epsilon^5 A_{53})\cosh(3kz)\sin(2\theta)\\ &+16\omega\epsilon^4 A_{44}\cosh(4kz)\sin(4\theta)\\ &+25\omega\epsilon^5 A_{55}\cosh(5kz)\sin(5\theta)\big]\end{aligned} \tag{C.2}$$

$$\begin{aligned}v = \frac{\partial \phi}{\partial z} = C_0\sqrt{\frac{g}{k}}\big[&(\epsilon^1 A_{11} + \epsilon^3 A_{31} + \epsilon^5 A_{51})\sinh(kz)\cos(\theta)\\ &+2(\epsilon^2 A_{22} + \epsilon^4 A_{42})\sinh(2kz)\cos(2\theta)\\ &+3(\epsilon^3 A_{33} + \epsilon^5 A_{53})\sinh(3kz)\cos(3\theta)\\ &+4\epsilon^4 A_{44}\sinh(4kz)\cos(4\theta)\\ &+5\epsilon^5 A_{55}\sinh(5kz)\cos(5\theta)\big]\end{aligned} \tag{C.3}$$

$$\begin{aligned}\frac{\partial u}{\partial x} = -C_0\sqrt{gk}\big[&(\epsilon^1 A_{11} + \epsilon^3 A_{31} + \epsilon^5 A_{51})\cosh(kz)\sin(\theta)\\ &+4(\epsilon^2 A_{22} + \epsilon^4 A_{42})\cosh(2kz)\sin(2\theta)\\ &+9(\epsilon^3 A_{33} + \epsilon^5 A_{53})\cosh(3kz)\sin(3\theta)\\ &+16\epsilon^4 A_{44}\cosh(4kz)\sin(4\theta)\\ &+25\epsilon^5 A_{55}\cosh(5kz)\sin(5\theta)\big]\end{aligned} \tag{C.4}$$

$$\begin{aligned}\frac{\partial u}{\partial z} = C_0\sqrt{gk}\big[&(\epsilon^1 A_{11} + \epsilon^3 A_{31} + \epsilon^5 A_{51})\sinh(kz)\cos(\theta)\\ &+4(\epsilon^2 A_{22} + \epsilon^4 A_{42})\sinh(2kz)\cos(2\theta)\\ &+9(\epsilon^3 A_{33} + \epsilon^5 A_{53})\sinh(3kz)\cos(3\theta)\\ &+16\epsilon^4 A_{44}\sinh(4kz)\cos(4\theta)\\ &+25\epsilon^5 A_{55}\sinh(5kz)\cos(5\theta)\big]\end{aligned} \tag{C.5}$$

C.2. Wave kinematics verification

The implementation of the wave kinematics into the parametric design model is verified using the wave kinematics tool developed by Fenton [72] is used. This tool can be used to calculate the wave kinematics for several wave theories, including 5th order Stokes theory. The output of the program consists of e.g. the surface elevation, horizontal velocity and acceleration terms for one half wave period, as derived above. These are non-dimensionalized by mean water depth d and gravitational acceleration g. In table C.1, the dimensionalized values of Fenton and the results of the parametric model for the surface elevation, horizontal velocity and acceleration at surface level are given, for the DLC 6.1 load case described in chapter 4. The wave period is increased to 12 seconds, such that, such that the time steps used in Fenton corresponds to 0.5 seconds. Only a significant difference is found at 2.5 seconds for the surface elevation. This is due to the fact that different values near zero will have a relative high error. Comparing the absolute values, only a difference of 0.05 m is found, which is acceptable.

Table C.1: Wave kinematics verification

	Elevation [m]			Hor. Velocity [m/s]			Hor. Acceleration [m/s^2]		
Time [s]	**Fenton**	**Model**	**[%]**	**Fenton**	**Model**	**[%]**	**Fenton**	**Model**	**[%]**
0	10.6353	10.6948	0.6	7.9958	8.0129	0.2	0.0000	0.0000	0.0
0.5	9.6841	9.6982	0.2	7.2295	7.2337	0.1	-1.7222	-1.7224	0.0
1	7.2622	7.2093	-0.7	5.3943	5.3848	-0.2	-2.8211	-2.8133	-0.3
1.5	4.3349	4.2932	-1.0	3.3345	3.3303	-0.1	-3.1419	-3.1348	-0.2
2.0	1.7199	1.7487	1.7	1.5383	1.5374	-0.1	-2.9316	-2.9340	0.1
2.5	-0.3194	-0.2600	-19.0	0.1113	0.1097	-1.4	-2.4609	-2.4637	0.1
3.0	-1.8989	-1.8998	0.0	-0.9594	-0.9587	-0.1	-1.9140	-1.9134	0.0
3.5	-3.1871	-3.2446	1.8	-1.7257	-1.7228	-0.2	-1.4218	-1.4214	0.0
4.0	-4.2050	-4.2335	0.7	-2.2676	-2.2665	-0.1	-1.0395	-1.0393	0.0
4.5	-4.9210	-4.8782	-0.9	-2.6535	-2.6562	0.1	-0.7486	-0.7477	-0.1
5.0	-5.3598	-5.3095	-0.9	-2.9226	-2.9250	0.1	-0.5003	-0.5001	0.0
5.5	-5.5914	-5.6085	0.3	-3.0859	-3.0843	-0.1	-0.2550	-0.2554	0.2
6.0	-5.6651	-5.7252	1.0	-3.1397	-3.1371	-0.1	0.0000	0.0000	0.0

The differences between surface elevation, wave velocity and acceleration between the wave generated with Focus6 Streamfunction and the 5th order Stokes theory used in the parametric model for the same wave parameters as described above is shown in figures C.2, C.3 and C.4, respectively. In Focus6, it is recommended to use at least a Streamfunction with order 11 [44]. The differences are found to be negligible.

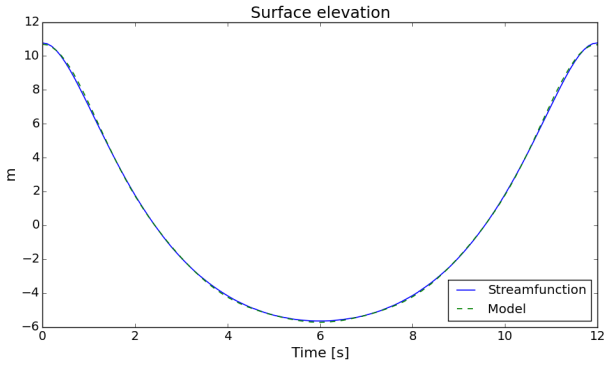

Figure C.2: Surface elevation

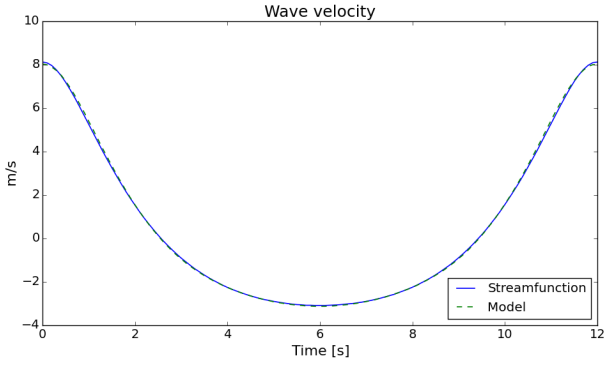

Figure C.3: Wave velocity at crest height

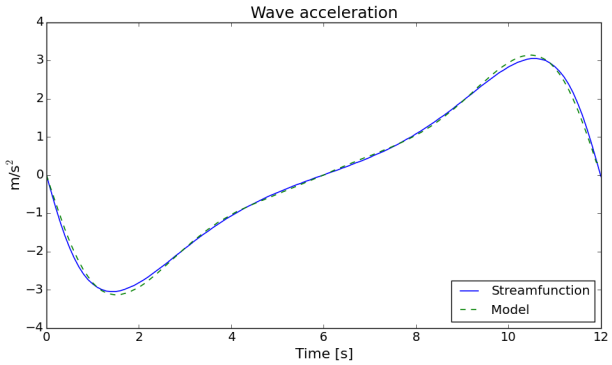

Figure C.4: Wave acceleration at crest height

C.3. Wave drag and inertia coefficient

The drag C_D and inertia C_m coefficient for waves are determined differently for different design standards [48]. The GL [73] and DNV standard [32] are outlined in this section.

In the DNV standard, the drag coefficient C_D is dependent on the relative roughness C_{DS} and a wake amplification factor Ψ, as given in equation C.6 [46]. The relative roughness is determined with equation C.7 and the wake amplification factor can be read of from figure C.5. For relative roughness values inbetween smooth and rough, linear interpolation can be used. New uncoated steel and painted steel can be assumed to be smooth. In the case of marine growth, the surface roughness k_r has a value between 0.005-0.05.

$$C_{D,p} = C_{DS} \cdot \psi \tag{C.6}$$

$$C_{DS} = \begin{cases} 0.65 & \text{for } k_r/D_p \leq 10^{-4} \text{ (smooth)} \\ \frac{29+4\log\frac{k_r}{D_p}}{20} & \text{for } 10^{-4} < k_r/D_p < 10^{-2} \\ 1.05 & \text{for } k_r/D_p \geq 10^{-2} \text{ (rough)} \end{cases} \tag{C.7}$$

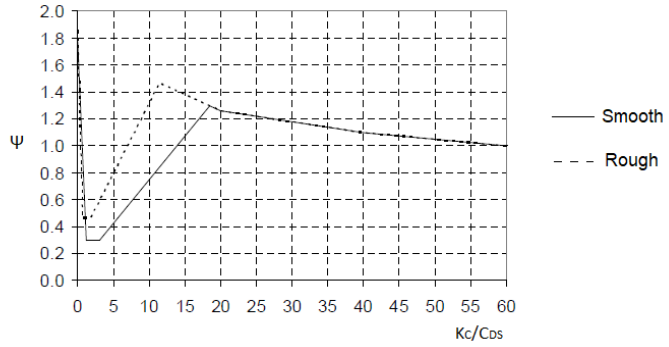

Figure C.5: Wake amplification factor [32]

The inertia coefficient C_m is used for the determination of the inertia part of the wave loading. The value of the inertia coefficient differs per load case and is determined with equation C.8. The Keulegan-Carpenter number (KC) is determined with equation C.9. Here is u_{max} the maximum wave velocity at still water level.

$$C_m = \begin{cases} 2.0 & \text{for KC} < 3.0 \\ \max\left[2.0 - 0.044(\text{KC}-3); 1.6 - (C_{DS} - 0.65)\right] & \text{for KC} > 3.0 \end{cases} \tag{C.8}$$

$$\text{KC} = \frac{u_{max} T_p}{D_p} \tag{C.9}$$

In the GL guideline, only a distinction is made between a smooth and rough cylinder and Reynolds number (R_e), as can been seen in table C.2. The Reynolds number is determined with equation C.10 [73].

$$R_e = \frac{u_{max} D_p}{1.5 \cdot 10^{-5}} \tag{C.10}$$

Table C.2: Drag and Inertia coefficient according to GL [73]

	Smooth cylinder		**Rough cylinder**	
Reynolds number	$C_{D,p}$	C_m	$C_{D,p}$	C_m
$\leq 2 \cdot 10^5$	1.2	2.0	1.2	2.0
$> 2 \cdot 10^5$	0.7	2.0	1.1	1.6

Since it is hard to integrate the graph of the DNV guideline into the parametric model, for simplicity the default values for C_D and C_m of the GL guideline will be used. Considering the Borssele DLC 6.1 wave, the Reynolds number is larger than $2 \cdot 10^5$. For simplicity, it will be assumed that no marine growth is present and that the values of a smooth cylinder will be valid along the complete monopile structure. The sensitivity of this choice on maximum loading along the monopile is left for future work.

D

Focus6 Results

D.1. Eigenmodes

In table D.1 the frequencies of the eigenmodes of the three tower concepts as described in section 4.4.2 determined in Focus6 are summarised. The first two fore aft bending mode shapes for the three tower concepts are plotted in figures D.1 and D.2, respectively.

Table D.1: Natural frequencies of Tower concepts

	1st fore-aft [Hz]	**2nd fore-aft [Hz]**	**1st side-side [Hz]**	**2nd side-side [Hz]**	**3rd side-side [Hz]**
Tower 1	2.2588	7.4385	0.9173	2.2651	7.4631
Tower 2	0.1198	0.8951	0.12039	0.92055	0.95814
Tower 3	0.0704	0.5817	0.0708	0.6225	0.9211

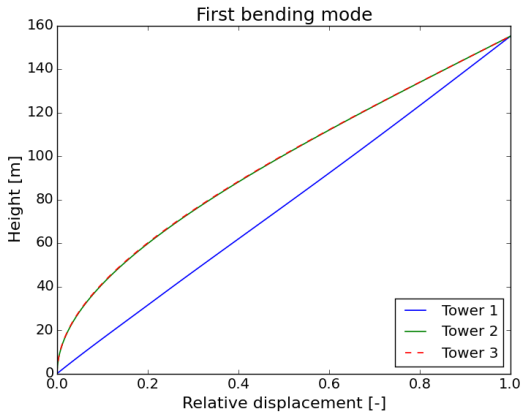

Figure D.1: First bending mode shape

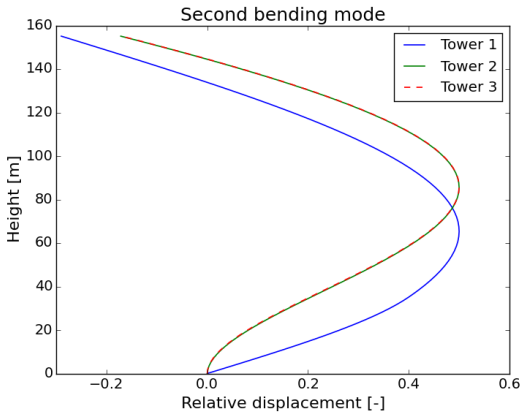

Figure D.2: Second bending mode shape

D.2. Damping

In this section, the damping ratios for the three tower concepts as described in section 4.4.2 are estimated. Two load cases will be analyzed; a step wind from 25 m/s to 20 m/s and a step wind from 10 m/s to 7 m/s, in which the turbine will be operational. The wind speed over time is shown in figure D.3. In figures D.4, D.5 and D.6, the tower top acceleration for the three tower concepts are shown as output of the predefined step wind. Next to that, equation D.1 is plotted in these three figures as well [74]. In this equation, $\hat{A}$ is the amplitude, ω the natural frequency of the tower (in rad/s), t the time and ζ the damping ratio. This line is fitted manually to find the damping ratio ζ.

$$\hat{x} = \hat{A}e^{-\zeta\omega t} \tag{D.1}$$

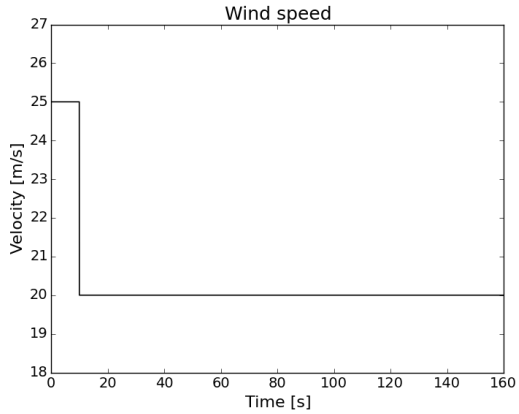

Figure D.3: Wind speed at hub height

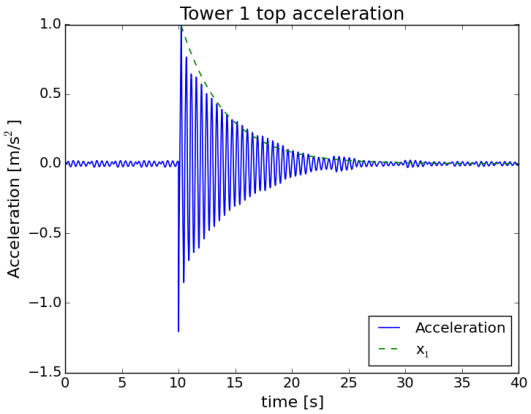

Figure D.4: Tower 1 top acceleration

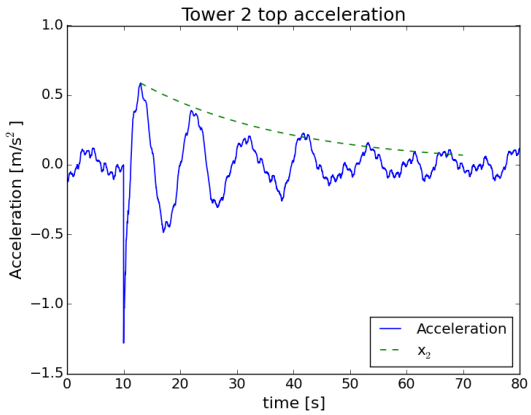

Figure D.5: Tower 2 top acceleration

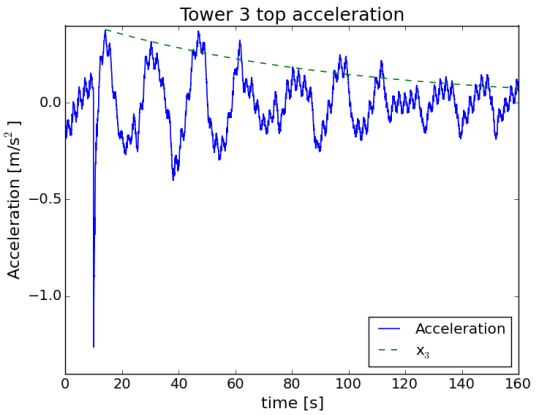

Figure D.6: Tower 3 top acceleration

The damping ratio found for Tower 1 is approximately 1.8%, for Tower 2 5% and for Tower 3 2.5%. Another step wind load case is analysed, as shown in figure D.7. The wave conditions of DLC 1.6 at rated wind speed as described in chapter 4. The acceleration responses of the three tower concepts is shown in figures D.8 - D.10. For this load case damping ratios are found of 1.8%, 6% and 10% for Tower 1, Tower 2 and Tower 3, respectively.

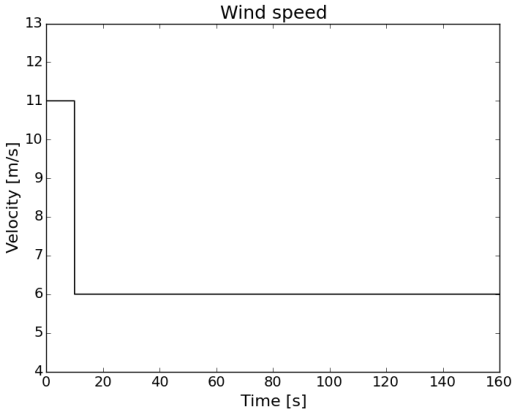

Figure D.7: Wind speed at hub height

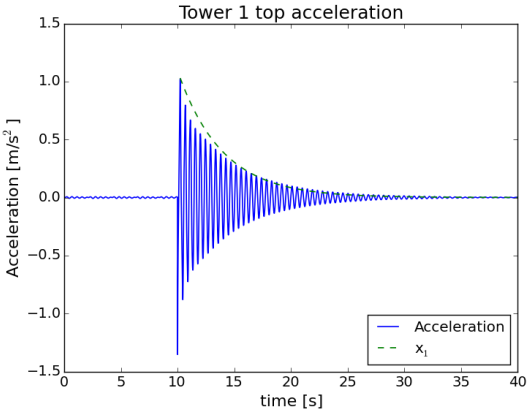

Figure D.8: Tower 1 top acceleration

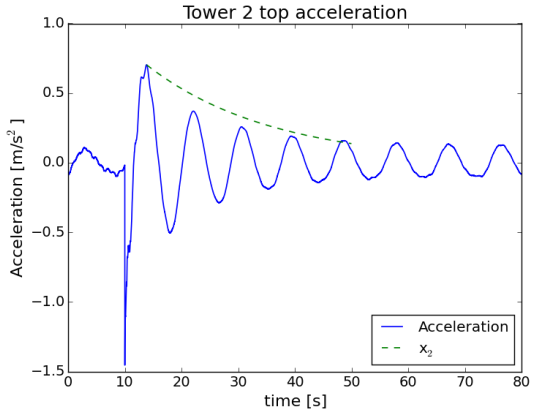

Figure D.9: Tower 2 top acceleration

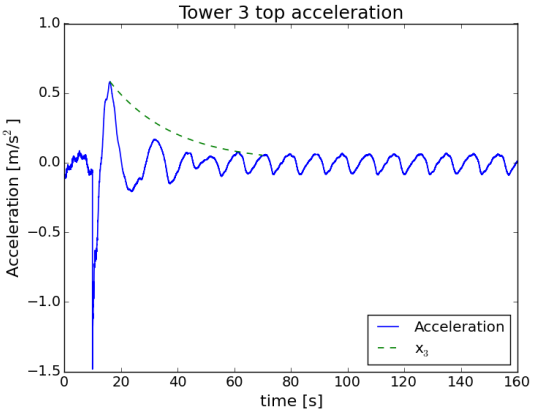

Figure D.10: Tower 3 top acceleration

From these two step wind load case analyses it is concluded that the damping ratio will depend on natural frequency of the support structure and loading condition. Since it is not the purpose of this project to find the exact damping values for specific support structures, a first initial guess as used in [10] is used in the parametric design model.

D.3. Maximum loading

The simulation results of DLC 6.1 and DLC 1.6 at rated wind speed for all three tower concepts are shown in figures D.17 - D.16. As can been seen, each random seed results in a different bending moment distribution along the structure. Especially DLC 6.1 for the flexible towers show large variations. For Tower 2 and Tower 3, the difference between minimum and maximum root bending moment is 23% and 25%, respectively.

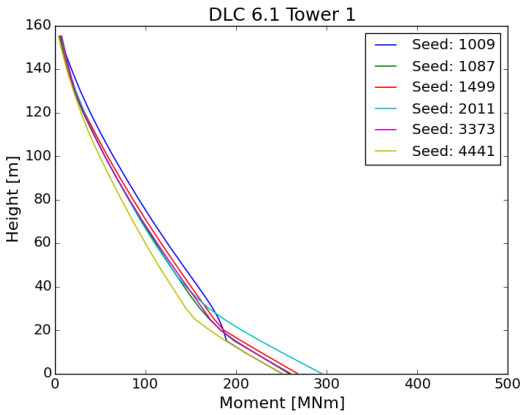

Figure D.11: DLC 6.1, moment distribution of Tower 1

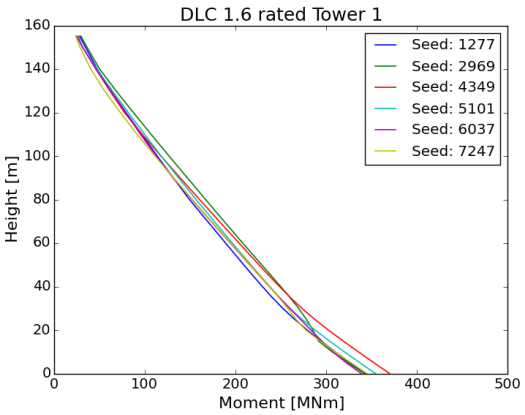

Figure D.12: DLC 1.6 rated, moment distribution of Tower 1

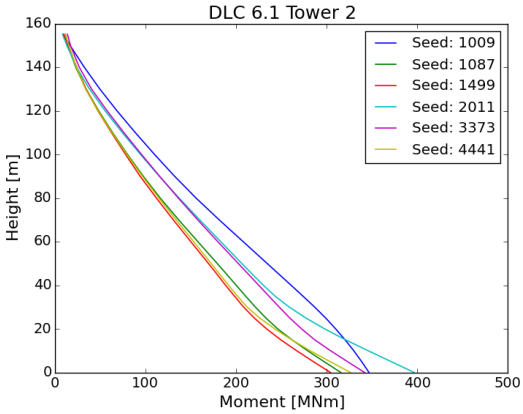

Figure D.13: DLC 6.1, moment distribution of Tower 2

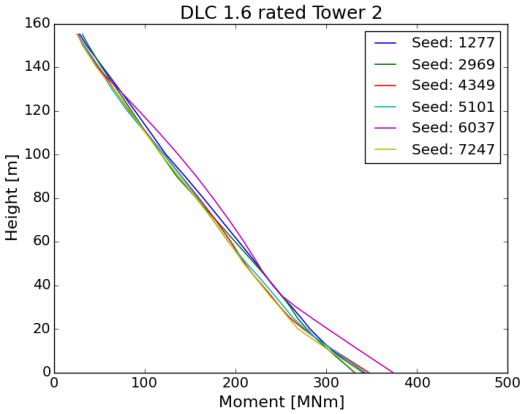

Figure D.14: DLC 1.6 rated, moment distribution of Tower 2

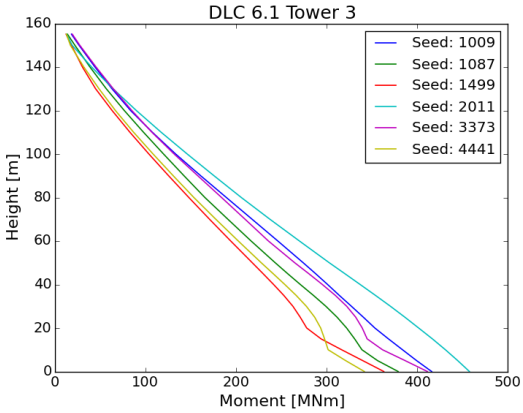

Figure D.15: DLC 6.1 Bending moment distribution of Tower 3

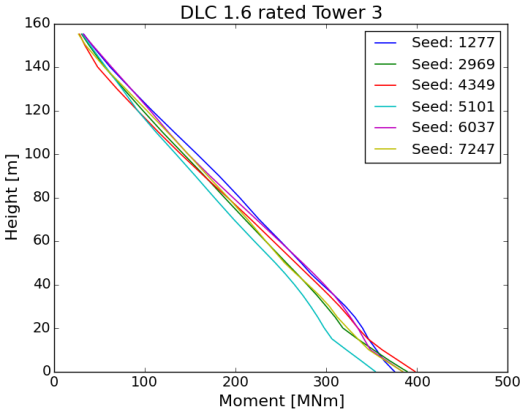

Figure D.16: DLC 1.6 rated, moment distribution of Tower 3

The simulation results of DLC 1.6 at cut-out wind speed are given in figures D.17, D.13 and D.15. For this load case, largest differences are present for Tower 1. This load case was analyzed as well with blade deformations enabled, for which the results are shown in figures D.18, D.20 and D.22. As can been seen, the difference in loading distribution on the support structure with and without blade deformations is negligible.

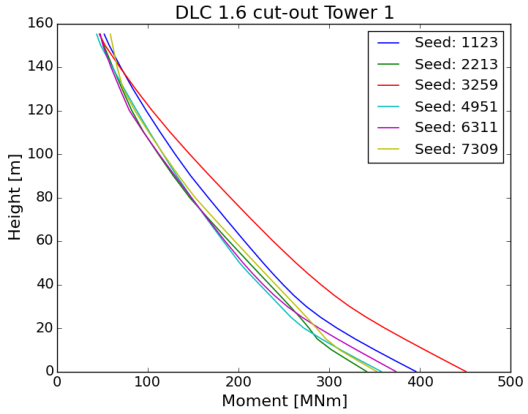

Figure D.17: DLC 1.6 cut-out, moment distribution of Tower 1

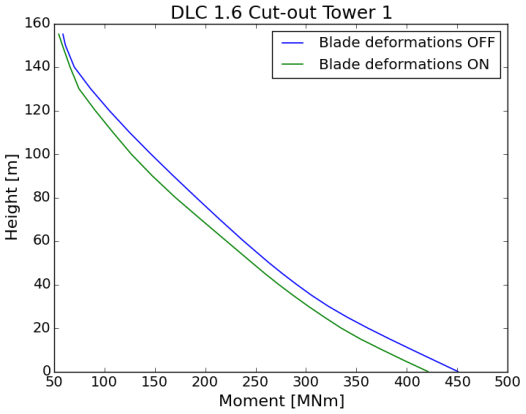

Figure D.18: DLC 1.6 cut-out, max moment distribution of Tower 1

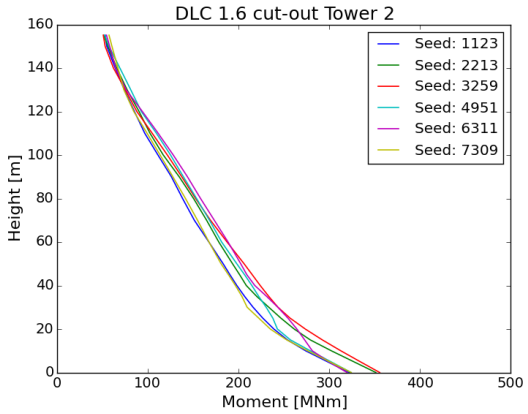

Figure D.19: DLC 1.6 cut-out, moment distribution of Tower 2

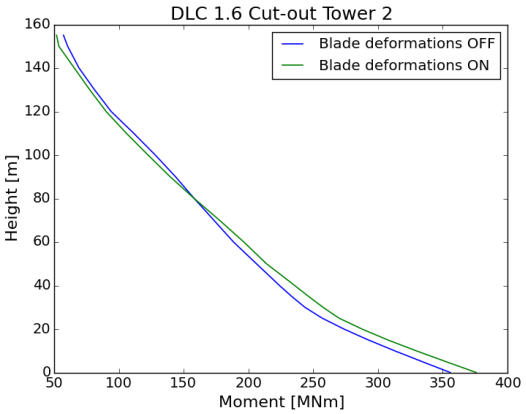

Figure D.20: DLC 1.6 Cut-out, max moment distribution of Tower 2

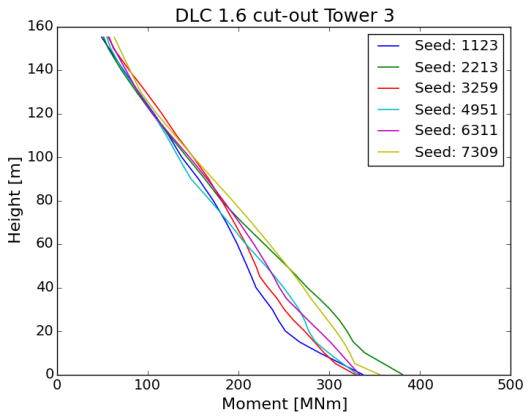

Figure D.21: DLC 1.6 cut-out, moment distribution of Tower 3

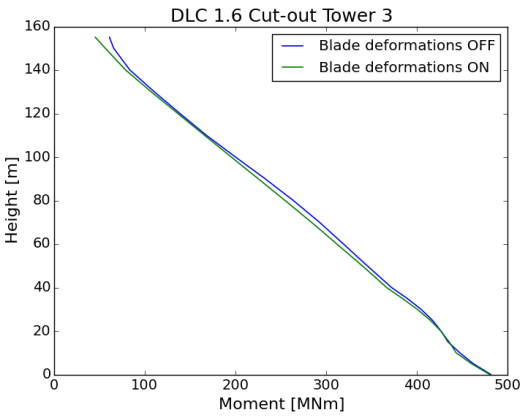

Figure D.22: DLC 1.6 Cut-out, max moment distribution of Tower 3

Bibliography

[1] L. Wang, A. Kolios, and M.M. Luengo. Structural optimisation of wind turbine towers based on finite element analysis and genetic algorithm. *Wind Energy Sci. Discuss*, 2016.

[2] B.W. Byrne, R. McAdam, and H.J. Burd et al. New design methods for large diameter piles under lateral loading for offshore wind applications. In *3rd International Symposium on Frontiers in Offshore Geotechnics*, Oslo, Norway, 2015.

[3] G. T. Houlsby. Interactions in offshore foundation design. *Geotechnique*, 66(10):791–825, 2016.

[4] T. Gentils, L. Wang, and A. Kolios. Integrated structural optimisation of offshore wind turbine support structures based on finite element analysis and genetic algorithm. *Applied Energy*, 199:187–204, 2017.

[5] M. Muskulus and S. Schafhirt. Design optimization of wind turbine support structures - a review. *Journal of Ocean and Wind Energy*, 1(1):12–22, 2014.

[6] D.J. Polyzois, I.G. Raftoyiannis, and N. Ungkurapinan. Static and dynamic characteristics of multi-cell jointed GFRP wind turbine towers. *Composite Structures*, 90:34–42, 2009.

[7] A.C. Young, A.J. Goupee, H.J. Dagher, and A.M. Viselli. Methodology for optimizing composite towers for use on floating wind turbines. *Journal of Renewable and Sustainable Energy*, 9(3), 2017. 033305.

[8] K. Chew, K. Tai, E.Y.K. Ng, and M. Muskulus. Optimization of offshore wind turbine support structures using an analytical gradient-based method. *Energy Procedia*, 80:100–107, 2015.

[9] F. Vorpahl, H. Schwarze, T. Fischer, M. Seidel, and J. Jonkman. Offshore wind turbine environment, loads, simulation and design. *Wiley Interdisciplinary Reviews: Energy and Environment*, 2(5):548–570, 2013.

[10] L. Arany, S. Bhattacharya, J. Macdonald, and S.J. Hogan. Design of monopiles for offshore wind turbines in 10 steps. *Soil Dynamics and Earthquake Engineering*, 92:126–152, 2017.

[11] R. Haghi. Integrated design and optimization of an offshore wind turbine monopile support structure. Master's thesis, Delft University of Technology, 2011.

[12] T. Fischer, W. de Vries, P. Rainey, B. Schmidt, K. Argyriadis, and M. Kühn. Offshore support structure optimization by means of integrated design and controls. *Wind Energy*, 15:99–117, 2012.

[13] N. Maljaars. Support structure optimization. Master's thesis, Delft University of Technology, 2017.

[14] H. Karadeniz, V. Togan, and T. Vrouwenvelder. Optimization of steel monopod-offshore-towers under probabilistic constraints. *Journal of Offshore Mechanics and Arctic Engineering*, 132(2):1–7, 2010.

[15] H.M. Negm and K.Y. Maalawi. Structural design optimization of wind turbine towers. *Computers and Structures*, 74:649–666, 2000.

[16] P.E. Uys, J. Farkas, K. Jármai, and F. van Tonder. Optimisation of a steel tower for a wind turbine structure. *Engineering Structures*, 29:1337–1342, 2007.

[17] M.J. Kühn. *Dynamics and Design Optimisation of Offshore Wind Energy Conversion Systems*. PhD thesis, Delft University of Technology, 2001.

[18] T. Ashuri. *Beyond Classical Upscaling: Integrated Aeroservoelastic Design and Optimization of Large Offshore Wind Turbines*. PhD thesis, Delft University of Technology, 2012.

[19] T. Ashuri, M.B. Zaaijer, J.R.R.A. Martins, G.J.W. van Bussel, and G.A.M. van Kuik. Multidisciplinary design optimization of offshore wind turbines for minimum levelized cost of energy. *Renewable Energy*, 68:893–905, 2014.

[20] T. Ashuri, C. Ponnurangam, J. Zhang, and M. Rotea. Integrated layout and support structure optimization for offshore wind farm design. *Journal of Physics: Conference Series*, 753(9), 2016. 092011.

[21] Deltares. Site Studies Wind Farm Zone Borssele: Meteocean study for the Borssele Wind Farm Zone Site III. Technical report, 2015.

[22] S. Hasan. Analysis and design of a new generation GFRP wind turbine tower. Master's thesis, University of Mantitoba, 2013.

[23] E. Gutiérrez, S. Primi, F. Taucer, P. Caperan, D. Tirelli, J. Mieres, I. Calvo, J. Rodriquez, F. Vallano, C. Galiotis, D. Mouzakis, and D. Karabalis. A wind turbine tower design based on the use of fibre-reinforced composites. Technical report, Eurpean Commission Joint Research Centre, 2013.

[24] S. Lim, C. Kong, and H. Park. A study on optimal design of filament winding composite tower for 2 MW class horizontal axis wind turbine systems. *International Journal of Composite Materials*, 3(1):15–23, 2013.

[25] H.J. Dagher A.M. Viselli, A.J. Goupee. Model test of a 1:8-scale floating wind turbine offshore in the Gulf of Maine. *Journal of Offshore Mechanics and Arctic Engineering*, 137(4), 2015. 041901.

[26] H. Dagher, A. Viselli, A. Goupee, R. Kimball, and C. Allen. The volturnUS 1:8 floating wind turbine: Design, construction, deployment, testing, retrieval, and inspection of the first-grid-connected offshore wind turbine in US. Technical report, University of Maine, 2017.

[27] T. van der Zee, M.J. de Ruiter, and I. Wieling. The C-Tower project - A composite tower for offshore wind turbines. *Energy Procedia*, 137:401–405, 2017.

[28] S. Bisoi and S. Haldar. Dynamic analysis of offshore wind turbine in clay considering soil-monopile-tower interaction. *Soil Dyanmics and Earthquake Engineering*, 63:19–35, 2014.

[29] S. Bisoi and S. Haldar. Design of monopile supported wind turbine in clay considering dynamic soil-structure-interaction. *Soil Dynamics and Earthquake Engineering*, 73:103–117, 2015.

[30] Y. Kuo, M. Achmus, and K. Abdel-Rahman. Minimum embedded length of cyclic horizontally loaded monopiles. *Journal of Geotechnical and Geoenvironmental Engineering*, 138(3):357–363, 2012.

[31] M. Martinez-Luengo, A. Kolios, and L. Wang. Parametric FEA modelling of offshore wind turbine support structures: Towards scaling-up and CAPEX reduction. *International Journal of Marine Energy*, 19:16–31, 2017.

[32] DNV GL. Design of Offshore Wind Turbine Structures. DNV-OS-J101, 2014.

[33] J. van der Tempel. *Design of Support Structures for Offshore Wind Turbines*. PhD thesis, Delft University of Technology, 2006.

[34] DNV. Fatigue design of offshore steel structures. DNV-RP-C203, 2010.

[35] DNV GL. Rotor blades for wind turbines. DNVGL-ST-0376, 2015.

[36] Y. Lee, B. Choi, J.H. Lee, S.Y. Kim, and S. Han. Reliability-based design optimization of monopile transition piece for offshore wind turbine system. *Renewable Energy*, 71:729–741, 2014.

[37] L. Arany, S. Bhattacharya, and J. Macdonald ans S.J. Hogan. Simplified critical mudline bending moment spectra of offshore wind turbine support structures. *Wind Energy*, 18(12):2171–2197, 2015.

[38] L. Wang, A. Kolios, T. Nishino, P.L. Delafin, and T. Bird. Structural optimisation of vertical-axis wind turbine composite blades based on finite element analysis and genetic algorithm. *Composite Structures*, 153:123–138, 2016.

[39] J.H. Park, J.H. Hwang, C.S. Lee, and W. Hwang. Stacking sequence design of composite laminates for maximum strength using genetic algorithms. *Composite Structures*, 52:217–231, 2001.

[40] L. Arany, S. Bhattacharya, J.H.G. Macdonald, and S.J. Hogan. Closed form solution of Eigen frequency of monopile supported offshore wind turbines in deeper water incorporating stiffness of substructure and SSI. *Soil Dynamics and Earthquake Engineering*, 83:18–32, 2016.

[41] W.S. Chan and K.C. Demirhan. A simple closed-form solution of bending stiffness for laminated composite tubes. *Journal of Reinforced Plastics and Composites*, 19(4):278–291, 2000.

[42] L. Arany, S. Bhattacharya, S. Adhikari, S.J. Hogan, and J.H.G. Macdonald. An analytical model to predict the natural frequency of offshore wind turbines on three-spring flexible foundations using two different beam models. *Soil Dynamics and Earthquake Engineering*, 74:40–45, 2015.

[43] M.B. Zaaijer. Foundation modelling to assess dynamic behaviour of offshore wind turbines. *Applied Ocean Research*, 28:45–57, 2006.

[44] C. Lindenburg. *Phatas User's Manual*. Knowlegde Center WMC, 11011 edition, July 2018.

[45] P. Frohboese and C. Schmuck. Thrust coefficients used for estimation of wake effects for fatigue load calculation. In *Europen Wind Energy Conference 2010*.

[46] DNV. Environmental conditions and environmental loads. DNV-RP-C205, 2010.

[47] J.D. Fenton. A fifth-order stokes theory for steady waves. *Journal of Waterway, Port, Coastal and Ocean Engineering*, 111(2):216–234, 1985.

[48] T. van Eijk. Gravity based foundation - scour and design optimisation. Master's thesis, Delft Univserity of Technology, 2016.

[49] J.D. Fenton. *Use of the programs FOURIER, CNOIDAL and STOKES for steady waves*, 2018.

[50] C. Dyrbye and S.O. Hansen. *Wind Loads on Structures*. John Wiley & Sons Ltd, West Sussex, England, 1997.

[51] DNV GL. Loads and site conditions for wind turbines. DNVGL-ST-0437, 2016.

[52] M. Zaaijer. personal communication, 07-03-2019.

[53] J.M. Peeringa. *Stream function wave program - User's manual*, 2005.

[54] K. Wei, A.T. Myers, and S. R. Arwade. Dynamic effects in the response of offshore wind turbines supported by jackets under wave loading. *Engineering Structures*, 142, 2017.

[55] T.J.J. van der Zee, R.R.H. Brood, and C. Lindenburg. *SWIFT-R Manual. Turbulent wind field generation on rectangular grid*. Knowlegde Center WMC, wmc-2015-88 edition, February 2016.

[56] DNV. Buckling Strength of Shells. DNV-RP-C202, 2013.

[57] L. Wang, X. Liu, L. Guo, N. Renevier, and M. Stables. A mathematical model for calculating cross-sectional properties of modern wind turbine composite blades. *Renewable Energy*, 64:52–60, 2014.

[58] X.S. Sun, Y. Chen, V.B.C. Tan, R.K. Jaiman, and T.E. Tay. Homogenization and stress analysis of multilayered composite offshore production risers. *Journal of Applied Mechanics*, 81(3), 2014. 031003.

[59] M. Siegl and I. Ehrlich. Transformation of the mechanical properties of fiber-reinfored plastic tubes from the cartesian coordinate system into the cylindrical coordinate system for the application of bending models. *Athens Journal of Technology & Engineering*, 4(1):47–62, 2017.

[60] C. Kassapoglou. *Design and Analysis of Composite Structures*. John Wiley & Sons Ltd, West Sussex, United Kingdom, 2013.

[61] I.M. Daniel and O. Ishai. *Engineering Mechanics of Composite Materials*. Oxford University Press, New York, USA, 2006.

[62] B.F. Tatting, Z. Gürdal, and V.V. Vasiliev. The Brazier effect for finite length composite cylinders under bending. *International Journal Solids Structures*, 34(12):1419–1440, 1997.

[63] B. Geier, H.R. Meyer-Piening, and R. Zimmermann. On the influence of laminate stacking on buckling of composite cylindrical shells subjected to axial compression. *Composite Structures*, 55:467–474, 2002.

[64] J. Tang. Semi-analytical solution to buckling of variable-stiffness composite panels. Master's thesis, Delft University of Technology, 2015.

[65] C. Lindenburg and G.D. de Winkel. Buckling load prediction tools for rotor blades: Model description of tools for buckling of thin-walled beams. ECN-C-05-103, Energieonderzoek Centrum Nederland, 2005.

[66] S. Yoshida. Wind turbine tower optimization method using a genetic algorithm. *Wind Engineering*, 30(6):453–470, 2006.

[67] K. Deb and R.B. Agrawal. Simulated binary crossover for continuous search space. *Complex Systems*, 9:115–148, 1995.

[68] V.C. van de Putte. Dynamic analysis of a monopile offshore wind support structure subjected to earthquakes. Master's thesis, Delft University of Technology, 2018.

[69] T. Yokoyama. Vibrations of a hanging timoshenko beam under gravity. *Journal of Sound and Vibration*, 141(2):245–258, 1990.

[70] T. Yokoyama. Parametric instability of timoshenko beams resting on an elastic foundation. *Computers & Structures*, 28(2):207–216, 1987.

[71] J.D. Fenton. Nonlinear wave theories. *The Sea*, 9(3), 1990.

[72] FOURIER, CNOIDAL and STOKES for steady waves. `http://johndfenton.com/Steady-waves/Fourier.html`. Accessed: 21-02-2019.

[73] Germanischer Lloyd. Guideline for the certification of offshore wind turbines. Technical report, 2012.

[74] M. Damgaard, J.K.F. Andersen, L.B. Ibsen, and L. V. Andersen. Natural frequency and damping estimation of an offshore wind turbine structure. In *Proceedings of the Twenty-second (2012) International Offshore and Polar Engineering Conference*.